Rydberg Molecules Bound By Mixed Singlet-Triplet Scattering

MASTERARBEIT
vorgelegt von

Fabian Böttcher

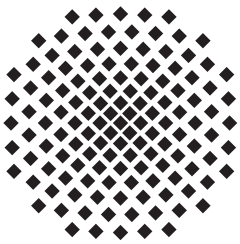

Universität Stuttgart

Hauptberichter: **Prof. Dr. Tilman Pfau**
Mitberichter: **Prof. Dr. Peter Michler**

5. Physikalisches Institut
Universität Stuttgart
4. Dezember 2015

Ehrenwörtliche Erklärung

Hiermit erkläre ich, dass ich die vorliegende Arbeit selbstständig verfasst habe und keine anderen als die angegebenen Quellen benutzt wurden. Alle wörtlich oder sinngemäß aus anderen Werken übernommenen Aussagen sind als solche gekennzeichnet. Die vorliegende Arbeit war weder vollständig noch in Teilen Gegenstand eines anderen Prüfungsverfahrens. Weiterhin stimmt das elektronische Exemplar mit der gedruckten Version überein.

Filderstadt, 4. Dezember 2015

Fabian Böttcher

Zusammenfassung

Die uns umgebende Welt ist aus Materie aufgebaut, welche wiederum aus diskreten Teilchen aufgebaut wird: den Atomen. Heute wissen wir, dass die Atome an sich aus noch kleineren Teilchen zusammengesetzt sind: einem positiv geladenen Kern aus Protonen und Neutronen und den, an den Kern gebundenen, Elektronen. Dieses Atommodell basiert auf den berühmten Streuexperimenten von Rutherford [61] und wurde bis heute zu einer kompletten quantenmechanischen Beschreibung des Atoms ausgebaut. Dabei können die Bindungsenergien der Elektronen, die an den Kern gebunden sind, nur diskrete Werte annehmen. Sind mehrere Elektronen an einen Kern gebunden, so wird der energetisch günstigste Gesamtzustand angestrebt, welcher durch die Besetzung der Energieniveaus gemäß der Hund'schen Regeln [62] beschrieben wird. Die möglichen Energieniveaus eines Elektrons im Atom werden an Hand mehrerer Quantenzahlen beschrieben, der Hauptquantenzahl n, der Drehimpulsquatenzahl l und der magnetischen Quantenzahl m.
Mit Laserlicht ist es möglich ein Elektron (oder auch mehrere Elektronen) in einen hochangeregten Zustand mit der Quantenzahl n, einem sogenannten Rydberg-Zustand, anzuregen. Dabei nimmt die Größe des Atoms deutlich zu, da der klassische Elektronenradius mit n^2 skaliert. Dadurch weisen Rydbergatome erstaunliche Eigenschaften auf. Zum Beispiel wechselwirken sie so stark miteinander, dass durch die Präsenz eines Rydbergatoms die Energieniveaus von benachbarten Atomen so weit verschoben werden, dass der Übergang in den Rydberg-Zustand mit Hilfe des Laserlichts nicht mehr resonant stattfinden kann. Dieser Effekt wird Rydberg-Blockade [63] genannt und kann dazu ausgenutzt werden um nur einzelne Rydbergatome in einem Ensemble von Atomen anzuregen. Des Weiteren sind die Elektronen in einem Rydberg-Zustand nur noch sehr schwach an ihren Kern gebunden, sodass kleinste elektrische Felder ausreichen um sie zu ionisieren. Deshalb und aufgrund des starken Stark-Effektes durch die hohe Polarisierbarkeit der Rydberg-Zustände ist es notwendig die elektrischen Felder im Experiment sehr genau zu kontrollieren und abzuschirmen.
In dichten Atomwolken ist der mittere Teilchenabstand vergleichbar mit der Größe der Rydbergatome, was zu einer Wechselwirkung zwischen dem Rydbergatom und den umliegenden Atomen im elektronischen Grundzustand führt. Dies wurde zuerst von Amaldi und Segrè in Absorptionsspektren von hochangeregten Alkaliatomen in dichten Gaszellen eines fremden Gases beobachtet [17]. Dabei sahen sie eine Verschiebung und eine Verbreiterung der spektralen Linie des Übergangs, wobei beide Effekte vom Fremdgas, in dem sich die Alkaliatome befanden, abhingen. Die Messergebnisse erklärte daraufhin Enrico Fermi als einen Effekt der Streuung der quasi-freien Rydbergelektronen mit den neutralen Atomen des fremden Gases die sich in der Wellenfunktion des Rydbergelektron befinden [18]. Dabei wird die Streuung als Kontaktwechselwirkung mit einer Streulänge a_0 beschrieben, welche

dabei, abhängig vom Fremdgas, sowohl positiv als auch negativ sein kann. Dadurch kann sowohl eine anziehende als auch eine abstoßende Wechselwirkung entstehen, genau wie es von Amaldi und Segrè [17] gemessen wurde. Spätere theoretische Arbeiten zur Streuung von Elektronen an neutralen Atomen, wie zum Beispiel [24, 27, 16], fürthen schließlich zum Wechselwirkungspotential von Omont [19].
Mit den experimentellen Fortschritten im Bereich der Laserkühlung und der darauf folgenden Bose-Einstein Kondensation, wurde von Chris Greene et al. [28] darauf hingewiesen, dass im Wechselwirkungspotential zwischen Rydbergelektron und Grundzustandsatom gebundene Molekülzustände möglich sein sollten wenn die thermische Energie der Atome klein genug ist. Diese langreichweitigen Rydberg-Moleküle wurden zuerst von Bendkowsky et al. [29] in Rubidiumatomen experimentell beobachtet. Seit dieser experimentellen Entdeckung der Rydberg-Moleküle wurden viele Phänomene untersucht, wie zum Beispiel Moleküle mit mehreren Atomen [30, 35], die kohärente Erzeugung und Brechung der Molekülbindung [31], die Lebenszeit der Molekülzustände [32, 64], exotische Trilobite-Zustände [33, 37], die Hybridisierung der Molekülorbitale in externen elektrischen Feldern [36] und auch Rydbergatome eingebettet in Bereichen sehr hoher Dichte [4, 5]. Des Weiteren wurden Rydberg-Moleküle auch für S-Zustände in Cs [38] und Sr [41, 64], für P-Zustände in Rb [40] und Cs [3] und auch für D-Zustände in Rb [34, 36, 39] realisiert.
Für die Molekülbindung der Rydberg-Moleküle muss die Streuung von Rydbergelektron und Grundzustandsatom zu einer anziehenden Wechselwirkung führen, was nur der Fall ist wenn die Streulänge negativ ist. Der Streuprozess an sich hängt dabei von der Energie [57] und der relativen Orientierung der beiden Spins [22, 23] der Streupartner ab. Für die Streuung von Elektronen mit neutralen Rubidium Atomen ist die Streulänge nur negativ, wenn sich die beiden Spins in einer symmetrischen Triplett Konfiguration befinden. Für den Fall der anti-symmetrischen Singulett Konfiguration der beiden Spins, ist die Streulänge hingegen positiv und somit sind keine gebunden Molekülzustände im Singulett-Streupotential möglich.
Vor kurzem wurde von Anderson et al. [2] darauf hingewiesen, dass die Hyperfeinwechselwirkung im Grundzustand des neutralen Atoms zu einer Mischung von Streukanälen mit reiner Triplett- und reiner Singulett-Streuung führt. Dies kann zu gebunden Molekülzuständen führen die durch gemischte Singulett-Triplett-Streuung gebunden sind. Diese Molekülzustände wurden zuerst von Saßmannshausen et al. [3] experimentell beobachtet. Im Rahmen dieser Arbeit und der daraus resultierenden Publikation [1] wurden diese gemischten Singulett-Triplett Rydberg-Moleküle ebenfalls untersucht. Dabei wurden die Moleküle spektroskopisch für einen Bereich von Quantenzahlen, $n = 36 - 45$, beobachtet. In den Spektren, gemessen in sub-μK thermischen Wolken, sind dabei deutlich unterscheidbare Linien zu erkennen, welche den gebundenen Molekülzuständen im Streupotential von Rydbergelektron und Grundzustandsatom zugeordnet werden können. Dabei wurden die Potentialkurven mit Hilfe eines einfachen Modells berechnet, welches nur die Unterzustände des 5S Grundzustand von Rb und des nS Rydbergzustand berücksichtigen. Mit den verwendeten Polarisationen der beiden Anregungslaser ist es möglich den Spin der zu Beginn spinpolarisierten Atome während der Anregung umzudrehen, was dazu führt, dass nur ein Teil der berechneten Potentialkurven für das Experiment relevant sind. Für die gemischten

Singulett-Triplett Potentialkurven spielt sowohl die Singulett-Streuung als auch die Resonanz in der p-Wellen Triplett-Streuung eine entscheidende Rolle, weshalb die beiden nicht vernachlässigt werden können, wie dies in den meisten bisherigen Arbeiten zu Rydberg-Molekülen der Fall war.
Ohne ein externes magnetisches Feld erhält man zwei Potentialfamilien: die reinen Triplett-Potentiale und Potentiale mit gemischter Singulett-Triplett Streuung. Dabei treten diese beiden Potentialfamilien sowohl für den $F = 1$ als auch für den $F = 2$ Hyperfeinzustand des 5S Grundzustandes auf. Im Gegensatz zu der Arbeit von Saßmannshausen et al. [3] wird in dem hier beschriebenen Experiment ein externes Magnetfeld dazu benutzt um die Atome zu fangen. Das angelegte Magnetfeld führt dazu, dass die Potentialkurven zusätzlich verändert werden. Durch das angelegte Magnetfeld sind die berechneten Potentialkurven der einzelnen Unterzustände nicht mehr energetisch entartet und die Tiefe der jeweiligen Streupotentiale ändert sich mit der Stärke des angelegten Magnetfeldes. Diese nicht-triviale Abhängigkeit vom angelegten Magnetfeld wurde theoretisch für einen großen Bereich von Feldstärken und experimentell für den Bereich 1.65 - 2.51 G untersucht. Im experimentell untersuchten Bereich wurde herausgefunden, dass die erhaltenen magnetischen Momente der Molekülzustände deutlich von denen des jeweiligen Rydberg-Zustandes abweichen. Diese Abhängigkeit vom angelegten Magnetfeld kann im Prinzip dazu benutzt werden um den Molekülzustand maßzuschneidern, ähnlich wie es schon für das elektrische Feld gezeigt wurde [36, 37].
Durch Erhöhen der Atomdichte, was durch die weitere Abkühlung der Atome und die darauf folgende Bose-Einstein Kondensation möglich ist, verschwinden die unterscheidbaren Linien in eine breite Spektrallinie. Dies wurde für den 53S Rydbergzustand sowohl für die Anregung in einen Zustand mit reiner Triplett-Streuung als auch in einen Zustand mit gemischter Singulett-Triplett-Streuung gemessen. Dabei ist zu sehen, dass die spektrale Breite für den gemischten Zustand deutlich geringer ist als für den reinen Triplett-Zustand. Dies kann dadurch erklärt werden, dass das experimentell zugängliche gemischte Potential durch das angelegte Magnetfeld schon deutlich schwächer ist als dies für die reine Triplett-Streuung der Fall ist.
Die im Rahmen dieser Arbeit präsentierten Messungen und das theoretische Modell zum Erklären dieser Molekülspektren, zeigen deutlich den Einfluss der Mischung von Singulett und Triplett Streuung auf Rb_2 Rydberg-Moleküle. Dabei können die gemessenen Spektren in Zukunft als Referenz für die Berechnung des Elektron-Rubidium Streuproblems und den daraus gewonnen Singulett und Triplett Streuphasen dienen. Messergebnisse in diesem Energiebereich waren zur Zeit dieser Berechnungen [22, 23] nicht verfügbar, weshalb eine Extrapolation zu diesen Energien durchgeführt wurde. Durch die reichlichen Messdaten zu Rydberg-Molekülen und auch aufgrund der verbesserten Messgenauigkeit anderer Eingangsparameter, wie z.B. der Polarisierbarkeit des 5S Grundzustandes von Rubidium, kann dies zu einer deutlichen Verbesserung in der Berechnung der Streuphasen führen.

Contents

1. Introduction

The idea that matter is made up by discrete particles has already been used by philosophers in ancient Greece. These discrete particles, which are today called atoms, are made up of a positive charged core and electrons bound to this core. This model of the atom was first proposed by Rutherford, in order to explain the results of his famous α-particle scattering experiment [61]. The model of the atom has since then been improved to a full quantum mechanical description of the system. The electrons are attracted by the electromagnetic force of the positive charged nucleus and in this potential they can populate only a discrete number of orbitals. The electrons will populate the energy levels according to Hund's rules [62], which results in the ground state of the atom with the lowest total energy. The possible energy levels of the electron are thereby labelled by the principal quantum number n, the angular momentum quantum number l, and the magnetic quantum number m.
With laser light it is possible to excite a single electron (or even more electrons) to a state with a high principal quantum number n, a so-called Rydberg state. The radius of the electron wavefunction thereby scales with n^2, leading to large sizes of such Rydberg atoms. This leads to long-range interactions between different Rydberg atoms, which leads to the Rydberg blockade effect [63]. This blockade can be used to create single Rydberg impurities in an atomic sample as it is done in the experiment that will be described in the course of this thesis. Due to the large distance between the Rydberg electron and the ionic core, the electron is only loosely bound and as such the interaction with external electric fields can remove the electron from the binding ionic core. Because of the sensitivity of Rydberg states to electric fields, a good control of stray electric fields is necessary in order to observe Rydberg atoms in the experiment, which is achieved with an electric field compensation chamber that will be described in detail later on.
In a dense atomic sample, the interparticle distance can be comparable to the size of the Rydberg atom, leading to an interaction between the Rydberg atom and the ground state atoms. This was experimentally observed by Amaldi and Segrè in the absorption spectra of alkali atoms excited to Rydberg states, which were immersed in a dense foreign gas [17]. They observed a broadening and a shift of the spectral line, that depends on the foreign gas that was used and could as such not be explained by pressure broadening. Enrico Fermi explained this as the effect of the scattering of the quasi-free Rydberg electron with the neighbouring ground state atoms inside the electron wavefunction [18]. The scattering is thereby described by the scattering length a_0, which can either be positive or negative depending on the foreign gas. This can lead to a repulsive as well as an attractive interaction, which can lead to a broadening and a shift of the spectral line as it was observed by Amaldi and Segrè. Further theoretical work on the scattering process of an electron with the polarization potential of a neutral atom, e.g. [24, 27, 16], leads to the complete

interaction potential given by Omont [19].
With the advances in laser cooling techniques and the subsequent realization of Bose-Einstein condensates, it was pointed out by Chris Greene et al. [28] that it should be possible to realize bound molecular states in the scattering interaction potential, due to the small kinetic energy of the ground state atoms at these low temperatures. These ultralong-range Rydberg molecules were for the first time experimentally observed by Bendkowsky et al. [29] for Rubidium atoms excited to nS Rydberg states. Since the initial experimental observation of Rydberg molecules, a variety of phenomena have been explored, such as molecular states containing more than one ground state atom [30, 35], coherent creation and breaking of the molecular bond [31], the lifetimes of the ground and excited molecular states [32, 64], exotic trilobite states [33, 37], hybridization of the molecular orbitals in electric fields [36] and also Rydberg atoms immersed in high densities [4, 5]. Rydberg molecules have also been experimentally realized for for S-states in Cs [38] and Sr [41, 64], for P-states in Rb [40] and Cs [3] and for D-states in Rb [34, 36, 39].
For the binding of the Rydberg molecules, the scattering of the Rydberg electron with the ground state atom leads to an attractive interaction if the scattering length is negative. The scattering process intrinsically depends on the scattering energy [57] and on the relative spin orientation of the scattering particles [22, 23]. For the scattering of an electron with neutral Rubidium atoms the scattering length is negative if the spins are in a symmetric triplet configuration, while it is positive for the anti-symmetric singlet configuration. This means that bound molecular states should only be possible if the spin of the Rydberg electron and the spin of the ground state atom are in a triplet configuration.
Recently it was pointed out by Anderson et al. [2] that the hyperfine interaction in the ground state of the neutral atom can lead to a mixing of singlet and triplet scattering channels. This can lead to molecular states which are bound by mixed singlet and triplet scattering. These mixed singlet-triplet Rydberg molecules were for the first time experimentally observed by Saßmannshausen et al. [3] and studied in the course of this thesis and the resulting publication [1]. In this thesis these mixed molecules were experimentally observed for principal quantum numbers in the range of $n = 36 - 45$. Thereby a simple theoretical model was used to explain the observed spectral lines, which will be discussed in detail in the following thesis. Also it will be shown that for these mixed molecules the dependence on the external magnetic field is not trivial, which can in principle be used to engineer the molecular state. Furthermore it will be shown, that the experimental data can be used as a reference in order to improve the theoretical calculations of the scattering phase shifts.

About this thesis

This thesis starts with a theoretical overview of Rydberg atoms and the interaction of atoms with external electric and magnetic fields in chapter 2.
In chapter 3 the experimental setup and procedure that is used for the presented measurements is discussed briefly. Also improvements made to some of the parts of the setup in the course of this thesis, e.g. the new version of the experimental chamber that was designed by Udo Hermann [10], are described.
Chapter 4 deals with the concentration of this thesis; namely the Rydberg molecules. In the beginning of the chapter a theoretical overview of the photoassociation process and the scattering process, which leads to the binding of the molecules, is described. In the following section of this chapter a summary of the work done up to now with Rydberg molecules bound by pure triplet scattering is given. Then the theory of the mixed singlet-triplet molecules is explained in detail, such that it is possible to recreate the simple theoretical model used to explain the observed molecular lines by reading this section of the thesis. The last part of the chapter is devoted to the experimental realization and results, comparing the observed molecular lines with the results from the previously presented theory.

2. Theory

In this chapter the theoretical foundations needed in the course of this thesis will be described. It will start with an introduction of Rydberg atoms and the interaction between different Rydberg atoms leading to the Rydberg blockade effect. Then the hyperfine structure of atoms and the interaction of atoms with external magnetic and electric fields will be discussed. The last part of the chapter deals with the process of field ionization used to detect Rydberg atoms in the experiment.

2.1. Rydberg atoms

The smallest component of matter, that still has the same properties as the chemical element as a whole, are the atoms. These atoms are made up by a positively charged nucleus, consisting of protons and neutrons, and electrons bound in the potential of this nucleus. Atoms with one valence electron, which is excited to a state with a high principal quantum number n, can be described in a hydrogen-like manner: A single outer electron is orbiting around a positively charged core, which is shielded by the inner electrons. This shielding of the positive charge is different for different principal quantum numbers and different angular momentum states, leading to some corrections from the situation of the actual hydrogen atom. These corrections can be taken into account by introducing the quantum defects

$$\delta_{nlj} = \sum_i \frac{\delta_i}{(n-\delta_i)^i} \ , \tag{2.1}$$

which therefore also account for the fine structure and the penetration of the electron into the ionic core. In this equation δ_i are the Rydberg-Ritz parameters that can, e.g., be found in [48]. Taking the quantum defects into account, the binding energy E_{nlj} of a Rydberg state is given by

$$E_{nlj} = -\frac{R^*_\infty}{n^{*2}} = -\frac{R^*_\infty}{(n-\delta_{nlj})^2} \ . \tag{2.2}$$

In this equation n^* is the effective principal quantum number and R^*_∞ is the Rydberg constant with the reduced mass taken into account.

$$R^*_\infty = \frac{R_\infty}{1+\frac{m_\mathrm{e}}{M_\mathrm{Rb}}} \tag{2.3}$$

The radius of the classical orbit of the Rydberg electron around the positive charged core scales with n^{*2}. This large distance for Rydberg states leads to interesting scalings with the principal quantum number for several physical properties. A list of properties of the Rydberg atoms and their respective scaling with the principal quantum number can be found in table 2.1.

Property	Scaling	Example for 40S
Binding energy	n^{*-2}	10 meV
Orbital radius	n^{*2}	0.14 µm
Natural lifetime	n^{*3}	68.75 µs
Polarizibility	n^{*7}	$10.57\,\mathrm{MHz(V/cm)^{-2}}$
Blockade radius ($\Delta f = 500\,\mathrm{kHz}$)	$n^{*11/6}$	3.55 µm

Table 2.1.: Interesting properties of Rydberg states, their scaling with the effective principal quantum number n^* and examples for the value of each property for the 40S state.

Two close-by Rydberg atoms interact strongly, even though they have no permanent dipole moment. Fluctuations of the electron density can create temporary dipole moments, which then induce a second temporary dipole moment inside of a neighbouring atom. This process is described by the Van-der-Waals potential

$$V(r) = -\frac{C_6}{r^6}\,, \tag{2.4}$$

where C_6 is the Van-der-Waals coefficient and r is the distance between the two interacting Rydberg atoms.
If one atom is excited to a Rydberg state, this interaction shifts the energy levels of all neighbouring atoms. If this shift is larger than the linewidth Δf of the excitation laser it is not possible to excite a second Rydberg atom. This effect is called the Rydberg blockade. The radius r_B of the blockade sphere around the Rydberg atom is given by

$$r_\mathrm{B} = \sqrt[6]{\frac{C_6}{\Delta f}}\,. \tag{2.5}$$

This blockade radius scales with the quantum number n^*, because the Van-der-Waals coefficient C_6 scales with the principal quantum number n^*. With this effect it is possible to create a single Rydberg excitation in a sample of many atoms, if the sample is smaller than the blockade sphere or if the excitation laser is focused down to a smaller size.

2.2. Hyperfine Structure

The different orbital and spin angular momenta in an atom can couple and lead to energy shifts of the electron energy levels calculated by equation (2.2).
The interaction of the magnetic moments of the electron spin **S** and the orbital angular momentum **L** of the electron is known as spin-orbit coupling and is one contribution of the fine structure of the atom. The energy shift of the electron energy levels introduced by the fine structure are already included in equation (2.2) in the form of the quantum defects. With this interaction the basis of uncoupled states $|L, m_\mathrm{L}\rangle \otimes |S, m_\mathrm{S}\rangle$ is not the eigenbasis of the system anymore, but still remains an orthonormal basis of the system. Because of this coupling of the angular momenta, the total angular momentum $\mathbf{J} = \mathbf{L} + \mathbf{S}$ is introduced. The eigenbasis is now built up from the states $|J, m_\mathrm{J}, L, S\rangle$, which are obtained from a linear combination of the states in the uncoupled basis. The amplitude of **J** is given by $\hbar\sqrt{J(J+1)}$, where the quantum number J can take the values from $L + S$ to $|L - S|$. The effect of the fine structure can be included in the quantum defects for different total angular momentum states.
The atomic core also has a nuclear magnetic moment μ_I which can interact with the magnetic field generated by the electrons. This leads to the so called hyperfine structure, which is typically orders of magnitude smaller than the fine structure. The Hamiltonian describing the hyperfine interaction is given by

$$\hat{H}_\mathrm{HF} = \frac{A_\mathrm{HF}}{\hbar^2}\,\mathbf{I}\cdot\mathbf{J} \tag{2.6}$$

with the hyperfine constant A_HF. For the $5\mathrm{S}_{1/2}$ ground state of ^{87}Rb the hyperfine constant takes the value of $A_\mathrm{HF} = h/2 \cdot 6.835\,\mathrm{GHz}$. For Rydberg states the electron is further away from the core and as such the coupling between the electron and the nuclear magnetic moment is weaker [49, 68, 69]. This leads to a n-dependency of the hyperfine constant, described by the following extrapolation formula given by Mack et al. [49].

$$A_\mathrm{HF} = \frac{h}{2}\cdot 34(3)\,\mathrm{GHz}\cdot(n-\delta_{njl})^{-3}\ . \tag{2.7}$$

For the 40S Rydberg state, for example, the hyperfine constant is $A_\mathrm{HF} = 339\,\mathrm{kHz}$.
Again the basis of the uncoupled states $|I, m_\mathrm{I}\rangle \otimes |J, m_\mathrm{J}, L, S\rangle$ is not the eigenbasis any more and a new total angular momentum $\mathbf{F} = \mathbf{I} + \mathbf{J}$ has to be introduced. The eigenbasis of the system can again be constructed from the uncoupled states by forming linear combinations:

$$\begin{aligned} |F, m_\mathrm{F}, I, J\rangle &= \sum_{m_\mathrm{I}, m_\mathrm{J}} \langle I, m_\mathrm{I}, J, m_\mathrm{J}|F, m_\mathrm{F}, I, J\rangle \cdot |I, m_\mathrm{I}, J, m_\mathrm{J}\rangle \\ &= \sum_{m_\mathrm{I}, m_\mathrm{J}} c_{I,m_\mathrm{I},J,m_\mathrm{J}} \cdot |I, m_\mathrm{I}, J, m_\mathrm{J}\rangle\ . \end{aligned} \tag{2.8}$$

Here $c_{I,m_\mathrm{I},J,m_\mathrm{J}}$ are called the Clebsch-Gordon coefficients. With the quantum number F it is possible to rewrite the Hamiltonian in equation (2.6) by using $2\,\mathbf{I}\cdot\mathbf{J} = \mathbf{F}^2 - \mathbf{I}^2 - \mathbf{J}^2$.

$$\hat{H}_{\mathrm{HF}} = \frac{A_{\mathrm{HF}}}{2}\ (F(F+1) - I(I+1) - J(J+1)) \tag{2.9}$$

In the experiment ^{87}Rb atoms are excited from the $5S_{1/2}$ ground state to the $nS_{1/2}$ Rydberg state. The nuclear spin I of ^{87}Rb is 3/2 and for the studied S-states the total angular momentum of the electron is given by $J = S = 1/2$. With this we get two possible values for the total angular momentum: $F = 2$ or $F = 1$. The energy levels of the F-states are then shifted by ΔE from the uncoupled value calculated by equation (2.2).

$$\Delta E = \begin{cases} \frac{3}{4} A_{\mathrm{HF}}, & F = 2 \\ -\frac{5}{4} A_{\mathrm{HF}}, & F = 1 \end{cases} \tag{2.10}$$

These hyperfine states also have sub-states, which are labelled according to their magnetic quantum number m_{F}. The magnetic sub-states are degenerate in zero magnetic field. An applied external magnetic field lifts this degeneracy as the different sub-states shift differently in the magnetic field.

2.3. Atoms in an external magnetic field

In the absence of an external magnetic field, the $2F+1$ magnetic sub-states of the hyperfine energy levels are degenerate. By applying an external field this degeneracy is lifted because the m_{F} sub-states have a different projection of the angular momentum on the magnetic field direction and as such different interaction strengths. The Hamiltonian describing the interaction with the magnetic field is given by

$$\hat{H} = \frac{\mu_{\mathrm{B}}}{\hbar}\ (g_{\mathrm{s}}\,\mathbf{S} + g_{\mathrm{L}}\,\mathbf{L} + g_{\mathrm{I}}\,\mathbf{I}) \cdot \mathbf{B}\ . \tag{2.11}$$

Here $\mu_{\mathrm{B}} = 9.274\,\mathrm{J/T}$ is the Bohr magneton and all the g's are the Landé g-factors of the respective angular momenta. The values of the g-factor for the different angular momenta are $g_{\mathrm{L}} = 1$ for the orbital angular momentum, $g_{\mathrm{S}} = 2.002319$ [47] for the spin and $g_{\mathrm{I}} = -0.000995$ [47] for the nuclear spin.
If the magnetic field is small enough compared to the hyperfine coupling, it can be treated as a perturbation of the $|F, m_{\mathrm{F}}, I, J\rangle$ states. In this case F stays a good quantum number and the Hamiltonian can be simplified to

$$\hat{H} = \frac{\mu_{\mathrm{B}}}{\hbar}\, g_{\mathrm{F}}\ \mathbf{F} \cdot \mathbf{B} = \mu_{\mathrm{B}}\, g_{\mathrm{F}}\, m_{\mathrm{F}} B_{\mathrm{z}}\ , \tag{2.12}$$

with the quantization axis along the z-axis. In this equation g_{F} is the Landé g-factor of the total angular momentum F, which can be calculated according to [47]

$$g_{\mathrm{F}} = g_{\mathrm{J}}\ \frac{F(F+1) - I(I+1) + J(J+1)}{2F(F+1)} + g_{\mathrm{I}}\ \frac{F(F+1) + I(I+1) - J(J+1)}{2F(F+1)}\ . \tag{2.13}$$

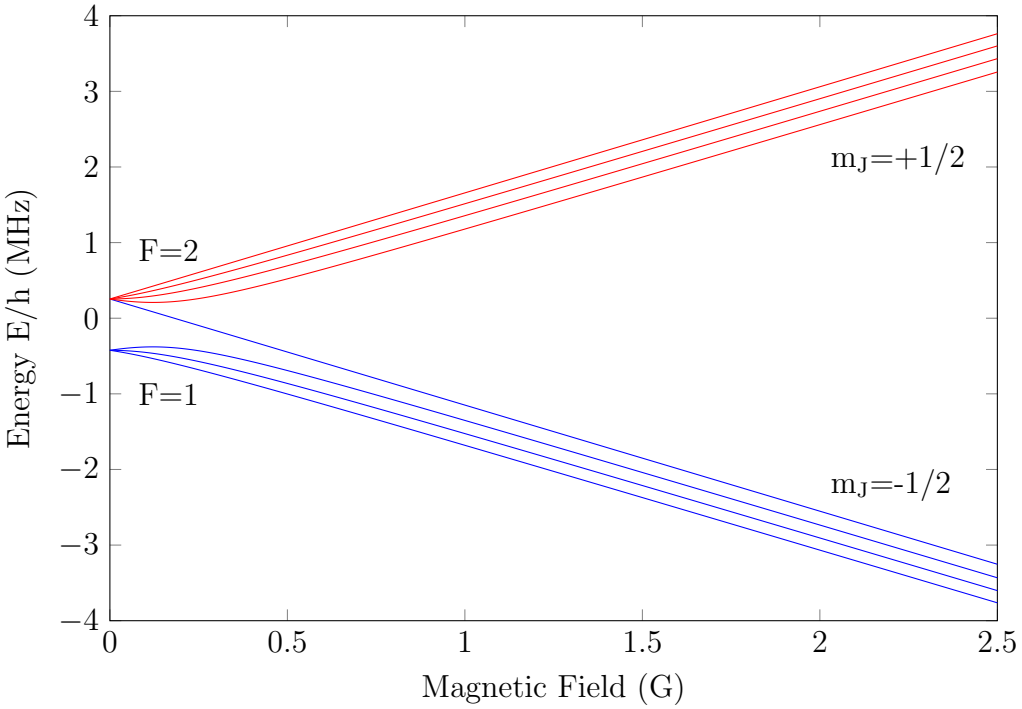

Figure 2.1.: Hyperfine structure of the 40S state of ^{87}Rb in an external magnetic field. For low magnetic fields the states are grouped according to their quantum number F and for higher fields they are grouped according to their value of m_J.

Since the second term in this equation is only on the order of 0.1% it is neglected in most cases. As such, small magnetic fields lead to a linear shift of the m_F sub-levels in an external magnetic field. This is the case for the $5\mathrm{S}_{1/2}$ ground state of ^{87}Rb with the achievable magnetic fields in the experiment.

For the Rydberg states already a small magnetic field, like the offset field in a magnetic trap, is strong compared to the hyperfine splitting. This means that the interaction with the external magnetic field dominates and the hyperfine splitting can be treated as a perturbation of the $|I, m_\mathrm{I}, J, m_\mathrm{J}\rangle$ states. In this case J stays a good quantum number as long as the interaction with the magnetic field stays smaller than the splitting of the spin-orbit coupling. This is called the Paschen-Back or strong B-field regime of the hyperfine interaction, for which the Hamiltonian in equation (2.11) can be written as

$$\hat{H} = \frac{\mu_\mathrm{B}}{\hbar} \left(g_\mathrm{J}\,\mathbf{J} + g_\mathrm{I}\,\mathbf{I}\right) \cdot \mathbf{B} = \mu_\mathrm{B} B \left(g_\mathrm{J}\, m_\mathrm{J} + g_\mathrm{I}\, m_\mathrm{I}\right) \,. \tag{2.14}$$

The Landé-g-factor for the total angular momentum of the electron in this equation is given by

$$\begin{aligned} g_{\mathrm{J}} &= g_{\mathrm{L}} \frac{J(J+1) - S(S+1) + L(L+1)}{2J(J+1)} + g_{\mathrm{S}} \frac{J(J+1) + S(S+1) - L(L+1)}{2J(J+1)} \\ &\simeq 1 + \frac{J(J+1) + S(S+1) - L(L+1)}{2J(J+1)} \,. \end{aligned} \tag{2.15}$$

The approximate expression above is obtained by using $g_{\mathrm{S}} = 2$ and $g_{\mathrm{L}} = 1$.
The complete dependency of the magnetic field for the hyperfine structure of the 40S Rydberg state is shown in figure 2.1. As can be seen, only for very small fields, the hyperfine basis is the correct description of the system, as already the necessary offset field of roughly 1 G in a magnetic trap is enough to be in the strong B-field or Paschen-Back regime. This means that the hyperfine structure can be neglected in most cases when dealing with Rydberg states.

2.4. Atoms in an external electric field

External electric fields also have an influence on the electronic level structure of atoms. The interaction with an external electric field $\mathbf{E}$ is described by the Hamiltonian

$$\hat{H} = -\mathbf{p} \cdot \mathbf{E} \,, \tag{2.16}$$

with the electric dipole moment $\mathbf{p}$. If an electronic state of an atom has an electric dipole moment the energy level therefore shifts linearly with the electric field amplitude. Spherically symmetric S-states, as studied in this thesis, however, do not have a permanent electric dipole moment. For these states the electric field first has to induce a temporary dipole moment in the atom, which is described by the polarizibility α of the atomic state. The electric dipole moment is then given by

$$\mathbf{p} = \alpha \, \mathbf{E} \,. \tag{2.17}$$

With this induced dipole moment the shift of the energy levels is then given by

$$\Delta E = -\frac{1}{2} \alpha \, \mathbf{E}^2 \,. \tag{2.18}$$

For Rydberg states the polarizibility scales with n^{*7} as can be seen in table 2.1 and as such, small electric fields can induce a large electric dipole moment and shift the electronic energy levels considerably.
In figure 2.2a the theoretically calculated energy levels close to the 40S Rydberg state in an external electric field are shown. It can be seen that the states of the nearest hydrogenic manifold (labeled as 37L in the figure) show a linear shift with the electric field. The quadratic shift of the S-state is not visible on the scale shown in the figure, but it is clearly visible in the measurement shown in figure 2.2b. There, already a small electric field leads to a shift of the atomic resonance of several MHz. This shift is even stronger for states

with a higher principal quantum number n due to the strong scaling of the polarizibility with n^{*7}. In figure 2.2b it is also visible that the parabola is not centered perfectly around zero electric field, due to the presence of stray electric fields in the experimental chamber leading to the necessary compensation field.
So in order to measure Rydberg states in the experiment, good electric field control and compensation of electric stray fields is necessary. This is achieved with electric field plates close to the atomic cloud. It is also important to have a homogeneous electric field over the whole atomic cloud, as gradients in the electric field lead to a broadening of the transition line in the spectrum. Since the shift and the broadening of the atomic resonance depends strongly on the principal quantum number, these effects are more pronounced than the other broadening mechanisms in the experiment, e.g. the Doppler broadening due to the finite temperature of the atomic cloud or the broadening due to the finite lifetime of the Rydberg state, for high principal quantum numbers. This puts a limit to the principal quantum number of the Rydberg state that can be observed in the experiment. In the described experiment this is about $n \approx 149$, for which it is already necessary to compensate the electric stray fields on a hourly basis.

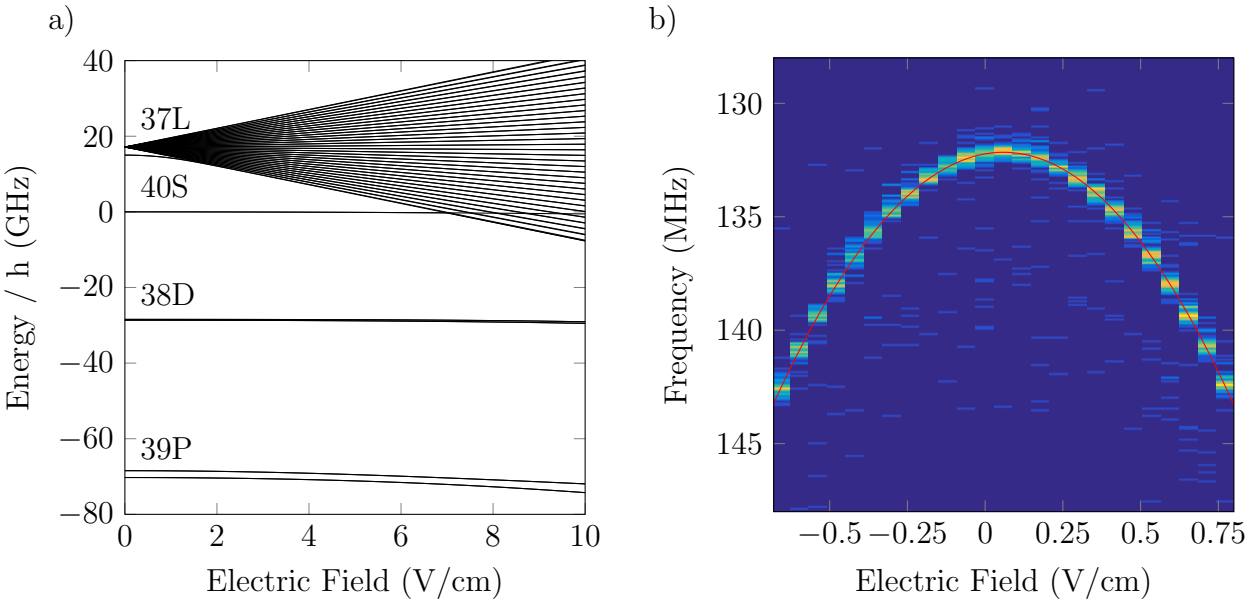

Figure 2.2.: Theoretical energy level structure of the Rydberg states close to the 40S state in an external electric field (a) and measured quadratic Stark shift of the studied S-states, shown exemplary for the 44S state (b)

2.5. Field Ionization

Applying even stronger electric fields can be used in order to ionize the Rydberg atom by removing the electron from attractive Coulomb potential of the ionic core. This can be used to detect Rydberg states by field ionization and subsequent detection of the positive ion with an ion detector, such as a multi-channel plate (MCP) or a Channeltron. The basics of the field ionization process will be discussed purely classically in the following. The potential $V(x,y,z)$ describing the system can be obtained through the sum of the Coulomb-potential of the core and the potential of the electric field.

$$V(x,y,z) = -\frac{e^2}{4\pi\epsilon_0\sqrt{x^2+y^2+z^2}} + e\,E\,z \tag{2.19}$$

In this equation $r = \sqrt{x^2+y^2+z^2}$ is the distance from the core, z is the coordinate in the direction of the electric field and E is the amplitude of the electric field.

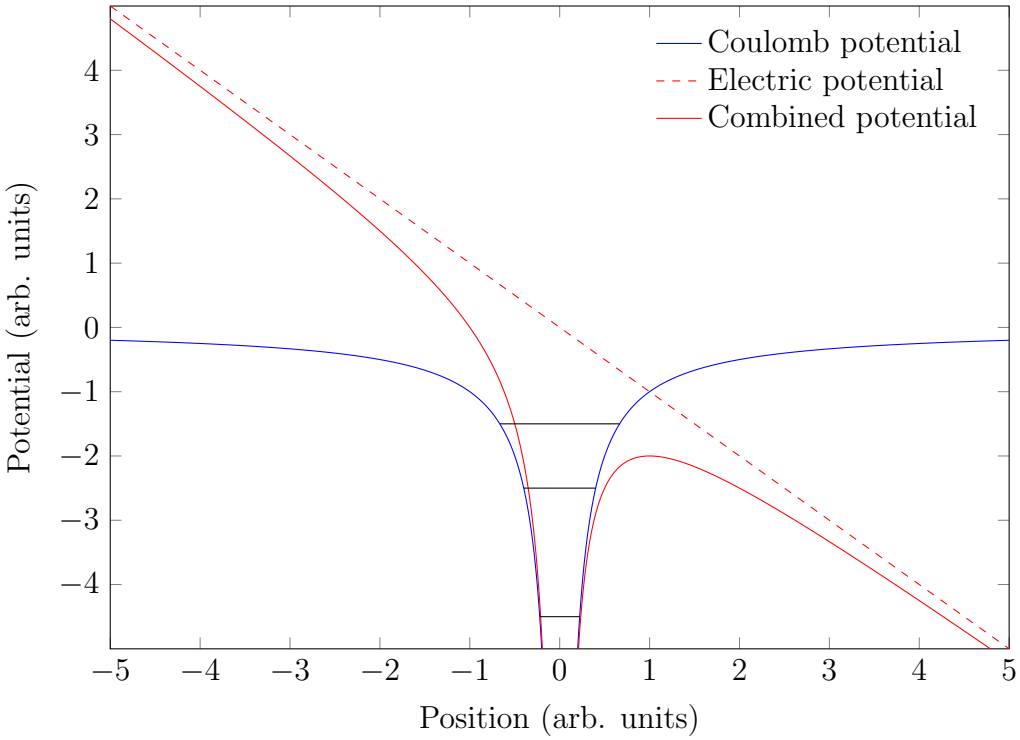

Figure 2.3.: Electric field potential (red dashed line), Coulomb potential (blue line) and combined potential (red line) shown as function of the distance from the ionic core in arbitrary units. For the Coulomb potential three possible bound states of the electron are shown by the black lines in the potential well. For the combined potential one of these states is not bound anymore and is therefore ionized.

In figure 2.3 these potential energy curves are shown separately as well as combined. There one can see, that the combined potential shows a local maximum. The position of this local maximum is given by

$$z_{\max} = \sqrt{\frac{e}{4\pi\epsilon_0 E}} \,. \tag{2.20}$$

Only states with a binding energy E_{nlj} lower than the potential at the local maximum $V(0,0,z_{\max})$ are classically bound. This is also shown schematically in figure 2.3: Only the two lower of the shown bound states are still bound in the combined potential while the highest one is not bound anymore and is therefore ionized. In order to ionize a state with the binding energy E_{nlj} an electric field of

$$E = \frac{\pi\epsilon_0}{e^3} \frac{R_\infty^{*2}}{n^{*4}} \tag{2.21}$$

is necessary. This expression for the necessary electric field is only correct for states with $m_{\mathrm{L}} = 0$. For states with a higher orbital angular momentum a centrifugal barrier is added to the Coulomb potential, which increases the necessary electric field. For states with a high angular momentum this can lead to electric fields necessary for the ionization, that are up to a factor of 2 higher than the one calculated in equation (2.21) [65].
In these equations the Stark shift of the electronic energy levels was not considered up to now. For states in the hydrogenic manifold there are red Stark states, for which the binding energy increases in the electric field, as well as blue Stark states, for which the binding energy decreases. Blue and red Stark state of the same hydrogenic manifold often have a necessary ionization field which differs by a factor of 2 [65].
Up until now this whole consideration of the field ionization was done purely classical. Quantum mechanically the electron can tunnel through a potential barrier with a finite probability. This can lead to field ionization for smaller electric fields than given in expression (2.21) of this section [65].

3. Experimental Setup

In the experiment Rydberg states are excited in an ultra-cold thermal gas or a Bose-Einstein condensate (BEC) of ^{87}Rb atoms. In order to achieve these dense atomic samples an ultra-high vacuum is necessary to reduce the interaction with the background gas leading to heating and loss of the atoms.
To get reasonable repetition rates of the experiment a two chamber setup is used: A magneto-optical trap (MOT) is prepared in a chamber with higher pressure, while the actual experiments with the cold thermal cloud or the BEC are done in an ultra-high vacuum chamber. The two chambers are connected by a small tube which allows differential pumping, resulting in a pressure difference on the order of two magnitudes between the two chambers. In between the two chambers the atoms are transported through the tube using the principle of magnetic transport.
In this section the experimental setup is described briefly (for more information see [8, 9, 10, 11, 12, 13]). To achieve a better stability of the electric field compensation and in order to study new aspects of Rydberg physics, a new electric field compensation box was designed in the course of the master thesis from Udo Hermann [10]. In the scope of this thesis a lot of work was done towards a setup for testing this new box and as such the changes between the new and old field compensation boxes will be discussed.

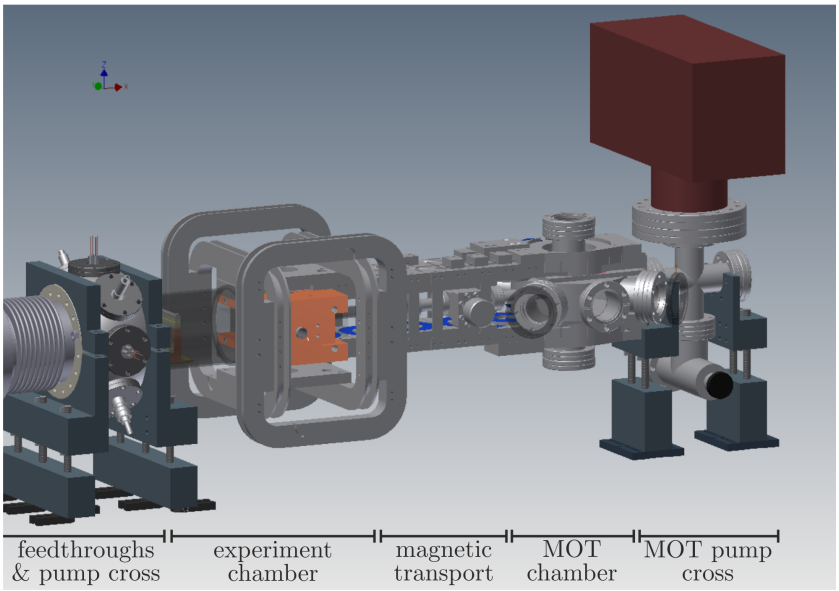

Figure 3.1.: Engineering drawing of the two-chamber setup of the experiment with the different section designated below

3.1. Setup

3.1.1. MOT chamber

The first step in order to obtain an ultra-cold atomic gas in the experiment is the preparation of a MOT [51]. This is done in the first of the two chambers, the so called MOT chamber. The Rubidium atoms are obtained from a reservoir connected to the MOT chamber with a valve mounted in between to control the flow of Rubidium atoms into the chamber. The emerging equilibrium of the flow of new atoms and the atoms lost through the vacuum pump leads to a background pressure of Rubidium of approximately 10^{-9} mbar inside of the MOT chamber.
In order to create a MOT, it is necessary to have a magnetic quadrupole field together with three orthogonal pairs of counter-propagating laser beams. To cool the atoms, the laser beams have to be red detuned from the atomic transition that is used for the cooling. The atoms are moving with their thermal velocity and due to the Doppler effect they see different frequencies if they are moving in the direction of the beam or in the opposite direction. Because of the red detuning of the laser beams, the atoms moving in the opposite direction of the beam absorb a photon with a higher probability. When an atom absorbs a photon it is excited to a higher laying state and its momentum in this direction is reduced by $\hbar k$, where $k = 2\pi/\lambda$ is the the wavenumber of the laser. The excited state has a finite lifetime and the subsequent spontaneous emission returning the atom to the ground state occurs in a random direction. The emission of a photon leads to a recoil, which adds a momentum of $\hbar k$ to the momentum of the atom. As such, after many scattering events, the sum of all the momenta from the spontaneous emission is zero, due to the random direction of the emission. The momentum from the absorption on the other hand always occurs in the same direction and therefore always reduces the momentum in one direction. By applying red detuned laser beams from all six spatial directions it is possible to decelerate the atoms and cool them down.
For this cooling process, the $5S_{1/2}$, F=2 $\longrightarrow$ $5P_{3/2}$, F=3 transition is used in the experiment. Due to off-resonant excitation there will also be some population in the $5P_{3/2}$, F=2 state, which can spontaneously decay to the $5S_{1/2}$, F=1 state. Atoms undergoing this transition would be lost to the cooling process. To avoid these losses to the cooling cycle a second laser is used as a repumper in order to optically pump the atoms back.
In order to spatially trap the atoms as well as cooling them a slightly different process has to be done. Adding a magnetic quadrupole field leads to a linear splitting of the m_F sub-levels of the $5P_{3/2}$ state as a function of the distance from the trap center. Due to the red detuning of the laser beams the transition will become resonant as an atom moves away from the center of the trap. By choosing the appropriate $\sigma^{\pm}$-polarization for the counter-propagating laser beams, the atoms will receive a 'kick' with a higher probability towards the center of the trap when they absorb a photon. This leads to a force acting on the atoms which is always pointing to the trap center, effectively trapping them.
In the experiment the loading of the MOT takes roughly 6 s and results in a few billion trapped atoms with a temperature of roughly 200 µK. To further cool down the atoms

the magnetic field is switched off and the optical molasses technique [51] is used. This decreases the temperature down to approximately 50 µK. As a last step all the atoms in the MOT chamber are optical pumped to the $5S_{1/2}$, F=2, m_F=2 sub-level, in order to get all the atoms in the low-field seeking state necessary to trap them in a magnetic trap used in the next step to transport the atoms to the experiment chamber.

3.1.2. Magnetic transport

As described in the theory section, the energies of the m_F sub-states of an atom are shifted in an external magnetic field. This energy shift is linear with B if the magnetic field is small compared to the hyperfine splitting, which is the case for the $5S_{1/2}$ ground state and the magnetic field used in the experiment. Therefore an extremum of the magnetic field can lead to a trapping potential for atoms prepared in the right sub-state: a minimum in the magnetic field for low-field seeking states and a maximum for high-field seeking states. In the experiment a local minimum is used and as such the atoms have to be in a low-field seeking state, for which the energy decreases with decreasing magnetic field. A low-field seeking state is for example the $|F = 2, m_F = 2\rangle$ of ^{87}Rb in which the atoms were prepared using optical pumping as a last step inside the MOT chamber.
The atoms are transferred from the MOT into a magnetic trap generated by coils in an anti-Helmholtz configuration. To transport the atoms from the MOT chamber to the glass cell with the electric field compensation chamber the position of the local minimum of the magnetic field is moved by turning on and off the coils along the path of the magnetic transport. This shift in the position has to be slow enough in order for the atoms to follow adiabatically.
To achieve this shift of the position in the experiment twelve pairs of coils in an anti-Helmholtz configuration are mounted below and above the tube connecting the two chambers. With the right sequence of current through these coils the minimum of the magnetic field can then be shifted along the tube.
During the 1.4 s of the transport process about 50% of the atoms are lost by the efficiency of the loading into the magnetic trap and then through the transport itself. Still roughly $2 \cdot 10^9$ atoms with a temperature of about 400 µK arrive in the experimental chamber.

3.1.3. Experiment chamber

The actual Rydberg excitation experiments are done in an experimental chamber, consisting of the electric field compensation plates and the ion detectors, which is placed inside the glass cell. The glass cell allows for good optical access and also a more compact design, which means that less current is needed in the coils used for generating the magnetic trap. After the magnetic transport the atoms are loaded into a QUIC-trap [50], consisting of a quadrupole field made by two coils in an anti-Helmholtz configuration and a Ioffe coil. The setup of these coils is shown in figure 3.2a.
The coils in the QUIC-trap configuration generate a nearly harmonic trap with a non-zero trap bottom, at a slightly different position than the anti-Helmholtz configuration.

a)

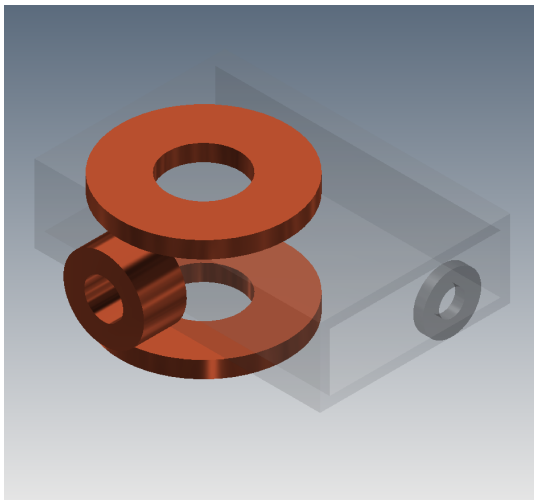

b)

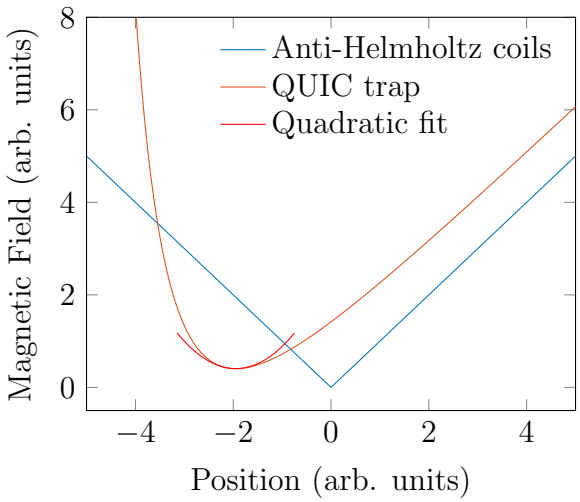

Figure 3.2.: a) Engineering drawing of the QUIC trap consisting of two coils in an anti-Helmholtz configuration (coils on top and bottom) and the Ioffe coil positioned on the front side of the shown glass cell. b) Amplitude of the magnetic field plotted against the position for coils in an anti-Helmholtz configuration (blue) and then with the added Ioffe coil resulting in the QUIC trap configuration (orange). The red line shows a harmonic fit function, coinciding with the magnetic field in the important part of the trap close to the center.

The magnetic fields of the QUIC-trap compared to the anti-Helmholtz configuration is shown in figure 3.2b. The non-zero magnetic field of the trap bottom is necessary to prevent majorana spin-flip transitions to states that are not trappable, which would lead to atom loss from the trap. Since the current needed for the trap configuration used in the experiment is 40 A, all coil holders for the QUIC-trap are water cooled in order to transport the heat away.

Furthermore, offset coils consisting of a pair of coils in Helmholtz configuration for each spatial direction, are mounted around the glass cell. With these coils it is possible to move the trap position in all spatial directions.

The QUIC-trap configuration used in the experiment results in a cigar-shaped trap, with trap frequencies of $\omega_{x,z} = 2\pi \cdot 200\,\mathrm{Hz}$ and $\omega_y = 2\pi \cdot 15\,\mathrm{Hz}$. A measurement of the trap frequency in the x-direction is shown in figure 3.3. For this measurement a BEC was prepared in the trap and then a short magnetic field pulse, created with one of the offset coils, pushed the atoms about 100 µm in the x-direction. Subsequently the atoms were oscillating inside of the trap. In order to measure this oscillation, the atoms were left alone for a wait time and then the trap was switched off and the atoms imaged in time-of-flight. In order to obtain the points shown, the hold time in the trap was varied from cloud to cloud and the center position determined from a bimodal fit (Thomas-Fermi + thermal density distribution) to the density distribution of the imaged BEC. In addition each point

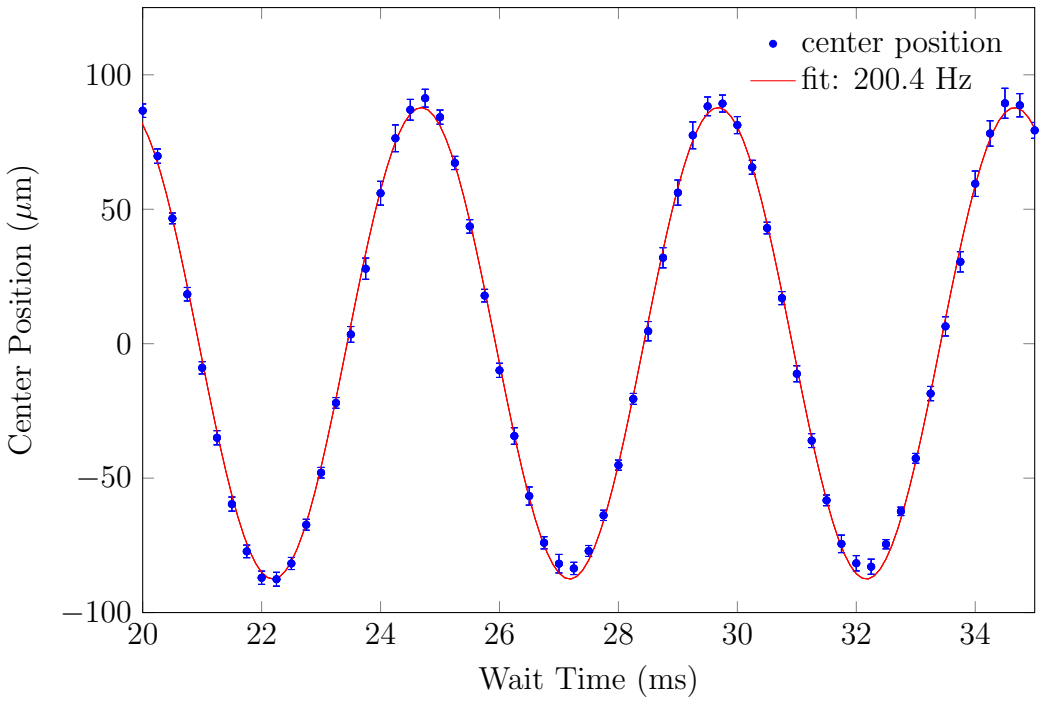

Figure 3.3.: Measurement of the trap frequency along the x-direction in the QUIC trap. For the measurement the BEC was pushed to the side of the trap with a small magnetic field pulse and then it was allowed to oscillate freely in the trap for a certain wait time. The trap was then switched off and the cloud imaged after 28 ms time of flight. The center position of the BEC was determined from a bimodal fit to the imaged density distribution of the BEC. The trap frequency of 200.4 Hz is then obtained with a sinusoidal fit (red line).

was averaged for several atomic clouds and the error from the mean value is shown in the error bars. An oscillation with a frequency of 200 Hz is clearly visible in the measured center position of the imaged condensates, directly corresponding to the trap frequency along the measurement axis.

The atoms arriving in the magnetic trap after the magnetic transport still have a temperature of roughly 400 µK. So in order to get ultra-low temperature thermal gases or even BECs an evaporative cooling technique is applied. The principle behind this technique is the removal of the hot atoms of the atomic cloud with a radio-frequency (RF) so that after a re-thermalization, the temperature of the cloud is reduced. To do this the radio-frequency has to transfer the atoms from the low-field seeking $|F = 2, m_F = 2\rangle$ state to a state that is not trapped anymore, so either one of the following $|F = 2, m_F = 0, -1, -2\rangle$. A high frequency will remove the atoms which are furthest away from the trap center, which are also the hottest atoms, because there the magnetic field is higher and as such also the splitting between the magnetic sub-states. By ramping down the evaporation frequency the remaining atoms in the trap get cooled down and at the same time the density increases.

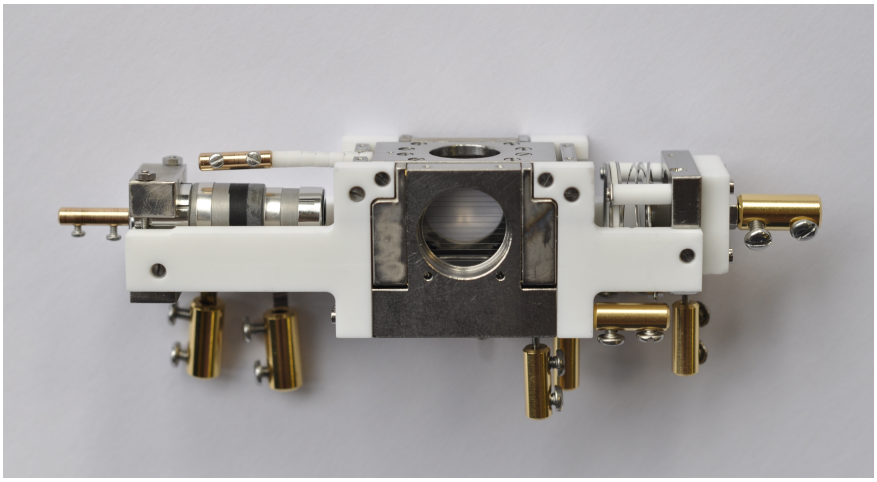

Figure 3.4.: Electric field compensation chamber of the experiment, consisting of six electric field plates made of titanium separated by Macor pieces. The micro-channel plate (right side) and Channeltron (left side) for the ion detection are also mounted to the Macor pieces.

In the experiment the evaporation cooling is done with three linear ramps, starting with a frequency of 45 MHz and depending on the trap bottom ending at roughly 1 MHz. In the experiment the evaporation cooling process takes about 16 s, which is roughly half the time of a complete cycle.
In order to do Rydberg excitation experiments, a good control of the electric field in the experiment chamber is necessary. Due to the Stark-effect, which was discussed in the theory section 2.4, the atomic energy levels shift in the presence of an electric fields. This is especially important for Rydberg states because of the strong scaling of the polarizibility with the principal quantum number n. For this the electric field compensation chamber (see picture in figure 3.4) is placed inside the glass cell with its center coinciding with the position of the magnetic trap. This electric field control box was designed in the course of the master thesis of Christph Tresp [11] and consists of six electric field plates used to compensate electric stray fields and also for the ionization of the created Rydberg atoms. Every field plate has a hole in the middle to either provide optical access for the excitation and imaging lasers or to allow the produced ions to hit the ion detectors mounted on the left and right side of the box shown in figure 3.4. The electric field plates are made of titanium and titanium wires are placed across each hole in order to shield electric stray fields from the outside. The individual plates are separated by isolating Macor pieces. Missing in the picture is the RF-coil for the evaporative cooling, which is mounted around the Channeltron.
After compensating the electric stray fields by applying compensation voltages to the field plates, it is possible to do high resolution spectroscopy of the Rydberg states. To excite the atoms to a Rydberg state the inverted excitation scheme is used[1], meaning that we

[1]For more information see appendix A.2

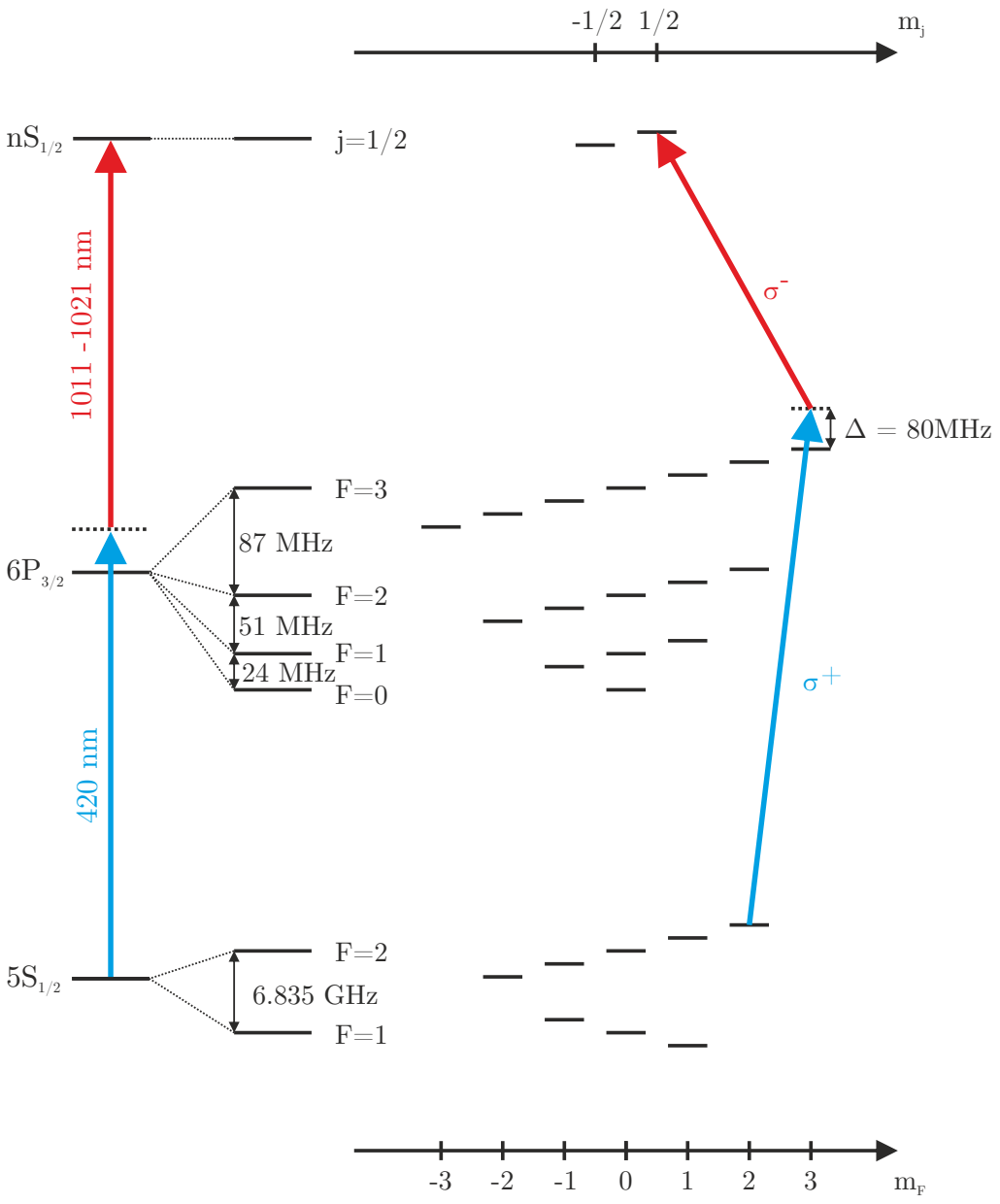

Figure 3.5.: Excitation scheme of the Rydberg excitation used in the experiment. The atomic cloud in the magnetic trap is spin polarized in the $F = 2, m_F = 2$ ground state. From there the excitation to the $nS_{1/2}$ Rydberg state is done via the stretched state $m_F = 3$ of the $6P_{3/2}$ state with σ^+-polarized 420 nm light and σ^--polarized 1020 nm light. With this scheme the Rydberg electron has the same spin direction as the ground state atoms, resulting in pure triplet scattering interactions between the Rydberg electron and neighboring ground state atoms.

excite the atoms from the $5S_{1/2}$ ground state with a 420 nm laser to the $6P_{3/2}$ intermediate state and then with a 1010-1020 nm laser to the $nS_{1/2}$ Rydberg state. The scheme of the Rydberg excitation is shown in figure 3.5. The polarization of the laser beams are chosen such that the atoms are always in the stretched state, which conserves the spin of the Rydberg electron with respect to the spin-polarized ground state atoms.
For the Rydberg excitation in the experiment, the 420 nm laser illuminates the whole atomic cloud, while the 1020 nm laser is focused down into the atomic cloud using an aspheric lens (Asphericon A15-12HPX-S-U). This aspheric lens is mounted to one of the electric field plates close to the atoms. With this it is possible to excite a single Rydberg atom inside the atomic cloud if the blockade-radius r_B is larger than the size of the focus. In the direction of the focused beam it is still possible to excite multiple Rydberg atoms, however, the excitation probability decreases because the intensity of the laser decreases away from the focus. The focused excitation also ensures a good localization of the Rydberg atom inside the cloud, since it can only be excited in the volume illuminated by both laser beams. A schematic drawing of the atoms in a BEC with the excitation laser beams is shown in figure 3.6. There the blockade radius for two different Rydberg states (53S and 111S) is also drawn to show that it is possible to only excite a single Rydberg atom in the whole BEC.

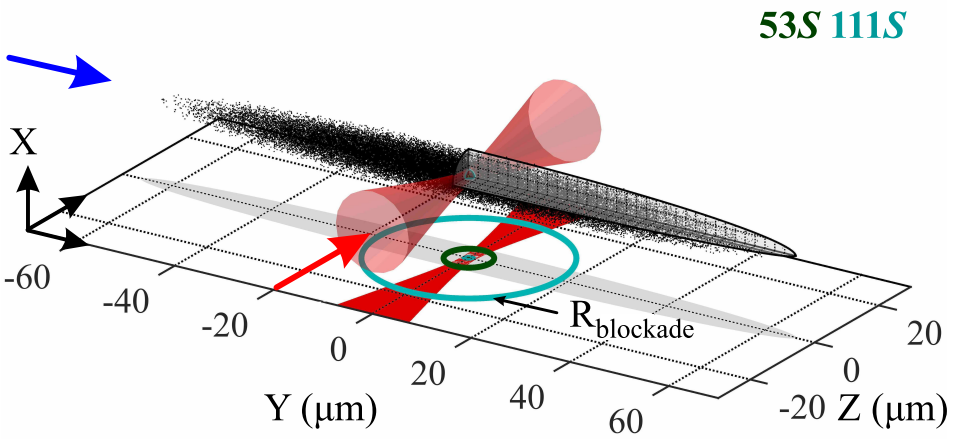

Figure 3.6.: Experimental setup of the BEC in the magnetic trap together with the two excitation laser. The 420 nm laser (blue arrow) has a beam waist of 2 mm and therefore illuminates the whole atomic cloud. The 1020 nm laser (red gaussian beam profile) is focused down to about 2.3 µm into the BEC using a high-NA aspheric lens.

In the course of this thesis the size of the focus after the high-NA aspheric lens was measured using a 500 nm pinhole. For this a test setup was built using the same optical elements as in the actual experiment, except for the glass cell and the wires placed over the lens. The measurement of the focal size is shown in figure 3.7. It is important to note that the lens is optimized for a wavelength of 780 nm, which is used for in-situ imaging of the atomic cloud. As such the 1020 nm beam shows a lot of aberrations after the lens. In order to

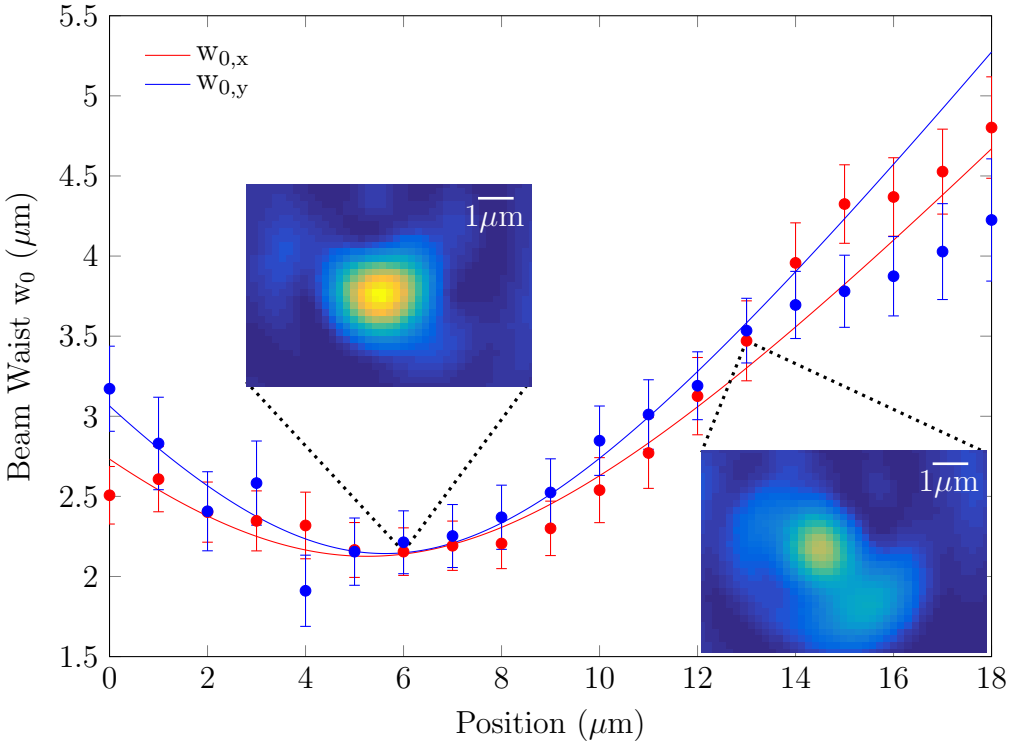

Figure 3.7.: Measurement of the focal size of the 1020 nm beam after the A15-12HPX aspheric lens in a test setup

get rid of these aberrations and to be able to move the position of the focus in the atomic cloud, it is planned to implement a spatial light modulator in the near future.
In order to detect the excited Rydberg atoms they are subsequently field ionized and the positive ions detected with an ion detector. For this a micro-channel plate (MCP) and a Channeltron are mounted to the electric field control box as can be seen in figure 3.4. Both detectors are built like an electron multiplier, with two electrodes connected by a glass tube. Between the two electrodes a high voltage on the order of 1-3 kV is applied. If a single electron or ion hits the wall of the glass tube, this leads to the emission of secondary electrons. These secondary electrons are accelerated due to the high voltage and will produce even more electrons if they hit the glass tube. This leads to an avalanche of electrons that can be measured, caused by a single initial electron or ion. This avalanche process leads to a dead time of the multiplier tube in which no other electron or ion can be detected. The Channeltron used in the experiment consists of six such electron multiplier channels, each with a diameter of about 1 mm. The built in Channeltron has a efficiency of about 90%. The MCP on the other hand consists of 10^6 channels with a diameter of 10 µm. This allows for the detection of many ions if they are spatially spread. In the presented measurements later in the thesis the MCP was used for the ion detection, which has an detection efficiency of 70%. Both ion detectors have a dark count rates of about $1\,s^{-1}$, which is negligible compared to the detection time of the ionized Rydberg atoms,

which is on the order of a few µs.
The process of excitation and ionization is repeated up to 5000 times in a single atomic cloud. Subsequently the magnetic field is switched off and the atomic cloud imaged after a certain time of flight, using absorption imaging tuned to the $5S_{1/2} \longrightarrow 5P_{3/2}$ transition. It is also possible to take in-situ images of the atomic cloud using phase-contrast imaging [52] instead of the absorption images in time of flight. The method of phase contrast imaging makes use of the different refraction index of the atomic cloud for different atomic densities. The different refractive index delays the light passing through, leading to a phase shift that is proportional to the density of the cloud. The whole experimental cycle takes around 30 s and is then repeated, starting again with the preparation of a MOT inside of the MOT chamber.

3.2. New experimental chamber

To improve the stability of the experiment and in order to study new aspects of Rydberg physics the experimental chamber has to be modified. For this reason a new electric field compensation box, with some additional features not described in the previous section, was designed in the course of the master thesis of Udo Hermann [10]. During this thesis a considerable work was done towards a test setup for this new box, as well as improving several other aspects of the experimental chamber. Another limiting factor of the stability of the experiment are fluctuations of the trap bottom. These fluctuations of the trap bottom can be caused by fluctuations in the current or the temperature of the coils of the QUIC-trap during one cycle or by a drift of the temperature over a longer time. For this reason a new setup of coil holders was designed to achieve better temperature stability. In the following section the major changes and improvements of the experimental chamber will be discussed.
As previously mentioned the electric field compensation box currently used in the experiment is made from titanium, which is non-magnetic and a good electrical conductor. The problem with this is that titanium oxidizes when it comes in contact with air, leading to the creation of titaniumoxide which is a semiconductor. This means that electrical charges, which are created by photo-emission caused by the 420 nm light used for the Rydberg excitation, can stick to the electric field plates, leading to unwanted perturbations of the electric field inside the box. These electric fields caused by the charges on the surface can not be compensated since they are changing randomly over time, leading to drifts of about 1-10 mV per hour for the necessary compensation voltage. For this reason the new electric field compensation box was made from stainless-steel (DIN 1.4404, AISI 316L). This stainless steel is a good electrical conductor, which does not oxidize and is nearly non-magnetic.
Another improvement for the electric field plates is that the holes in the direction of the ion detectors are not shielded by wires anymore, but only by cylinders around the hole of the field plates. These cylinders shield the high electric fields caused by the high voltages of the ion detectors even better than the shielding wires. Also no ions can be lost on the way

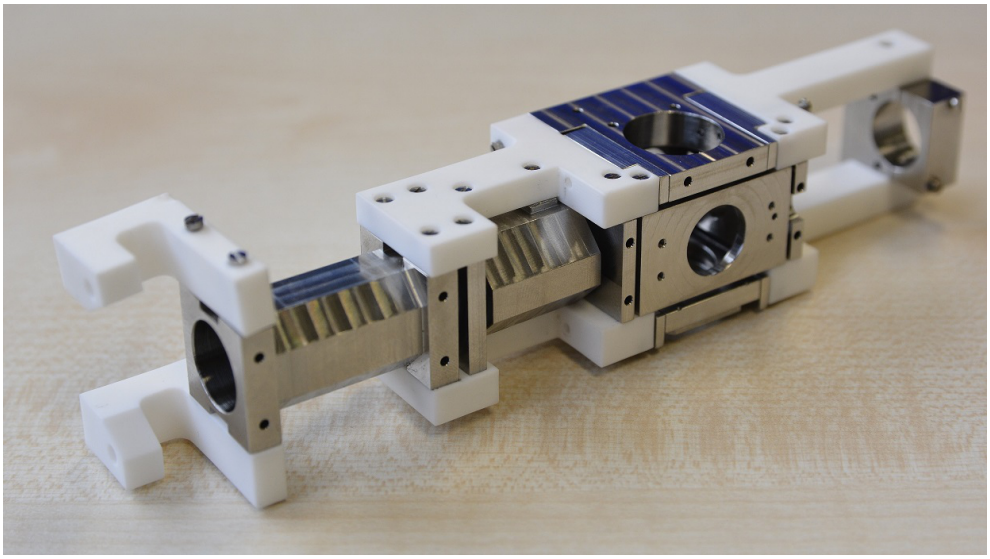

Figure 3.8.: New electric field compensation chamber with three additional tubes for the ion lensing in order to spatially spread the ions arriving on the MCP (left side, not mounted in the picture).

to the detectors in the new setup, by hitting one of the wires used for shielding the electric field. With these changes of the electric field plates, the stability of the electric field inside the chamber should improve. This should allow the excitation of Rydberg states with an even higher principal quantum number than $n \approx 150$, which we were limited to up to now.

For the new box, two of the electric field plates are connected with $50\,\Omega$ cables (and feedthroughs) in order to switch the voltage on a nanosecond time scale. With this it is possible to create fast electric field pulses, which can be used to generate circular Rydberg states. Circular Rydberg states are states with a high angular momentum m_{L}. For these states the electron orbital is nearly classical. This means that the electron moves only on a torus far away from the ionic core. Increasing the size of the torus by increasing the principal quantum number n means that the electron orbits only outside of the atomic cloud if the principal quantum number n is high enough, leading to the possibility to study the effect of a single ion inside the atomic cloud.

Around the cylinder for the shielding on the electric field plate close to the Channeltron, the coil for the radio frequency of the evaporative cooling was placed in the new design instead of around the Channeltron like in the old design. This means that less RF-power is necessary for the evaporative cooling, since the coil is already placed inside of the metal cage and the radiation will not have to get through the metal cage to reach the atoms. the metal cage of the field plates will also shield the RF radiation, so that outside the RF power will be a lot lower and as such not influencing other electronic devices anymore.

Another new feature are the three additional metal tubes between the MCP and the respective electric field plate, which are set up in an ion lensing configuration. With this it is possible to spatially spread the ions flying towards the MCP so that they hit the whole

area of the detector. In the old setup the MCP was placed directly after the field plate, which actually led to a focussing of the ions to a small area on the MCP. This means that only very few channels of the MCP were actually hit by ions, which is bad for the life time of the channels since they can only detect ions up to a certain point, which is given by the doping of the glass tubes. If this point is reached the detection efficiency of the channel decreases dramatically. This actually happened to the channels of the MCP that were hit by ions in the course of the thesis. In order to still use the MCP to efficiently detect ions an additional deflection voltage was used so that the ions hit a different spot on the detector. In the new design of the experiment box an ion lensing configuration was added, which spreads the ion so that an area roughly 100 times larger than for the old setup is hit on the MCP. This spatial spread also causes a spread in time, which means that if there are two ions at the same time the probability that they overlap becomes less likely. With this the detection of ions and as such the Rydberg atoms will become even more efficient than up to now.
The MCP built into the old setup was disassembled and a self-made backplate was used in the reassembling, because the space in the glass cell was not big enough for the standard backplate. As a result of this the impedance is not perfectly matched anymore, leading to reflections of the electric signal [66, 67]. This causes ringing on the signal of the detected ion, which can be seen for about 50 ns. In this time no other ions can be detected even if they hit another channel and should in principle be visible. For the new setup Hamamatsu offered a custom-made backplate, which means that the MCP did not have to be disassembled and modified by us. This means that for the new MCP the impedance is matched and there should be no ringing on the signal.
The position of the field compensation chamber inside the glass cell is adjusted by fixing

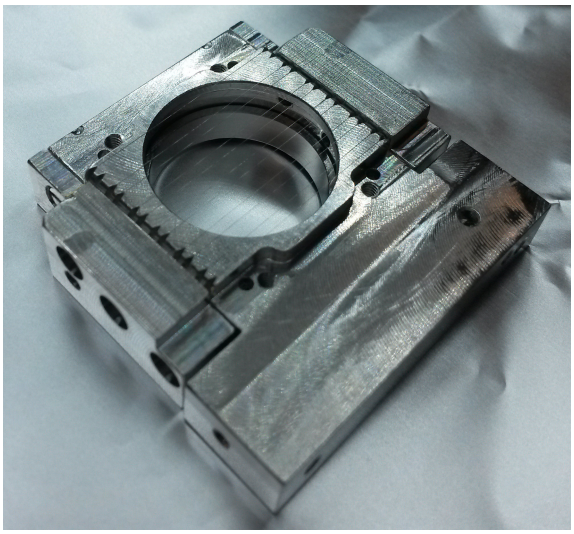

Figure 3.9.: Photo with a detailed view of the shielding wires. Stainless stell wires with a diameter of 25 µm are attached to the shown field plate to screen surface charges.

the cables with clamps. This is a tedious work since the cable clamps used in the current setup are hard to get to. For this purpose a new setup of cable clamps was designed. With this it should be easier to position the electric field compensation chamber inside the glass cell.

Before the new electrical field control box can be built into the experiment all the parts have to be tested. For this all the separate parts were cleaned for ultra-high vacuum and then assembled to the field compensation chamber. Also shielding wires (stainless steel DIN 1.4404, 25 µm diameter) were put over all the holes for the optical access, as can be seen for one of the field plates in figure 3.9. As a next step a vacuum test setup has to be built in order to test the electrical connections and the functionality of the MCP and the Channeltron.

To further improve the stability of the experiment the thermal stability of the coils for the QUIC-trap had to be improved. For this reason new coil holders for the quadrupole and Ioffe coils were designed during this thesis. The new coils are now split into different layers separated by a copper plate for better cooling. The quadrupole coils therefore consist of 2 times 2 layers each with 21 windings and the Ioffe-coil of 4 times 2 layers with 9 windings.

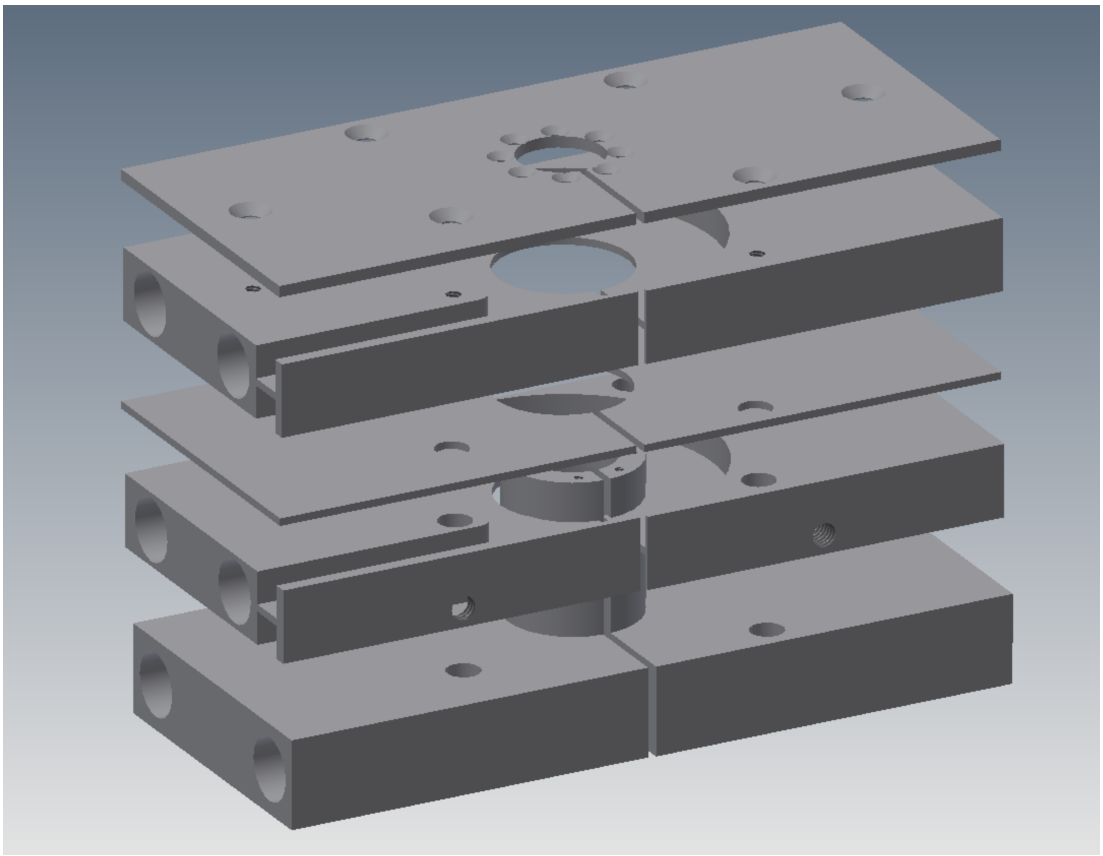

Figure 3.10.: Engineering drawing of the new coil holder for the Ioffe coil. The different layers of the coil holder are separated for better visibility.

Also the distance of 3.01 cm between the Ioffe-coil and the center of the trap was reduced by 1 mm, so that less windings were necessary. Calculations of the magnetic field generated by this configuration of coils lead to slightly changed trap frequencies of about $\omega_{x,z} = 2\pi \cdot 280\,\mathrm{Hz}$ and $\omega_y = 2\pi \cdot 16\,\mathrm{Hz}$. These trap frequencies are larger than the ones of the current setup, but it was already seen for the old setup that the calculation always results in slightly higher trap frequencies than the actual experiment. This could be because the actual coils are not perfectly constructed and also that the mounting most likely does not result in exactly the same distances as used in the calculation.
All in all the described changes should lead to an overall improvement of the stability of the experiment and at the same time allowing the study of new topics, like Rydberg states with an even higher quantum number or circular states.

4. Rydberg Molecules

Scattering experiments can provide valuable information about the interaction of the scattered particles. The electron of an atom in a Rydberg state is far away from the ionic core, which means that it can interact with neighbouring particles of a dense atomic sample. The scattering of the quasi-free Rydberg electron with neighbouring ground state atoms can lead to an attractive or repulsive interaction, depending on whether the electron-neutral atom scattering length is negative or positive. If the electron-atom scattering leads to an attractive potential, it is possible that the arising potential can sustain bound molecular states: the ultra-longrange Rydberg molecules.
The scattering process depends on the kinetic energy of the two particles [57] and on the relative spin configuration of the Rydberg electron and the electron of the ground state atom. For the Rubidium atoms used in the experiment, only the triplet scattering leads to an attractive potential. For this case the Rydberg molecules were first observed by Bendkowsky et al.[29]. However if the spins of the electron of the Rydberg state and the ground state are in a singlet configuration the arising potential is repulsive and therefore no bound molecular states can be sustained.
Recently it was pointed out by Anderson et al.[2] that the hyperfine coupling of the ground state of the neutral atom leads to a mixing of singlet and triplet scattering channels. This leads to changes of the pure triplet and singlet scattering potentials, resulting in the emergence of molecular states bound by mixed singlet-triplet scattering.
This chapter starts with the theory of Rydberg molecules, namely the process of photoassociation used to create the molecules in the experiment and the electron-atom scattering leading to the binding of the Rydberg molecules. Then the work done with Rydberg molecules up to this date will be presented briefly. In the next section the theory of the mixed singlet-triplet molecules will be discussed in detail. The chapter ends with the presentation of the spectroscopic observation of the molecules, comparing the experimental results to the presented theory.

4.1. Theory of Rydberg molecules

4.1.1. Photoassociation

The formation of a diatomic molecule from two separate atoms under the influence of resonant light is called photoassociation. During this process the distance between the two atoms does not change (Frank-Condon principle). For diatomic molecules made up of two ground state atoms, the bond length is on the order of $10\,a_0 \approx 0.5\,\mathrm{nm}$, which is

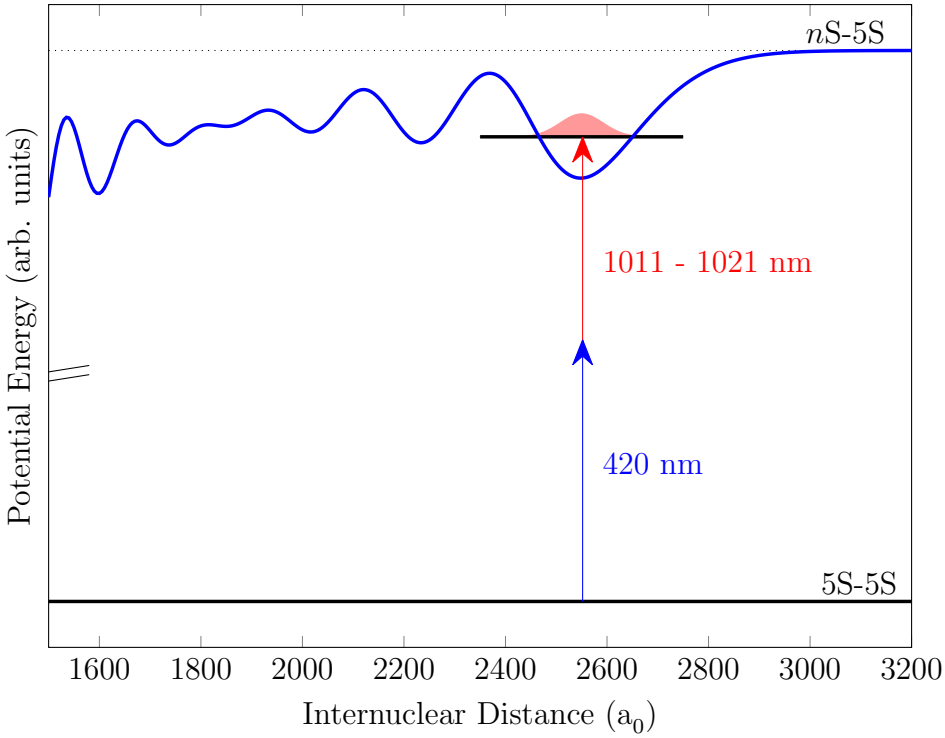

Figure 4.1.: Molecular potential curves in the region of interest. The interaction for two Rb 5S ground state atoms is really short range ($\lesssim 10\,a_0$) and is not shown here. In a dense atomic sample a configuration of two atoms with the right internuclear separation can be photoassociated into a nS-5S Rydberg molecule via the shown two photon transition. The atomic transition to the nS Rydberg state (dotted line) acts as the dissociation limit of the molecular potential.

considerably smaller than the interparticle distance in a dense atomic cloud. Because of this only high vibrational molecular states, with a large internuclear separation, can be photoassociated in these samples.

For Rydberg molecules this is different since the electron is far away from the core, with the orbital radius scaling as n^{*2}. The scattering of the Rydberg electron with ground state atoms can lead to an attractive potential and as such bound molecular states are possible. The bond length for these molecular states is on the order of $1000\,a_0$. This means that it is possible to directly excite the vibrational ground state of Rydberg molecules in cold atomic samples. As an example, figure 4.1 schematically shows the photoassociation process from two 5S ground state atoms to a nS-5S Rydberg molecule for Rubidium. The interaction between the two ground state atoms plays a role for distances on the order of $10\,a_0$, which is negligible for the interparticle distances of the cold atomic samples, and is as such not shown in the figure. An exemplary wavefunction of the molecular ground state in the nS-5S potential is also shown.

With photoassociation spectroscopy it is possible to measure absolute binding energies as

all molecular states appear red detuned from the atomic resonance of the respective Rydberg state with quantum number n, which is the dissociation limit of the nS-5S molecular potential. Thereby the molecular ground state corresponds to the peak with the highest red detuning in a spectrum, as it has a higher binding energy than the excited vibrational states which therefore appear closer to the respective atomic resonance. More atomic molecules, e.g. triatomic molecules, can appear for an even higher detuning from the dissociation limit.
The experimental resolution of the photoassociation spectroscopy is limited by three factors: the linewidth of the excitation laser, the Doppler broadening [58] and the population of different rotational states due to the thermal energy. The laser linewidth of the 420 nm and 1020 nm excitation laser used in the experiment are both below 20 kHz [12]. The next factor is the Doppler broadening of the transitions due to the movement of the atoms in the atomic cloud. For the temperature of roughly 1 µK used in the thermal cloud experiments, the Doppler broadening is about 25 kHz. The last factor is the population of different rotational molecular states due to the thermal energy of the atoms, which is transferred to an angular momentum J in the moment of the photoassociation of the molecule. The spectral spacing between different rotational states is quite small (on the order of 10 kHz) due to the large bond length, which gives a small rotational constant B. The intensity of the different rotational states in the spectrum is proportional to the degeneracy $(2J+1)$ of the rotational states and the Boltzmann distribution (for more information see [53]). For the parameters in the experiment, only the few lowest rotational levels are populated. All in all the resolution of the photoassociation spectroscopy should be better than 100 kHz, which was used as the step size for the excitation laser frequency in most of the measured spectra presented later in the chapter.

4.1.2. Electron - Atom Scattering

In absorption spectroscopy of alkali atoms excited to Rydberg states in an environment of a foreign background gas, Amaldi and Segrè found that the transition line was broadened and simultaneously shifted from the expected position [17]. This shift could not be explained by pressure broadening, as it also depends on the foreign gas itself. This density shift of the Rydberg line was explained by Fermi as the effect of the low-energy scattering of the Rydberg electron and the foreign gas atoms [18]. This is expressed in the famous Fermi-pseudopotential

$$V(\mathbf{r}) = 2\pi\, a_0\, \delta^{(3)}(\mathbf{r} - R\hat{\mathbf{z}})\,, \tag{4.1}$$

in which the scattering is treated as contact interaction described by the scattering length a_0. In this equation $\mathbf{r}$ is the position of the Rydberg electron and R is the internuclear distance measured along the $\hat{\mathbf{z}}$-axis. For the contact interaction in the Fermi-pseudopotential, the neutral atom as the perturber is treated as a point-like particle. Averaged over many electron-neutral atom scattering events, the arising potential is then proportional to the electron density $|\psi(\mathbf{r})|^2$ of the Rydberg state.

$$V(\mathbf{r}) = 2\pi\, a_0\, |\psi(\mathbf{r})|^2 \tag{4.2}$$

The assumption of many scattering events is valid because of the different time scales of the movement of the Rydberg electron compared to the neutral atoms. As it was pointed out by Chris Greene et al.[28], this potential can sustain bound molecular states if the thermal energy of the ground state atom is lower than the scattering interaction. The theory of the electron-atom scattering leading to these Rydberg molecules will be discussed in this section on the basis of [15] and [14]. If not stated otherwise atomic units ($\hbar = m = e = 1$) will be used throughout the whole section.
In order to quantum mechanically study the scattering of a particle by a potential $V(\mathbf{r})$, one has to solve the time-independent Schrödinger equation

$$\hat{H}\,\psi(\mathbf{r}) = \left(-\frac{1}{2}\nabla^2 + V(\mathbf{r})\right)\,\psi(\mathbf{r}) = E\,\psi(\mathbf{r}) \tag{4.3}$$

for the motion of the particle in the potential $V(\mathbf{r})$. In this equation $\hat{H}$ is the Hamiltonian of the system, E is the total energy and $\psi(\mathbf{r})$ is the wavefunction of the particle. For the discussion of the scattering process we will start with short-range potentials that are spherical symmetric and are vanishing faster than r^{-1} for $r \to \infty$. For the potential of interest for us, namely the polarization potential describing the interaction of a charged and a neutral particle, this discussion has to be slightly changed, because the potential asymptotically vanishes as r^{-4} and is as such considered as a long-range potential. The necessary changes for the long-range polarization potential will be described later on in this section.
For a spherically symmetric, short-range potential $V(\mathbf{r}) = V(r)$ the solution of the Schrödinger equation (4.3) can be written as

$$\psi(\mathbf{r}) \underset{r\to\infty}{\simeq} e^{ikz} + f(\theta,\phi)\,\frac{e^{ikr}}{r}\,. \tag{4.4}$$

In this equation the incoming wave is treated as a plane wave along the z-direction with the amplitude of the wavevector k given by $k^2 = 2E$ and the scattered wave as a spherical wave with an angular dependent scattering amplitude $f(\theta,\phi)$. The scattering problem is shown schematically in figure 4.2.
With this ansatz for the solution of the Schrödinger equation the differential cross section

$$\frac{d\sigma}{d\Omega} = |f(\theta,\phi)|^2 \tag{4.5}$$

and the total cross section

$$\sigma_{\text{tot}} = \int_0^{2\pi} d\phi \int_0^{\pi} d\theta\; sin(\theta)\; |f(\theta,\phi)|^2 \tag{4.6}$$

can be calculated from the scattering amplitude. The total cross section σ_{tot} is given in units of a_0^2, where a_0 is the Bohr radius, which is the unit of length in atomic units. In

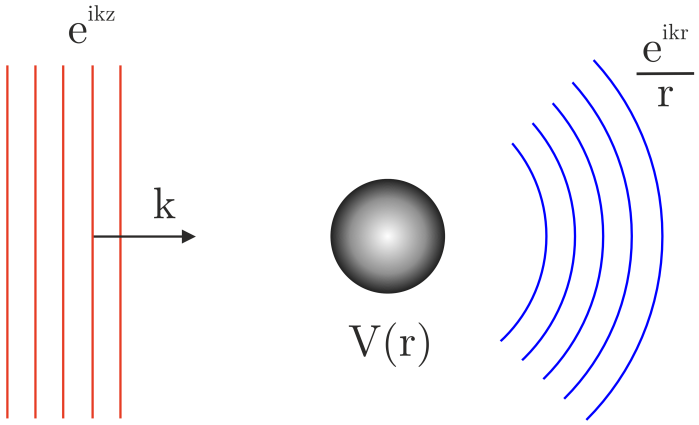

Figure 4.2.: Schematic illustration of the scattering process of a plane wave e^{ikz} by the spherical symmetric interaction potential $V(r)$ resulting in the scattered spherical wave e^{ikr}/r.

order to obtain the scattering amplitude $f(\theta,\phi)$, we have to solve the Schrödinger equation (4.3) with the correct boundary conditions for $\psi(\mathbf{r})$. The Schrödinger equation can be solved for low energy scattering by a partial wave analysis [20, 21].

$$\psi(\mathbf{r}) = \sum_{l=0}^{\infty} B_l(k)\,\frac{u_l(r)}{r}\,P_l(cos\theta) \tag{4.7}$$

In this equation l is the quantum number of the angular momentum of the scattered particle, $P_l(cos\theta)$ are the Legendre polynomials, $u_l(r)$ are the radial wave functions and $B_l(k)$ are the coefficients, which are obtained from the boundary conditions. Substituting this ansatz into equation (4.3), it is possible to separate the radial and angular dependency. With this we get the radial Schrödinger equation for the radial wavefunction $u_l(r)$.

$$\left(\frac{1}{2}\frac{d^2}{dr^2} - \frac{l(l+1)}{2r^2} - V(\mathbf{r}) + \frac{k^2}{2}\right)\,u_l(r) = 0) \tag{4.8}$$

In this equation $l(l+1)/2r^2$ is the centrifugal potential barrier and the energy was written as $E = k^2/2$. It can be shown (see, e.g., [15]) that the scattering amplitude can then be written in terms of one set of parameters, the scattering phase shifts $\delta_l(k)$.

$$f(\theta,\phi) = \sum_{l=0}^{\infty}(2l+1)\,\frac{sin(\delta_l(k))}{k}\,P_l(cos\theta) \tag{4.9}$$

Since we are discussing spherically symmetric potentials, $V(r)$, the scattering amplitude does not depend on the azimuthal angle ϕ. The scattering phase shifts $\delta_l(k)$ are a measure of the asymptotic deviation of the wavefunction from the wavefunction without the external potential. The phase shifts depend on the scattering energy and on the structure of the scattering potential. As such these phase shifts are unique for each combination of different

scattering particles and as such experimental input of the real potentials and possible bound states is necessary in order to obtain the correct values of these phase shifts. For alkali atoms the scattering phase shifts were calculated by Fabrikant in a non-relativistic calculation [22], as well as a relativistic calculation [23]. For low-energy scattering only the first few terms of equation (4.9) contribute, as the phase shifts $\delta_l(k) \to 0$ for $l \to \infty$. This can be understood as the effect of the centrifugal barrier due to the angular momentum: If the scattering energy is lower than the centrifugal barrier, the higher angular momentum channels do not contribute to the scattering.
With expression (4.9) for the scattering amplitude, the total cross section from equation (4.6) can then be written as

$$\sigma_{\text{tot}} = 4\pi \sum_{l=0}^{\infty} (2l+1) \frac{sin^2(\delta_l(k))}{k^2} = \frac{4\pi}{k} \Im\left(f(\theta = 0, \phi)\right) \ . \tag{4.10}$$

The last equality is known as the optical theorem [24], which is a general law for wave scattering theory. The analysis presented here is a good procedure for low energies as the number of partial waves that have to be included is small. For higher scattering energies this analysis breaks down, as you have to include more and more partial waves. For the case studied in this thesis, and also for the early measurements done in a vapour cell, only the lowest partial waves have to be included, because the thermal velocity of the neutral atoms is really small compared to the velocity of the Rydberg electron. However, due to the small mass of the electron, the momentum and therefore the kinetic energy of the electron is really small. This means that for the Rydberg electron-neutral atom scattering studied in this thesis, only the s- and p-wave scattering ($l = 0$,1) has to be taken into account. Before focussing on this long-range scattering process, we will finish the discussion of short-range potentials.
It can be shown in the effective range theory that the scattering phase shifts obey the 'effective-range expansion' [25, 26]:

$$k^{2l+1} \cot\left(\delta_l(k)\right) = -\frac{1}{a_l} + \frac{1}{2} r_{\text{el}} k^2 + \mathcal{O}(k^4) \ . \tag{4.11}$$

In this expansion a_l is the scattering length for the corresponding angular momentum l and r_{el} is the effective range, which depends on the scattering potential $V(r)$. To understand how the scattering length is connected to the strength of the scattering potential, we will briefly discuss the square well potential (for a complete discussion see [15]). In figure 4.3 the connection between the s-wave scattering length a_0 and the potential depth of a square well potential with a unitary range is shown. There it can be seen, that the scattering length vanishes as the potential vanishes. For a repulsive potential, meaning positive potential strengths in the figure, the scattering length tends towards the range of the potential, which is marked by the dashed line in the figure. For attractive potentials the scattering length diverges for several potential strengths, each corresponding to an emergence of a new bound state (dotted lines) that is sustained in the potential.

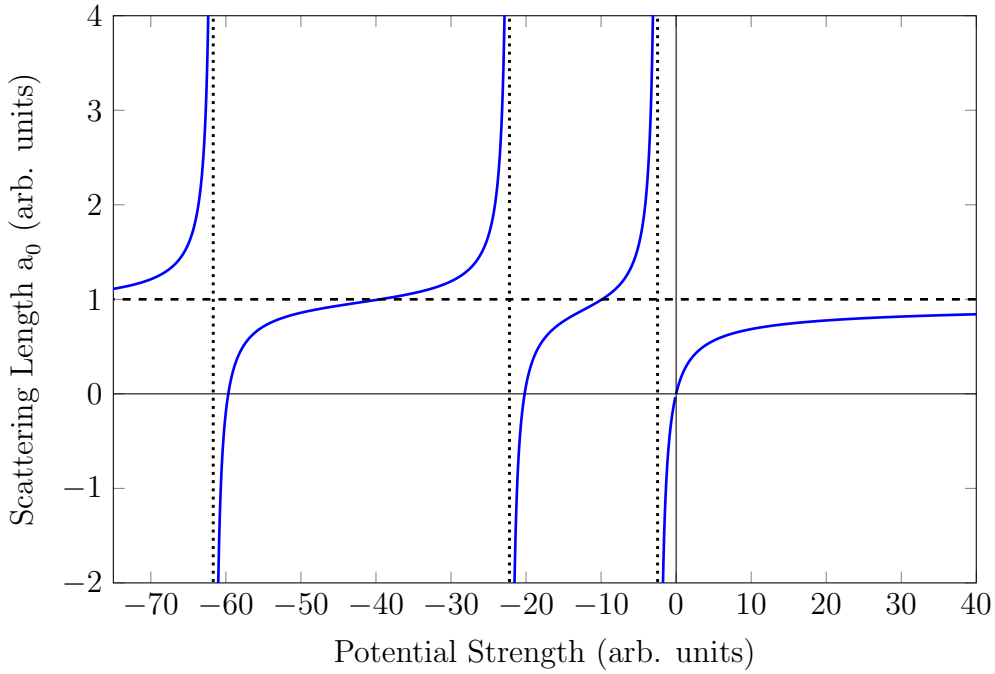

Figure 4.3.: Dependence of the s-wave scattering length on the potential strength for an exemplary square well potential with an unitary range. The scattering length tends towards the range of the potential (dashed line) for repulsive potentials and divergences for each occurrence of a new bound state (dotted lines), that is sustained in an attractive potential.

The s-wave scattering dominates the scattering process for low energies if there is no resonance for the higher partial waves. For Rubidium there is a p-wave shape resonance at about 20 meV, which means that the p-wave scattering has to be included if the scattering energy is in this range.
Now let us look at the situation that is of interest in the scope of this thesis, namely the scattering interaction of a Rydberg atom with an atom in the ground state. The Hamiltonian describing this interaction can be written as the sum of the three different contributions:

$$\hat{H} = \hat{H}_{\text{ion-e}^-} + \hat{H}_{\text{ion-atom}} + \hat{H}_{\text{atom-e}^-} \ . \tag{4.12}$$

The first term is the unperturbed Hamiltonian of the Rydberg state, with the known energy levels and wave functions of the electron. This describes the electronic states and as such the dissociation limit of the molecules bound by the scattering interaction. The second term represents the interaction of the ionic core and the ground state atom. This interaction only contributes at internuclear distances that are much smaller than the size of the Rydberg molecules discussed here and can as such be safely neglected. The last term describes the interaction of the Rydberg electron and the neutral ground state atom, which

is described by the polarization potential given in equation (4.13). This is a spherically symmetric potential that asymptotically only depends on the polarizibility α of the neutral ground state atom.

$$V(r) \underset{r\to\infty}{=} -\frac{\alpha}{2r^4} \tag{4.13}$$

Since the Rydberg electron is far away from the ionic core it can be considered as quasi-free, which means that the interaction can be treated as a scattering process with the polarization potential as the scattering potential. As already discussed above, this potential is a long-range potential and as such the discussion of the scattering process from above has to be adjusted because the effective range approach is not valid any more. It can be shown, e.g. [15], that the scattering length as defined by equation (4.11) is only valid if the exponent s of a r^{-s}-potential satisfies $s > 2l + 3$. Similarly the effective range r_{el} is not defined any more if $s \leq 2l + 5$. As such an effective range is not defined for s-wave scattering in the case of the polarization potential and a scattering length is only defined for s-wave scattering.
For the partial waves with $l \geq 1$ the Schrödinger equation (4.3) with the polarization potential can be solved by only looking at the asymptotic behaviour. Instead of the 'effective-range expansion' in equation (4.11), this leads to

$$k^2 \cot(\delta_l(k)) = \frac{8(l+3/2)\,(l+1/2)\,(l-1/2)}{\pi\alpha} + \mathcal{O}(k^2)\,. \tag{4.14}$$

As expected from the conditions discussed above, a scattering length is not defined for partial waves with $l \geq 1$. For s-wave scattering this asymptotic behaviour analysis can not be done. For this reason O'Malley et al.[16] introduced a modified effective range theory for the case of the polarization potential.

$$k \cot(\delta_0(k)) = -\frac{1}{a_0} + \frac{\pi\alpha}{3a_0^2}\,k + \frac{4\alpha}{3a_0}\,k^2\,\log\left(\frac{\sqrt{\alpha}\,k}{4}\right) + \mathcal{O}(k^2) \tag{4.15}$$

The obtained expressions can be connected to the total cross section in equation (4.10) by using $\sin(\delta_l)/k \simeq \tan(\delta_l)/k$. For this the expressions (4.14) and (4.15) have to be rewritten, as they can be found, e.g. in [27].

$$-\frac{\tan(\delta_l(k))}{k} = -\frac{\pi\alpha}{8(l+3/2)\,(l+1/2)\,(l-1/2)}\,k + \mathcal{O}(k^2) \tag{4.16}$$

$$-\frac{\tan(\delta_0(k))}{k} = a_0 + \frac{\pi\alpha}{3}\,k + \frac{4\alpha\,a_0}{3}\,k^2\,\log\left(\frac{\sqrt{\alpha}\,k}{4}\right) + \mathcal{O}(k^2) \tag{4.17}$$

The expansions (4.16) and (4.17) can be used as expressions for an energy dependent scattering length $a_0(k)$ and $a_l(k)$ for finite scattering energies. Substituting (4.17) into equation (4.10) for the total cross section we obtain the energy dependence of the s-wave cross section.

$$\sigma_{\text{tot, l=0}}(k) = 4\pi \cdot \left(a_0 + \frac{\pi\alpha}{3}\, k + \ldots\right)^2 \tag{4.18}$$

For the scattering of the Rydberg electron with a neutral ground state atom at the position $\mathbf{R}$, the influence of higher partial waves was first studied by Omont[19], who obtained the following pseudopotential

$$V\text{pseudo}(\mathbf{R}) = 2\pi \sum_{l=0}^{\infty} (2l+1)\, a_l(k) \left(P_l \left(\frac{\nabla_{\mathbf{r}'} \cdot \nabla_{\mathbf{r}}}{k^2} \right) \psi^*(\mathbf{r}')\psi(\mathbf{r}) \right)_{\mathbf{r}=\mathbf{r}'=\mathbf{R}} . \tag{4.19}$$

In this equation the wave number is given by $k(r) = \sqrt{2(E_{\text{nl}} + 1/r)}$ and the energy dependent scattering length by

$$a_l(k) = -\frac{\tan(\delta_l(k))}{k^{2l+1}} . \tag{4.20}$$

Using only the first term of the sum in equation (4.19) and only the zero-order contribution in k, results in the famous Fermi-pseudopotential already given in equation (4.1). Only taking into account the p-wave contribution ($l = 1$) of the sum in equation (4.19) results in

$$V_{\text{l=1}}(\mathbf{R}) = \frac{6\pi}{k^2}\, a_1(k)\, |\nabla_{\mathbf{R}}\, \psi(\mathbf{R})|^2 . \tag{4.21}$$

All higher partial waves can be safely neglected for the range of the scattering energy leading to the Rydberg molecules. As can be seen from Greene's formalism in equation (4.2) the molecular potential shows the same oscillatory behaviour in an s-wave scattering treatment as the electron wave function of the Rydberg state.
Quantum mechanically there is another degree of freedom that influences the scattering process: the relative spin orientation of the two scattering particles. For the nS Rydberg states as well as the ground state of ^{87}Rb, that are considered in the scope of this thesis, there is one valence electron which has a spin of $S = 1/2$. The combination of the two spins can form a symmetric (triplet) or an antisymmetric (singlet) spin-wavefunction. The influence of these spin configurations on the scattering process can be taken into account by introducing different scattering lengths for the two cases, or by including the spin from the very beginning by solving the time-independent Dirac equation 4.22[54] instead of the Schrödinger equation (4.3).

$$\left(c\,\boldsymbol{\alpha} \cdot \mathbf{p} + \beta' c^2 + V(\mathbf{r})\right)\, \psi(\mathbf{x}) = E\, \psi(\mathbf{x}) \tag{4.22}$$

Here $\mathbf{x} = (\mathbf{r},\sigma)$ includes the space ($\mathbf{r}$) and spin (σ) coordinates, c is the speed of light, $\beta' = \beta - \mathbb{1}_4$ is chosen such that the rest mass of the electron is not included in the equation and the entries of the vector $\boldsymbol{\alpha}$ and β are the 4×4 Dirac matrices defined by

$$\alpha_{\text{x,y,z}} = \begin{pmatrix} 0 & \sigma_{\text{x,y,z}} \\ \sigma_{\text{x,y,z}} & 0 \end{pmatrix} \qquad \text{and} \qquad \beta = \begin{pmatrix} \mathbb{1}_2 & 0 \\ 0 & -\mathbb{1}_2 \end{pmatrix} . \tag{4.23}$$

Thereby $\sigma_{x,y,z}$ are the Pauli spin matrices [55]. Solving the scattering problem with the Dirac equation leads to a dependency of the scattering phase shifts $\delta_l(k)$ on the spin configuration of the particles (for further information see pages 45-55 in [15]). Due to the spin-orbit coupling it is also possible for a spin-flip to occur during the scattering process, which can also be described by this formalism.
As already mentioned above, the combination of two spin 1/2 particles can lead to either a triplet or a singlet configuration of the spins. There are three possible symmetric combinations of the two spins

$$|\uparrow\uparrow\rangle\,,\ |\downarrow\downarrow\rangle\ \text{and}\ \frac{1}{\sqrt{2}}\left(|\uparrow\downarrow\rangle + |\downarrow\uparrow\rangle\right)\,, \tag{4.24}$$

leading to a triplet configuration and one anti-symmetric singlet combination

$$\frac{1}{\sqrt{2}}\left(|\uparrow\downarrow\rangle - |\downarrow\uparrow\rangle\right)\,. \tag{4.25}$$

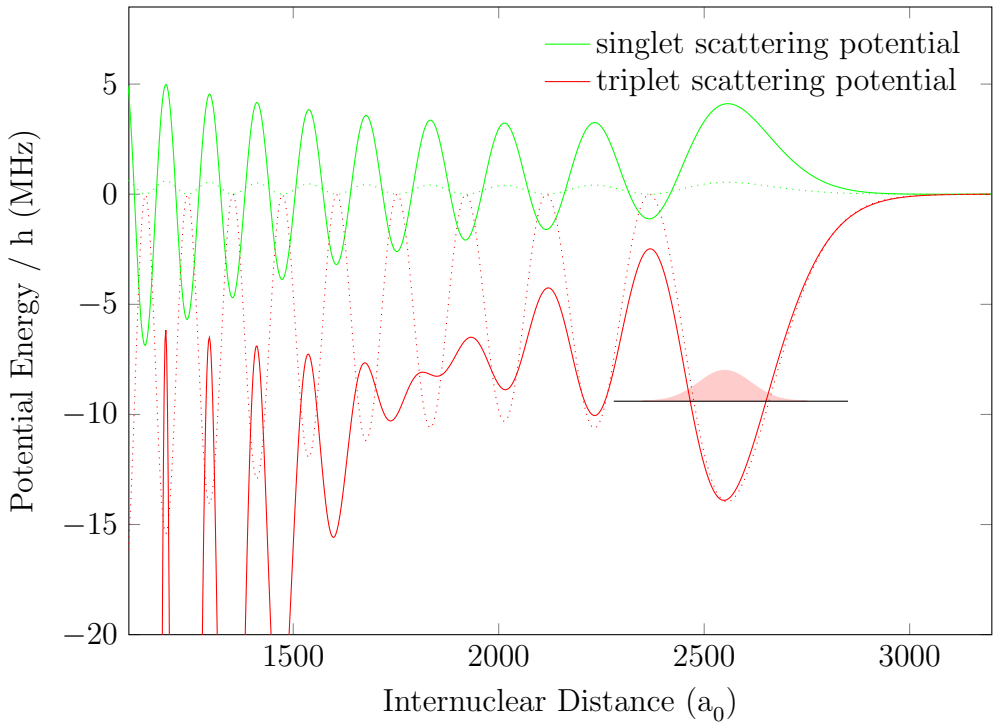

Figure 4.4.: Scattering potential for pure singlet and triplet scattering of an atom in a 40S Rydberg state and an atom in the 5S ground state of ^{87}Rb calculated from the zero-energy Fermi-pseudopotential given by equation (4.1) (dotted lines) and from a full diagonalization method including the neighbouring Rydberg states, the energy dependence of the scattering and the p-wave scattering contribution (solid lines). In the attractive potential arising from the triplet scattering an exemplary wavefunction of a bound molecular states is shown.

Theoretical calculations of the zero-energy s-wave scattering length lead to predictions of $a_{0,\mathrm{T}} = -16.1\,a_0$ [23] for the triplet scattering length and $a_{0,\mathrm{S}} = +0.63\,a_0$ [23] for the singlet scattering length. Looking at the Fermi-pseudopotential in equation (4.1) this leads to an attractive potential for the case of triplet scattering and a repulsive potential for singlet scattering. These potentials are shown schematically for the 40S Rydberg state in figure 4.4. The dotted lines in the figure are the potentials calculated with the Fermi-pseudopotential using only the zero-energy scattering lengths. The solid lines are the potentials obtained from diagonalizing the scattering Hamiltonian [42] using the scattering phase shifts from [22], including all Rydberg states in the range of $\Delta n = \pm 15$. It can be seen in figure 4.4 that the neighbouring Rydberg states, the p-wave scattering and the k-dependence of the scattering strongly influence the potentials. The triplet scattering potential bends down for the small internuclear distances shown, due to the shape resonance of the triplet p-wave scattering, which does not exist for singlet p-wave scattering. In these pure singlet and triplet potentials bound molecular states are only possible in the attractive potential arising from the triplet scattering,as shown schematically by the calculated wavefunction of the molecular ground state. The binding energies and the respective wavefunctions are calculated by solving the Schrödinger equation using Numerov's method [59, 60].
Only recently it was shown that the hyperfine structure of the ground state atom mixes singlet and triplet scattering channels, leading to mixed singlet-triplet potentials that are able to sustain bound molecular states. These mixed singlet-triplet molecules will be considered in detail later on.

4.2. Triplet spectroscopy: Work up to now

Since the prediction of ultralong-range Rydberg molecules in 2000 by Greene et al. [28], these molecules have gained a lot of experimental and theoretical attention, because they represent a new mechanism of chemical bonding and because of their surprising properties, like e.g. a permanent electric dipole moment in a homonuclear molecule. The Rydberg molecules were for the first time spectroscopically observed by Bendkowsky et al.[29] for ^{87}Rb atoms in the range of $n = 35 - 37$. In this work the diatomic ground state as well as several excited vibrational states were observed. Later on also more atomic states [30, 35], like trimer states consisting of one Rydberg atom and two ground state atoms, and excited states bound by quantum reflection [30] were observed. The molecules with multiple ground state atoms bound to the Rydberg atom by the electron-neutral scattering are possible because the neutral-neutral scattering length and as such the range of the neutral-neutral scattering interaction, is significantly smaller than the mean interparticle distance in the atomic cloud. Because of this, different ground state atoms inside the same Rydberg wavefunction do not interact with each other, leading to molecular states containing more than one ground state atom. Because the different ground state atoms do not interact with each other the binding energy is additive, meaning that the triatomic molecule has twice the binding energy of the diatomic molecule and so on [35].
In figure 4.5 a spectrum of the 40S Rydberg state, measured in a thermal cloud with a

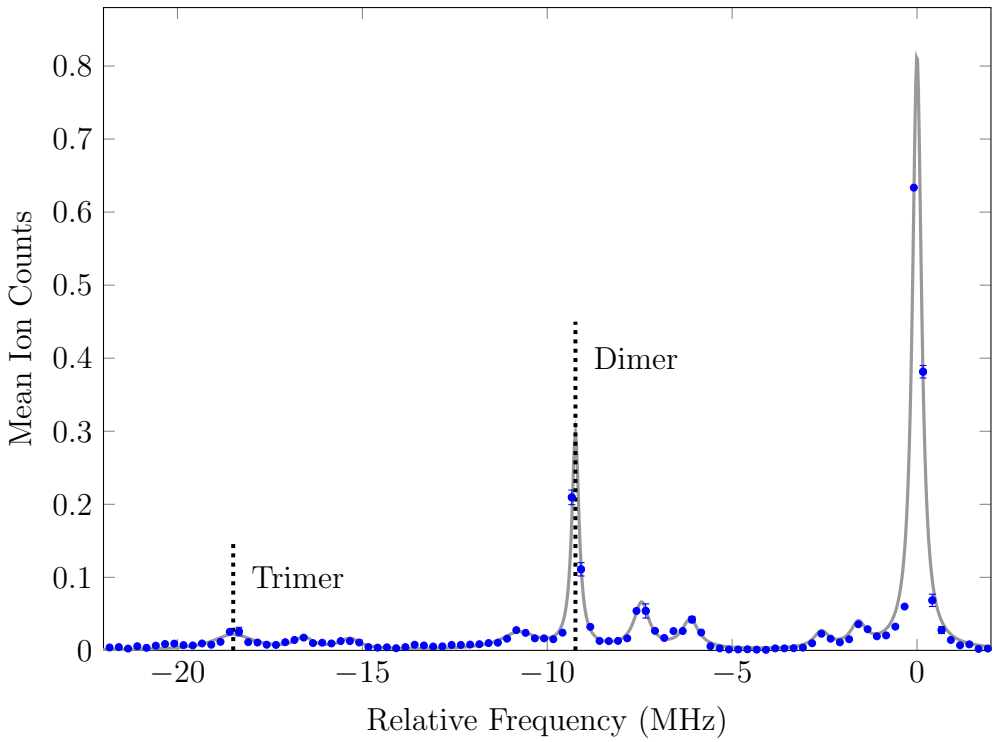

Figure 4.5.: Molecular spectrum of the 40S Rydberg state measured in a thermal cloud. The atomic transition from the 5S, F=2, m_F=2 to the 40S, m_S=1/2 state corresponds to the zero of the frequency axis. This corresponds to the dissociation limit of the molecular states and as such the relative frequencies in the figure correspond to the binding energies of the molecular states. On the left side of the atomic transition the dimer state is visible at -9.3 MHz and the trimer state at -18.6 MHz. Several excited states of both the dimer and the trimer states are also visible as smaller peaks. The standard error of the measured mean ion counts are shown exemplary for some of the data points. The grey line is a multiple-Lorentzian fit to the data, shown for better visibility.

temperature of about 1 µK, is shown. There the diatomic molecular ground state is visible as a peak at -9.3 MHz, with several excited states visible in between this state and the peak of the atomic transition at zero, which corresponds to the dissociation limit of the 40S-5S Rydberg molecules. In the spectrum the trimer state is also visible at -18.6 MHz, corresponding to twice the binding energy of the dimer state.

The ground state of the diatomic Rydberg molecule is bound in the outermost well of the triplet scattering potential shown in figure 4.4. As the depth of this potential well changes with the principal quantum number n^*, so does the binding energy of the molecular states. Because of the scaling of the classical electron orbit as n^{*2}, the volume of the electron wavefunction scales as n^{*6}. Since the wavefunction has to be normalized, the amplitude of the wavefunction has to decrease accordingly if the volume increases. From this size

argument of the Rydberg wavefunction one would expect that the depth of the scattering potential scales as n^{*-6} with the principal quantum number. Experimentally an exponent of -6.26 ± 0.12 was found by Gaj et al.[35], matching the predicted value quite well.
Since the initial experimental observation of Rydberg molecules, a lot of phenomena have been explored, such as the coherent creation and breaking of the molecular bond [31] and exotic trilobite states [33, 37]. Also the lifetimes of the molecular ground and excited states [32] were studied, where it was found, that the decay rate of the molecular states depends on the lifetime of the Rydberg state as well as on collisions with the background gas, which lead to the dissociation of the molecule. The collisional lifetime is of course dependent on the density of the atomic cloud and the thermal energy of the atoms. The p-wave shape resonance in the electron-Rubidium scattering potential leads to shorter lifetimes of the molecular states than it is the case for systems which do not show such a shape resonance, e.g. strontium [64]. In systems with no p-wave scattering resonance the lifetime of the molecules is only limited by the lifetime of the Rydberg state, if the density and therefore the collisional decay rate is small enough.
Diatomic Rydberg molecules were also realized for S-states in Cs [38] and Sr [41, 64], for P-states in Rb [40] and Cs [3] and for D-states in Rb [34, 36, 39]. For the D-state molecules it was shown that it is possible to control the hybridization of the molecular orbitals by tuning the strength of an external electric field [36]. Rydberg molecules in Rb have also been used as a probe of the phase transition from a Mott-insulator to a superfluid phase in an optical lattice [43].
With Rydberg molecules it is also possible to study the transition from a two-body to a many-body system by simply increasing the principal quantum number n and with that the number of atoms inside the electron wave function [35]. By doing this, one can see the transition from distinguishable molecular lines to an inhomogeneously broadened spectral line, which can be described by a mean-field model. In this mean-field model, taking only s-wave scattering into account, the shift of the spectral line is given by

$$\Delta E = \int d\mathbf{R}\, V(\mathbf{R}) \cdot \varrho(\mathbf{R}) = 2\pi\, a_0\, \bar{\varrho}\,. \tag{4.26}$$

In this equation $\varrho(\mathbf{R})$ is the density distribution and $\bar{\varrho}$ the mean density of the atomic cloud. The same transition can be observed by increasing the density instead of the principal quantum number. This was done by exciting single Rydberg atoms inside a BEC and showing that the center of gravity of the obtained spectra is more or less independent of the quantum number [5]. For the higher densities of a BEC, the inter-particle distance decreases and the p-wave shape resonance plays an important role for the broadening of the observed spectra [4]. This is because even a single particle close to the p-wave shape resonance contributes a lot to the overall shift of the spectral line. A 40S Rydberg spectrum measured inside a BEC is shown in figure 4.6. In this figure one can see a broad spectral line coming from the Rydberg atoms excited inside the high density fraction and distinguishable molecular peaks from the thermal fraction. The model used to simulate the spectra (red line) is discussed in detail in [4].
The shift of the spectral line in the BEC spectrum can be used to study density dependent

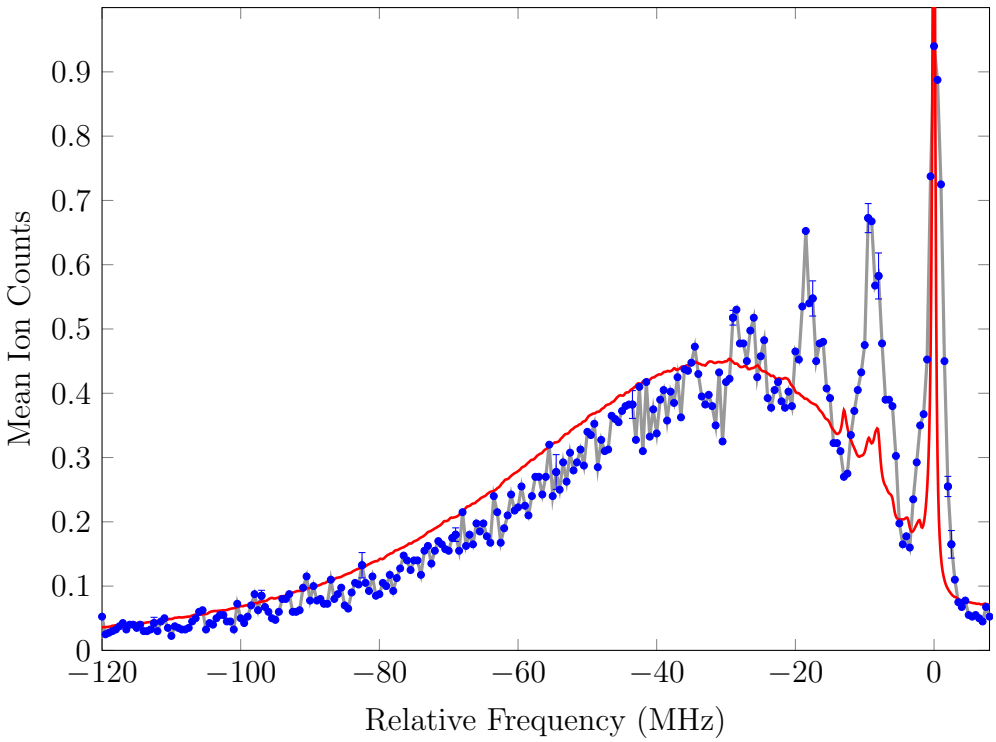

Figure 4.6.: Spectrum of the 40S Rydberg state measured in a BEC with a peak density of about $5.5 \cdot 10^{14}\,\mathrm{cm}^{-3}$. The spectrum consists of a broad line coming from Rydberg atoms excited in the high density region and the atomic and molecular lines coming from the thermal fraction of the atomic cloud. The red line is a simulated spectrum taking into account the bimodal density distribution and the full scattering potential, which includes the p-wave shape resonance [4]. The atomic transition once again corresponds to the zero of the frequency axis. For some data points the standard error of the mean ion counts is shown exemplary in the spectrum. The grey line acts as a guide to the eye that connects the data points.

phenomena inside the BEC, as each detuning from the atomic resonance corresponds to a number of configurations of atoms, which sum up to give exactly this shift of the spectral line. These configurations of atoms can be seen as different local densities inside the cloud. As such there is a correspondence between the detuning from the atomic resonance and the local density. This can be used to study the density distribution of the BEC with the Rydberg atom acting as a local probe [6]. Also the dynamics of the Rydberg atom inside the atomic cloud can be studied for different detunings from the atomic resonance and as such different density distributions. There it can be observed that the Rydberg atoms inside the BEC undergo l-changing collisions on a time scale that depends on the principal quantum number, ranging from 1 µs for 53S up to about 10 µs for 149S [7].

Also the interaction of the Rydberg electron with the BEC has been studied [44] showing

that it is possible to set the whole condensate into a collective oscillation by exciting a single Rydberg atom. Furthermore it should be possible to imprint the scattering potential, and as such more or less the electron wavefunction, onto the density distribution of the condensate [45, 46]. This imprint of the scattering potential on the density distribution should occur after the Rydberg excitation because the particles want to minimize their energy and as such they want to 'flow' into the potential wells of the scattering potential. This increase of particles in the potential wells of the scattering potential should then be visible in the density distribution of the BEC, which can directly be imaged after a few microseconds following the Rydberg excitation using in-situ phase contrast imaging.
All the work presented in this section has been done by taking only triplet scattering into account, which is correct if the Rydberg atoms are excited using the excitation scheme shown in figure 3.5. By using an unpolarized atomic sample or by changing the scheme of the Rydberg excitation by using different polarizations of the laser beams, leading to a spin-flip during the excitation, it is possible for the singlet scattering channel to play a role as well. As seen in the previous section, the pure singlet scattering leads to a repulsive potential and as such no molecular states. Since the atoms can never be prepared in a pure singlet state in the experiment described in this thesis, and due to the hyperfine coupling in the ground state of the atoms, the singlet and triplet scattering channels mix, leading to mixed singlet-triplet molecular potentials able to sustain bound states. The theory of these mixed singlet-triplet Rydberg molecules will be discussed in the following section.

4.3. Theory of mixed singlet-triplet Rydberg molecules

Looking at the pure singlet and triplet scattering potentials in figure 4.4, it can be seen that no bound molecular states are possible for singlet scattering. However it was pointed out by Anderson et al.[2] that the hyperfine coupling in the ground state of the neutral atom leads to mixing of some triplet scattering channels with the singlet channels. This mixing leads to mixed singlet-triplet potentials, which Anderson et al. called 'shallow' potentials, that are able to sustain bound molecular states. These mixed singlet-triplet molecular states were first observed by Saßmannshausen et al.[3] for nP states in Cs in the range of $n = 26 - 34$. In the course of this thesis the naming convention of triplet and mixed potentials will be used, instead of deep and shallow potential as it was used by Anderson et al.[2].
The Hamiltonian of the system, including the hyperfine coupling in the 5S ground state of the neutral atom is given by

$$\begin{aligned}\hat{H}(\mathbf{r}, R) = \hat{H}_0 + A_{\mathrm{HF}}\, \hat{\mathbf{S}}_{\mathrm{g}} \otimes \hat{\mathbf{I}}_{\mathrm{g}} + \sum_{\mathrm{i=S,T}} 2\pi\, a^i_{l=0}(k)\, \delta^{(3)}(\mathbf{r} - R\hat{\mathbf{z}})\, \hat{P}_i \\ + \sum_{\mathrm{i=S,T}} 6\pi\, a^i_{l=1}(k)\, \delta^{(3)}(\mathbf{r} - R\hat{\mathbf{z}})\, \nabla \cdot \nabla\, \hat{P}_i\,.\end{aligned} \tag{4.27}$$

In this equation $\hat{H}_0$ is the Hamiltonian of the unperturbed Rydberg state, $\mathbf{r}$ is the position

of the Rydberg electron, R is the distance between the ionic core of the Rydberg atom and the neutral atom along the $\hat{\mathbf{z}}$-axis, $A_{\mathrm{HF}} = h/2 \cdot 6.835\,\mathrm{GHz}$ is the hyperfine constant of the 5S ground state, $\hat{\mathbf{S}}_{\mathrm{g}}$ is the operator of the electron spin and $\hat{\mathbf{I}}_{\mathrm{g}}$ the operator of the nuclear spin of the ground state. The third term is the s-wave scattering term with the sum covering both singlet (S) and triplet (T) scattering and the last term the p-wave scattering interaction. There $a_l(k)$ is the energy dependent scattering length for the first two partial waves, the s-wave ($l = 0$) and the p-wave ($l = 1$), as it was introduced by equation 4.20. In the two scattering terms, $\hat{P}_{\mathrm{T}}$ and $\hat{P}_{\mathrm{S}}$ are the projection operators defined by

$$\hat{P}_{\mathrm{T}} = \hat{\mathbf{S}}_{\mathrm{r}} \otimes \hat{\mathbf{S}}_{\mathrm{g}} + \frac{3}{4}\,\mathbb{1} \quad \text{and} \quad \hat{P}_{\mathrm{S}} = \mathbb{1} - \hat{P}_{\mathrm{T}}\,. \tag{4.28}$$

The molecular potential energy curves are then obtained by diagonalizing the Hamiltonian (4.27) as a function of the internuclear distance R.
The Hamiltonian given by 4.27 conserves the total quantum number $M = m_{\mathrm{I,g}} + m_{\mathrm{S,g}} + m_{\mathrm{S,r}}$. As such the matrix given by equation 4.35 can also be written as a block diagonal matrix, by re-arranging the basis vectors. The Hilbert space as such can then be seen as a combination of sub-spaces with a fixed quantum number M.
To better understand the underlying physics, we will look at the matrix representation of the Hamiltonian. For this all the parts building up the Hamiltonian (4.27) will be explained separately before combining them to the Hamiltonian.
Considering a system of two spin 1/2 particles, the Hilbert space used to describe the system is 4-dimensional. In this Hilbert space the two spins can either be in a triplet configuration, which is symmetric with respect to a permutation of the two spins, or in an anti-symmetric singlet configuration. These singlet and triplet states are then the eigenstates of the system. In the basis of two independent spins the three triplet states are given by

$$\begin{aligned} |\uparrow\uparrow\rangle &= (1,0,0,0) \\ |\downarrow\downarrow\rangle &= (0,0,0,1) \\ \frac{1}{\sqrt{2}}\,(|\uparrow\downarrow\rangle + |\downarrow\uparrow\rangle) &= \frac{1}{\sqrt{2}}\,(0,1,1,0) \end{aligned} \tag{4.29}$$

and the singlet state by

$$\frac{1}{\sqrt{2}}\,(|\uparrow\downarrow\rangle - |\downarrow\uparrow\rangle) = \frac{1}{\sqrt{2}}\,(0,1,-1,0)\,. \tag{4.30}$$

In order to get the projection operators, one has to calculate the tensor product of the two spin operators $\hat{\mathbf{S}}_1 \otimes \hat{\mathbf{S}}_2$. The spin operator of the spin 1/2 system is defined by the Pauli spin matrices $\hat{\mathbf{S}} = 1/2\,(\sigma_{\mathrm{x}},\sigma_{\mathrm{y}},\sigma_{\mathrm{z}})$. With this the projection operator for the triplet and singlet states are then given by

$$\hat{P}_{\mathrm{T}} = \begin{pmatrix} 1 & 0 & 0 & 0 \\ 0 & 1/2 & 1/2 & 0 \\ 0 & 1/2 & 1/2 & 0 \\ 0 & 0 & 0 & 1 \end{pmatrix} \quad \text{and} \quad \hat{P}_{\mathrm{S}} = \begin{pmatrix} 0 & 0 & 0 & 0 \\ 0 & 1/2 & -1/2 & 0 \\ 0 & -1/2 & 1/2 & 0 \\ 0 & 0 & 0 & 0 \end{pmatrix} . \tag{4.31}$$

As a next step we have to get the matrix representation of the hyperfine Hamiltonian in the uncoupled $|L, S, I\rangle$-basis. For the 5S ground state of ^{87}Rb, the quantum numbers take the values of $L = 0$, $S = 1/2$ and $I = 3/2$. The Hilbert space of this system then has a dimension of $(2S+1)(2I+1) = 8$. For the electron with spin 1/2, the spin-operator is again given by the Pauli matrices $\hat{\mathbf{S}} = 1/2\,(\sigma_{\mathrm{x}},\sigma_{\mathrm{y}},\sigma_{\mathrm{z}})$. The matrix representation for the nuclear spin of $I = 3/2$ is given by $\hat{\mathbf{I}} = (\hat{I}_{\mathrm{x}},\hat{I}_{\mathrm{y}},\hat{I}_{\mathrm{z}})$, with the following three spin operators[56].

$$\begin{aligned} \hat{I}_{\mathrm{x}} &= \frac{1}{2} \begin{pmatrix} 0 & \sqrt{3} & 0 & 0 \\ \sqrt{3} & 0 & 2 & 0 \\ 0 & 2 & 0 & \sqrt{3} \\ 0 & 0 & \sqrt{3} & 0 \end{pmatrix} \\ \hat{I}_{\mathrm{y}} &= \frac{i}{2} \begin{pmatrix} 0 & -\sqrt{3} & 0 & 0 \\ \sqrt{3} & 0 & -2 & 0 \\ 0 & 2 & 0 & -\sqrt{3} \\ 0 & 0 & \sqrt{3} & 0 \end{pmatrix} \\ \hat{I}_{\mathrm{x}} &= \frac{1}{2} \begin{pmatrix} 3 & 0 & 0 & 0 \\ 0 & 1 & 0 & 0 \\ 0 & 0 & -1 & 0 \\ 0 & 0 & 0 & -3 \end{pmatrix} \end{aligned} \tag{4.32}$$

With this the matrix representation of the hyperfine Hamiltonian for the 5S ground state of ^{87}Rb can be calculated.

$$\begin{aligned} \hat{H}_{\mathrm{HF}} &= A_{\mathrm{HF}}\, \hat{\mathbf{S}}_{\mathrm{g}} \otimes \hat{\mathbf{I}}_{\mathrm{g}} = A_{\mathrm{HF}}\, (\hat{S}_{\mathrm{x}} \otimes \hat{I}_{\mathrm{x}} + \hat{S}_{\mathrm{y}} \otimes \hat{I}_{\mathrm{y}} + \hat{S}_{\mathrm{z}} \otimes \hat{I}_{\mathrm{z}}) \\ &= A_{\mathrm{HF}} \cdot \begin{pmatrix} 3/4 & 0 & 0 & 0 & 0 & 0 & 0 & 0 \\ 0 & 1/4 & 0 & 0 & \sqrt{3}/2 & 0 & 0 & 0 \\ 0 & 0 & -1/4 & 0 & 0 & 1 & 0 & 0 \\ 0 & 0 & 0 & -3/4 & 0 & 0 & \sqrt{3}/2 & 0 \\ 0 & \sqrt{3}/2 & 0 & 0 & -3/4 & 0 & 0 & 0 \\ 0 & 0 & 1 & 0 & 0 & -1/4 & 0 & 0 \\ 0 & 0 & 0 & \sqrt{3}/2 & 0 & 0 & 1/4 & 0 \\ 0 & 0 & 0 & 0 & 0 & 0 & 0 & 3/4 \end{pmatrix} \end{aligned} \tag{4.33}$$

This matrix has two different eigenvalues: $3/4\,A_{\mathrm{HF}}$ and $-5/4\,A_{\mathrm{HF}}$, corresponding to the $F = 2$ and $F = 1$ hyperfine states respectively. Thereby the eigenvalue for the $F = 2$ state is five times degenerate and the eigenvalue for $F = 1$ three times degenerate.
Together with the expressions for the pure singlet (S) and triplet (T) scattering interaction obtained from the scattering theory we have all the parts needed to build up the matrix representation of the Hamiltonian in equation (4.27). The pure scattering potentials will be treated as known functions $V_{\mathrm{S,T}}(R)$ of the internuclear distance R and are as such simple numbers for a fixed value of R. In order to get the Hamiltonian, the matrices of the hyperfine Hamiltonian in equation (4.33) and the triplet and singlet projection operators in (4.31) have to be adjusted to the system of interest to us: the Rydberg electron with two possible states $m_{\mathrm{S}} = \pm 1/2$, interacting with the electron of the 5S ground state atom, which has 8 states due to its coupling to the nuclear spin. This is a simplification of the real process, in order to work with the lowest number of states as possible to reduce the computational complexity. The spacing between neighbouring Rydberg states is on the same order of magnitude as the hyperfine splitting of the ground state and in the full diagonalization method used to calculate the pure singlet and triplet scattering potentials these neighbouring states were included, as they have an influence on the scattering potentials. However including all necessary states in the calculation would lead to huge matrices and in order to reduce the computational complexity, this two-step approach was used. The Hilbert space of this system is 16-dimensional and in order to get the matrix representation of the full Hamiltonian one has to take the tensor product of the respective operators with the identity operator $\mathbb{1}$.

$$\hat{H}(R) = \mathbb{1}_2 \otimes \hat{H}_{\mathrm{HF}} + V_{\mathrm{S}}(R) \cdot (\hat{P}_{\mathrm{S}} \otimes \mathbb{1}_4) + V_{\mathrm{T}}(R) \cdot (\hat{P}_{\mathrm{T}} \otimes \mathbb{1}_4) \tag{4.34}$$

This equation now includes the scattering interaction of the two valence electrons of the two possible Rydberg states and the hyperfine states of an atom in the 5S ground state. The 16×16 matrix representing the Hamiltonian of this system is then given by equation (4.35). In this matrix the index of the hyperfine constant A_{HF} and the dependency of the scattering potentials on the internuclear separation R, are omitted for simplicity.

$$\hat{H} = \begin{pmatrix}
\frac{3A}{4}+V_T & 0 & 0 & 0 & 0 & 0 & 0 & 0 & 0 & 0 & 0 & 0 & 0 & 0 & 0 & 0 \\
0 & \frac{A}{4}+V_T & 0 & 0 & 0 & 0 & 0 & 0 & 0 & 0 & 0 & 0 & 0 & 0 & 0 & 0 \\
0 & 0 & \frac{-A}{4}+V_T & 0 & 0 & A & 0 & 0 & 0 & 0 & 0 & 0 & 0 & 0 & 0 & 0 \\
0 & 0 & 0 & \frac{-3A}{4}+V_T & 0 & 0 & \frac{\sqrt{3}A}{2} & 0 & 0 & 0 & 0 & 0 & 0 & 0 & 0 & 0 \\
0 & \frac{\sqrt{3}A}{2} & 0 & 0 & \frac{-3A}{4}+\frac{V_T+V_S}{2} & 0 & 0 & \frac{V_T-V_S}{2} & 0 & 0 & 0 & 0 & 0 & 0 & 0 & 0 \\
0 & 0 & A & 0 & 0 & \frac{-A}{4}+\frac{V_T+V_S}{2} & 0 & 0 & \frac{V_T-V_S}{2} & 0 & 0 & 0 & 0 & 0 & 0 & 0 \\
0 & 0 & 0 & \frac{\sqrt{3}A}{2} & 0 & 0 & \frac{A}{4}+\frac{V_T+V_S}{2} & 0 & 0 & \frac{V_T-V_S}{2} & 0 & 0 & 0 & 0 & 0 & 0 \\
0 & 0 & 0 & 0 & \frac{V_T-V_S}{2} & 0 & 0 & \frac{3A}{4}+\frac{V_T+V_S}{2} & 0 & 0 & \frac{\sqrt{3}A}{2} & 0 & 0 & 0 & 0 & 0 \\
0 & 0 & 0 & 0 & 0 & \frac{V_T-V_S}{2} & 0 & 0 & \frac{A}{4}+\frac{V_T+V_S}{2} & 0 & 0 & A & 0 & 0 & 0 & 0 \\
0 & 0 & 0 & 0 & 0 & 0 & \frac{V_T-V_S}{2} & 0 & 0 & \frac{-A}{4}+\frac{V_T+V_S}{2} & 0 & 0 & \frac{\sqrt{3}A}{2} & 0 & 0 & 0 \\
0 & 0 & 0 & 0 & 0 & 0 & 0 & \frac{\sqrt{3}A}{2} & 0 & 0 & \frac{-3A}{4}+V_T & 0 & 0 & 0 & 0 & 0 \\
0 & 0 & 0 & 0 & 0 & 0 & 0 & 0 & \frac{\sqrt{3}A}{2} & 0 & 0 & \frac{-A}{4}+V_T & 0 & 0 & 0 & 0 \\
0 & 0 & 0 & 0 & 0 & 0 & 0 & 0 & 0 & \frac{\sqrt{3}A}{2} & 0 & 0 & \frac{A}{4}+V_T & 0 & 0 & 0 \\
0 & 0 & 0 & 0 & 0 & 0 & 0 & 0 & 0 & 0 & 0 & 0 & 0 & \frac{3A}{4}+V_T & 0 & 0 \\
0 & 0 & 0 & 0 & 0 & 0 & 0 & 0 & 0 & 0 & 0 & 0 & 0 & 0 & \frac{3A}{4}+V_T & 0 \\
0 & 0 & 0 & 0 & 0 & 0 & 0 & 0 & 0 & 0 & 0 & 0 & 0 & 0 & 0 & \frac{3A}{4}+V_T
\end{pmatrix} \tag{4.35}$$

Diagonalizing this matrix as a function of the internuclear distance R results in the molecular potential energy curves. The matrix representation of the Hamiltonian results in 4 different eigenvalues, which are given in equations (4.36)-(4.38). In the equations for the eigenvalues, the R-dependency of the scattering potentials $V_{\mathrm{S,T}}$ was again omitted for simplicity.

$$\frac{3}{4} A_{\mathrm{HF}} + V_{\mathrm{T}} \quad 6 \times \text{degenerate} \tag{4.36}$$

$$-\frac{5}{4} A_{\mathrm{HF}} + V_{\mathrm{T}} \quad 2 \times \text{degenerate} \tag{4.37}$$

$$-\frac{1}{4} A_{\mathrm{HF}} + \frac{1}{2} \left(V_{\mathrm{T}} + V_{\mathrm{S}} \pm \sqrt{4\, A_{\mathrm{HF}}^2 + A_{\mathrm{HF}} \cdot V_{\mathrm{S}} + V_{\mathrm{S}}^2 - A_{\mathrm{HF}} \cdot V_{\mathrm{T}} - 2\, V_{\mathrm{S}} \cdot V_{\mathrm{T}} + V_{\mathrm{T}}^2} \right) \quad \text{each } 4 \times \text{degenerate} \tag{4.38}$$

For the obtained eigenvalues, 8 eigenvalues contain only the triplet scattering interaction (given by equation (4.36) and (4.37)), while the other 8 contain both singlet and triplet scattering (given by equation (4.38)). The 8 eigenvalues that contain both singlet and triplet scattering, form the mixed molecular potentials as they were pointed out by Anderson et al.[2]. Without the scattering interaction, the eigenvalues are split apart to form the hyperfine $F = 2$ and $F = 1$ states with their respective degeneracy. With the scattering interaction there are 6 molecular potentials formed by pure triplet scattering for $F = 2$ and only 2 for $F = 1$, while there are 4 mixed singlet-triplet potentials for both hyperfine levels.
The obtained molecular potentials are shown in figure 4.7 as a function of the internuclear separation R for the 40S Rydberg state. In this figure the pure triplet potentials are shown in red, while the mixed potentials are shown in green. The pure singlet and triplet potentials used in the calculation of these potentials are again calculated with the full diagonalization method already shown in figure 4.4. In the figure it is clearly visible that the mixed potentials for $F = 1$ are deeper than the ones for $F = 2$. This was already pointed out by Anderson et al.[2] in their initial paper about mixed molecules and then also experimentally observed by Saßmannshausen et al.[3].
In order to explain the measurements done in the described experiment, it is necessary to include the interaction with an external magnetic field, since the experiment is done in a magnetic trap with a non-zero offset. The interaction of the electronic sub-states of an atom with an external magnetic field is described by the Hamiltonian in equation (2.11). This interaction was already described in detail in chapter 2.3.

$$\hat{H}(R) = \hat{H}_{\mathrm{B}} + \hat{H}_{\mathrm{HF}} + V_{\mathrm{S}}(R) \cdot \hat{P}_{\mathrm{S}} + V_{\mathrm{T}}(R) \cdot \hat{P}_{\mathrm{T}} \tag{4.39}$$

The Hamiltonian of the interaction of the electron spin with the magnetic field $\hat{H}_{\mathrm{B}}$ has to be included in the Hamiltonian given by equation 4.27. This interaction only appears if both spins are pointing in the same direction, because the Zeeman shift of each spin cancels

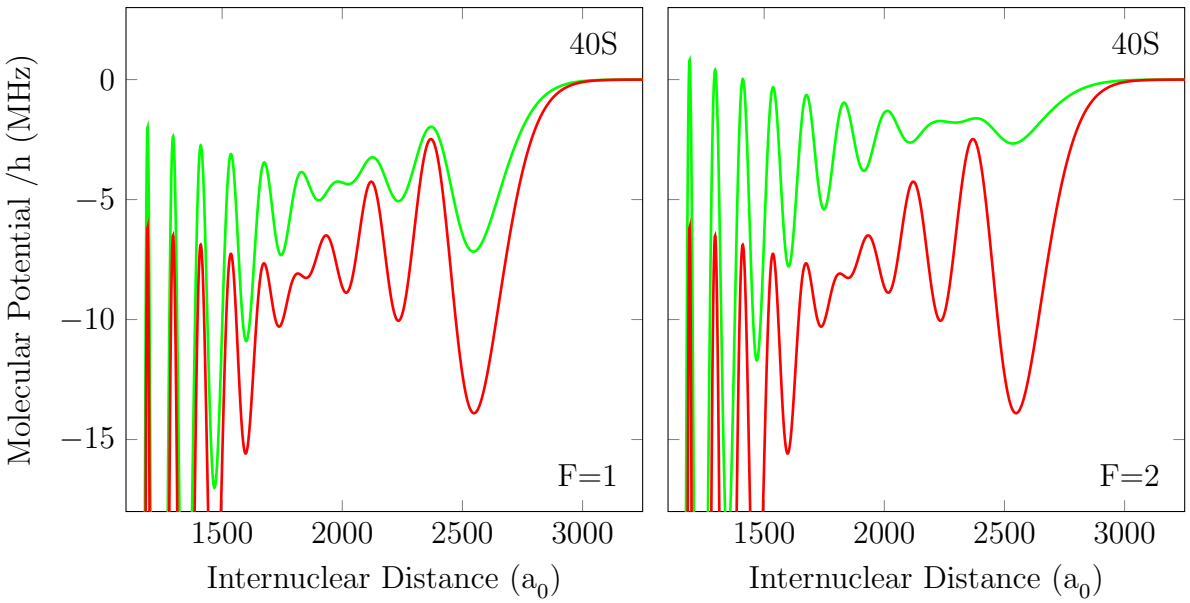

Figure 4.7.: Potential energy curves for the 40S-5S Rydberg molecules. Shown are the triplet (red) and the mixed singlet-triplet (green) potential energy curves for both hyperfine levels $F = 1$ and $F = 2$ of the 5S ground state of ^{87}Rb. The triplet potentials are the same for both hyperfine levels and also the same as shown in figure 4.4. The mixed singlet-triplet potential for the $F = 1$ hyperfine state is deeper than for the $F = 2$ hyperfine state. Zero on the vertical axis corresponds to the energy of the respective hyperfine state in zero magnetic field.

out if they are pointing in opposite directions. This Zeeman shift than enters the matrix representation of the Hamiltonian given in equation (4.35) only on the diagonal terms if both $m_{\mathrm{S,g}}$ and $m_{\mathrm{S,r}}$ are the same. The structure of the Hamiltonian is shown schematically, with each interaction corresponding to a different color, in figure 4.8. In this figure the interaction of the nuclear spin with the magnetic field was neglected, because it is only a small effect since the magnetic moment of the nucleus is almost negligible compared to the magnetic moment of the electron. This interaction can also be included in the matrix. This Hamiltonian still conserves the total quantum number M and as such the system can in principle be reduced to smaller sub-spaces.

To obtain the new molecular potentials, including the interaction with the magnetic field, the Hamiltonian given by equation (4.39) has to be diagonalized. The new eigenvalues are no longer given by the eigenvalues given in equations (4.36)-(4.38), as the magnetic field leads to further mixing of the states. As such the obtained eigenvalues can in principle not be labelled as triplet and mixed potential as we did for the eigenvalues without the magnetic field. In this thesis however we will stick to the notation in zero magnetic field, where the potentials could be grouped into two families: the triplet and the mixed family. In the appendix A.1 the dependency of the obtained potentials on the strength of the

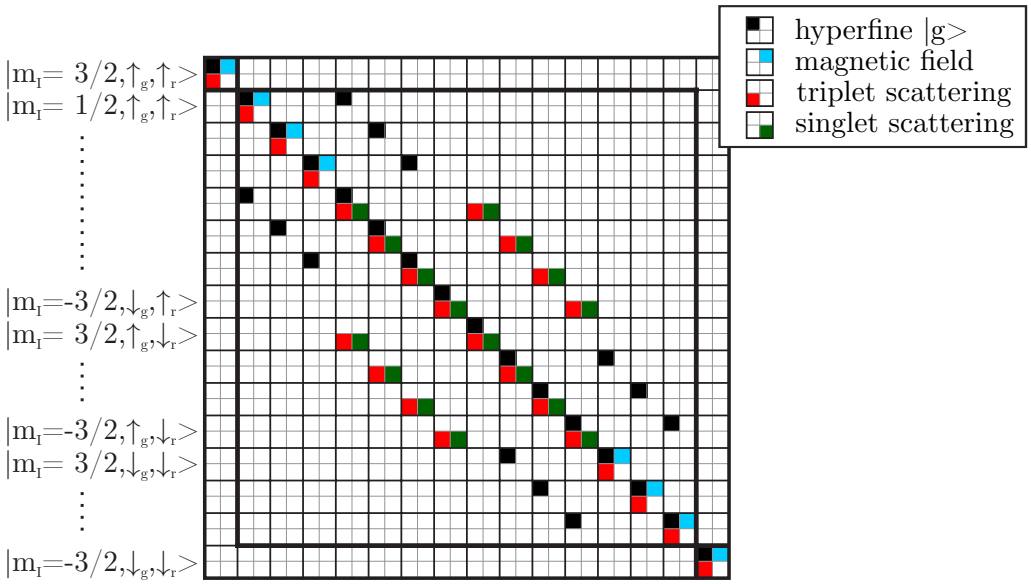

Figure 4.8.: Schematic illustration of the structure of the matrix representation of the Hamiltonian (4.39). The respective terms of the interactions are marked in different colors. Blank square indicates a zero in the Hamiltonian.

magnetic field is discussed for all obtained potential energy curves.

As can be seen in figure 4.8, the outermost states of the matrix are the only states that do not couple to other states and as such are the only ones affected purely by triplet scattering. All the obtained potential energy curves are shown in figure 4.9 for a magnetic field of 2.35 G, which was the magnetic field used for most of the measurements that will be presented later. In this figure the potentials belonging to the mixed family are drawn in green, while the potentials of the triplet family are drawn in red. An exemplary wavefunction calculated for a bound state in the experimentally accessible triplet potential is shown in blue. The uppermost and the lowermost state for $F = 2$, are the states that do not couple to other states and are as such the only pure triplet states. In the measurements presented in the previous section, the Rydberg atoms were always excited to the state corresponding to the highest potential energy curve of the $F = 2$ state and were therefore purely triplet.

In the described experiment not all of the potential energy curves shown in figure 4.9 are accessible, because the atoms are prepared to be spin polarized inside the magnetic trap. In order to obtain the potentials that are of interest, the overlap $|\langle\psi_{\mathrm{ex}}|\psi_{\mathrm{eig}}\rangle|^2$ of the calculated eigenstates with the atomic state, that can be excited, has to be calculated. For the measurements done in this thesis this is the $|m_{\mathrm{I,g}} = 3/2, m_{\mathrm{S,g}} = 1/2, m_{\mathrm{S,r}} = -1/2\rangle$ state. The overlap of the calculated eigenstates with the state that is excited in the experiment of course also depends on the internuclear distance, as the scattering that mixes the states depends on the internuclear separation. The calculated overlap $|\langle\psi_{\mathrm{ex}}|\psi_{\mathrm{eig}}\rangle|^2$ as a function of the internuclear distance is shown in figure 4.10. For the ground state of

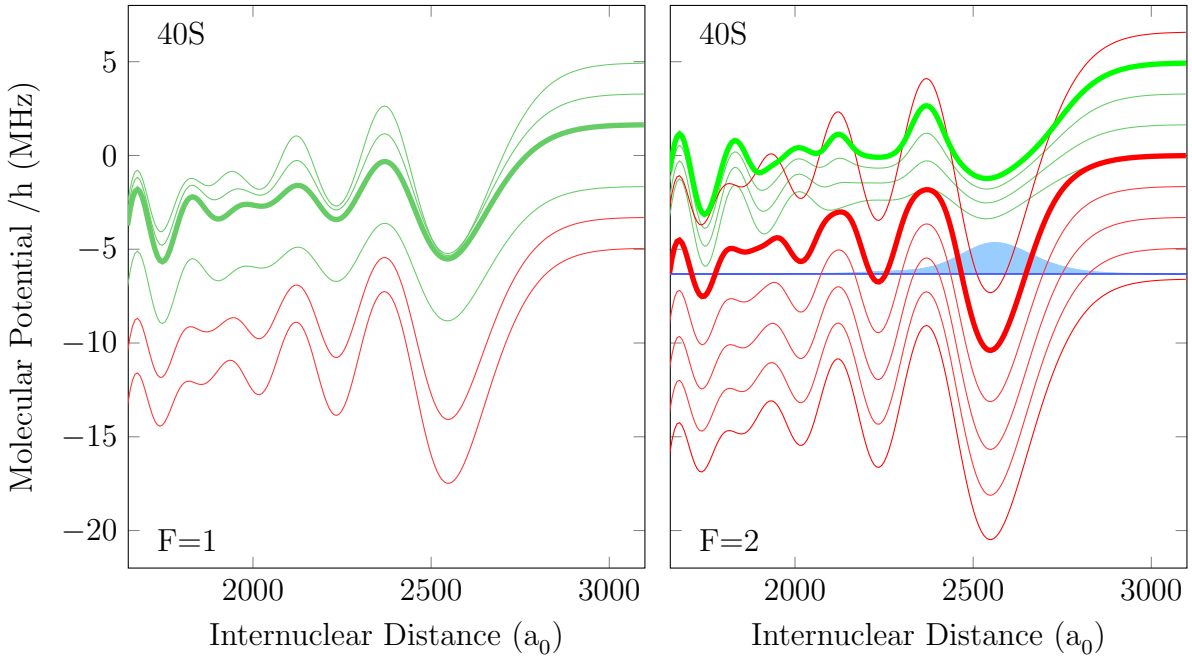

Figure 4.9.: Molecular potential energy curves for the 40S-5S Rydberg molecules as a function of the internuclear distance R calculated by diagonalizing the Hamiltonian given in equation (4.39), using the pure singlet and triplet potentials obtained with the full diagonalization method. The inclusion of the hyperfine interaction of the 5S ground state atom leads to the mixing of singlet and triplet scattering channels. In zero magnetic field the molecular potentials can be grouped in two different families: triplet (red) and mixed (green) potential energy curves. The applied magnetic field of B=2.35 G leads to further mixing and also splits the potentials apart by the Zeeman shift of the asymptotic atomic energy levels. In the experiment we address the triplet and mixed molecular states of F=2 which are indicated with thick red and green lines, respectively. The substate of F=1 plotted with a thick green line has a very small overlap with the initial state and thus was not observed in the experiment. As an example a bound state inside the accessible triplet potential is shown in blue. Zero on the vertical axis corresponds to the asymptotes of the respective degenerate hyperfine state ($F = 1,2$) in zero magnetic field.

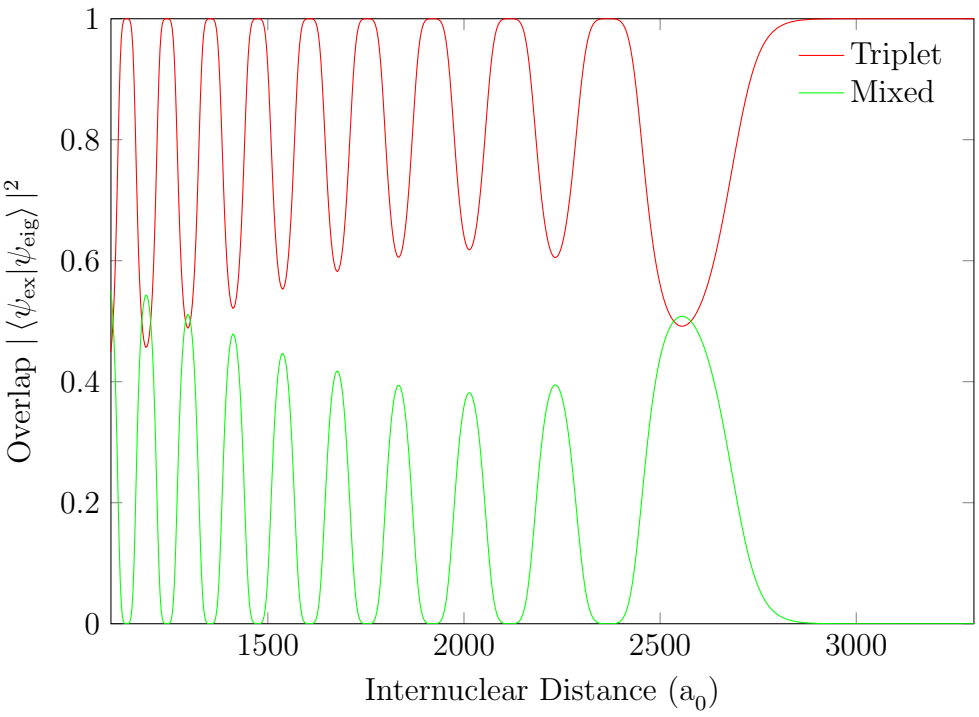

Figure 4.10.: Calculated overlap of the eigenstates $|\psi_{eig}\rangle$ of the Hamiltonian given by equation (4.39) with the state $|\psi_{ex}\rangle = |m_{I,g} = 3/2, m_{S,g} = 1/2, m_{S,r} = -1/2\rangle$ that is excited in the experiment as a function of the internuclear distance for a magnetic field of 2.35 G. For the ground state of the Rydberg molecules only the overlap for the outermost well of the potentials is decisive. Another state also has a non-zero overlap with the state that is excited, but this overlap is very small compared to the two states shown here and is as such not visible in the figure.

the Rydberg molecules only the overlap $|\langle\psi_{ex}|\psi_{eig}\rangle|^2$ in the outermost well of the potential energy curve, where the ground state atom is bound by the electron-neutral scattering, is crucial. This overlap depends not only on the scattering, but also on the amplitude of the external magnetic field. This dependency on the magnetic field is shown in figure A.3 of the appendix. For the state that is excited in the experiment there are three eigenstates that have a non-zero overlap. These three eigenstates are the potentials that are shown in a thick line in figure 4.9. However the eigenstate corresponding to the potential at $F = 1$ has such a small overlap that it was not observed in the experiment. This is because the scattering interaction is small compared to the hyperfine splitting, leading only to small perturbations.
The dependency of the bound molecular ground state in the two potentials of interest (thick lines for $F = 2$ in figure 4.9) is shown in figure 4.11. The zero of the vertical axis in this figure is the transition to the atomic $|m_{I,g} = 3/2, m_{S,g} = 1/2, m_{S,r} = 1/2\rangle$-state. For this state the energy level of the ground state and the Rydberg state are shifted by the

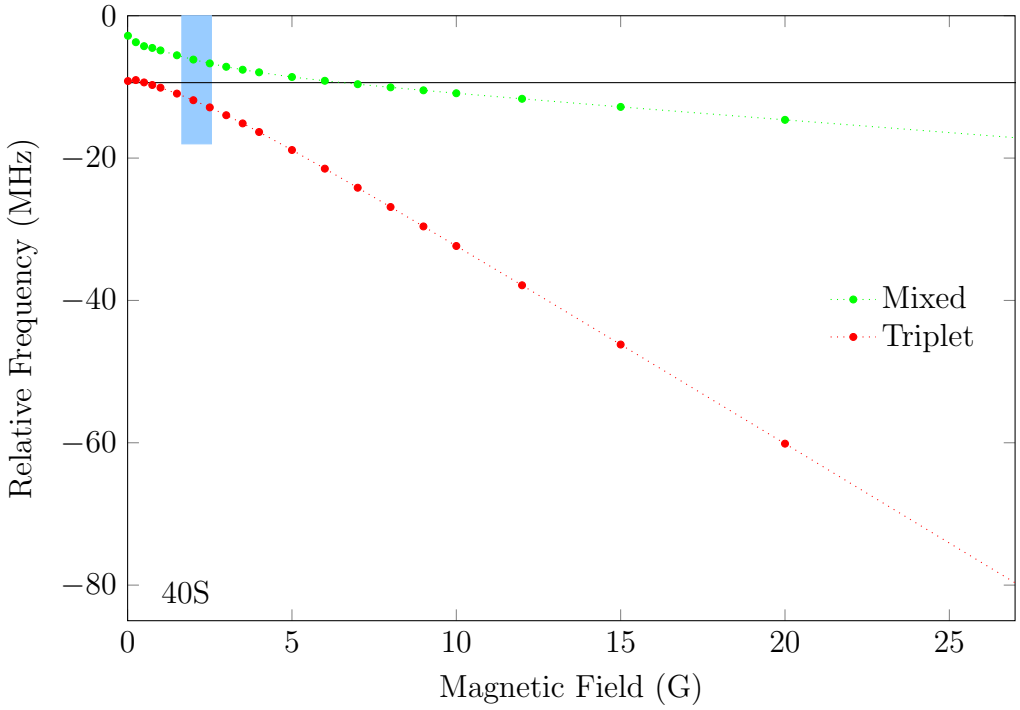

Figure 4.11.: Dependence of the relative frequency of the bound molecular states that are accessible in the experiment on the amplitude of the magnetic field. Zero on the vertical axis corresponds to the transition to the atomic $|m_{\mathrm{I,g}} = 3/2, m_{\mathrm{S,g}} = 1/2, m_{\mathrm{S,r}} = 1/2\rangle$-state, for which the relative laser frequency stays the same. This atomic state is the asymptote of a pure triplet potential, for which the binding energy (black line) of the molecular ground state does not depend on the magnetic field. The range that was measured in the experiment is shown in light blue.

same amount in an external magnetic field and as such the relative laser frequency used to excite the Rydberg state stays the same. Hence, this transition is always used as a reference in the experiment. Furthermore the molecular potential corresponding to this atomic state is not changed by the magnetic field and as such the relative frequency of the bound molecular ground state in this pure triplet potential also stays at the same frequency, which is shown by the black line at -9.4 MHz. The non-linear behaviour that can be seen in figure 4.10 can be explained by the dependence of the potentials on the magnetic field. For small magnetic fields the mixed potential becomes deeper and the triplet potential gets more shallow. This effect saturates after a certain magnetic field and the potential depth stays the same. From this point on, only the linear Zeeman effect of the asymptote of the potentials is observed. This dependency on the magnetic field is also shown in the appendix A.1 in figure A.1 for all potentials and in figure A.2 for the binding energies of the molecules for the other principal quantum numbers.

Up to now only the hyperfine structure of the 5S ground state was included in the calcu-

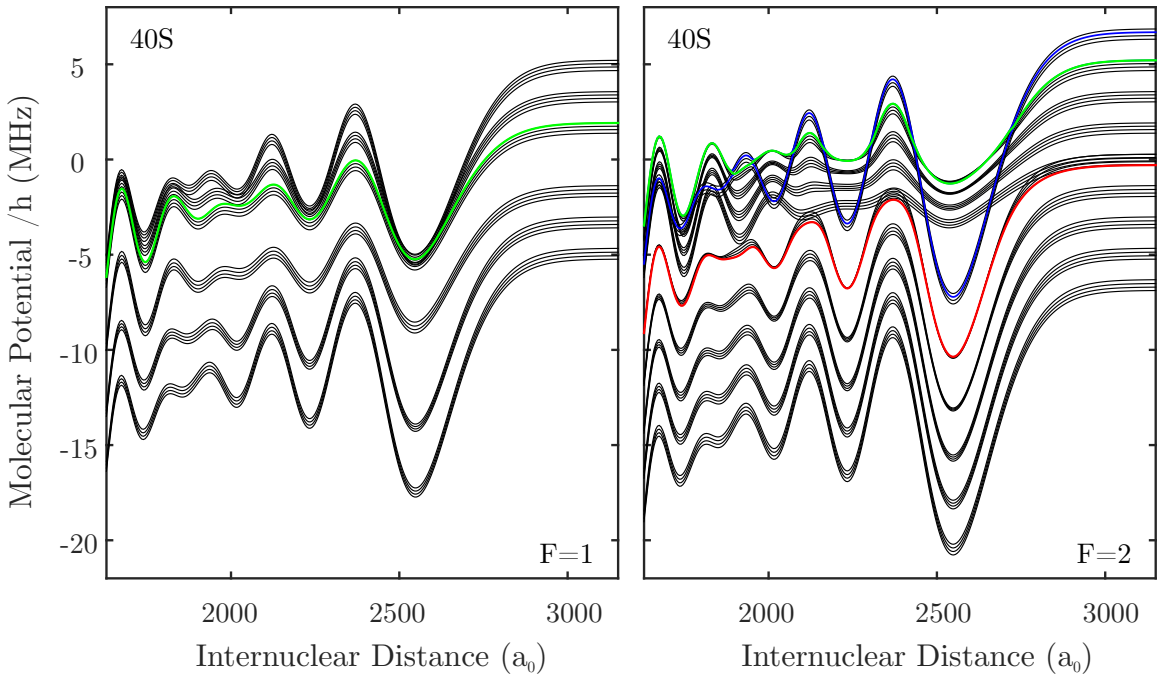

Figure 4.12.: Molecular potential energy curves for the 40S-5S Rydberg molecules with mixed singlet-triplet scattering, interaction with an external magnetic field and the hyperfine structure for both the 5S ground state and the Rydberg state. For the Rydberg state the magnetic field is large enough to be in the strong B-field regime and as such there are always 4 potentials following more or less the same behaviour. The potential energy curves that are accessible in the experiment are shown in green for the mixed potentials and in red for the triplet potential. By changeing the nuclear spin of the Rydberg atom during the excitation, it is also possible to end up in the potential shown in blue, which was not accessible without the inclusion of the nuclear spin of the Rydberg atom. The zero of the vertical axis again corresponds to the energy of the degenerate hyperfine state (F=1,2) in zero magnetic field.

lation. For the Rydberg state there is also a coupling of the electron and the nuclear spin, which is, as described in chapter 2.2, considerably weaker due to the large electron orbit, but still on the order of the measurement resolution. As such the hyperfine structure of the Rydberg state was also included in the calculation of the mixed potential energy curves. In order to do this, one has to include the 8 hyperfine states for the nS Rydberg state instead of only the two electron spin states. With this the Hamiltonian is then given by

$$\hat{H}(R) = \hat{H}_{\mathrm{B}} + \hat{H}_{\mathrm{HF,g}} + \hat{H}_{\mathrm{HF,r}} + V_{\mathrm{S}}(R) \cdot \hat{P}_{\mathrm{S}} + V_{\mathrm{T}}(R) \cdot \hat{P}_{\mathrm{T}} \,, \tag{4.40}$$

with the hyperfine interaction for both the ground state $\hat{H}_{\mathrm{HF,g}}$ and the Rydberg state $\hat{H}_{\mathrm{HF,r}}$. The Hilbert space is then 64-dimensional, which leads to a 64×64 matrix as the

representation of the Hamiltonian. This Hamiltonian now conserves the total quantum number $M' = m_{\mathrm{I,g}} + m_{\mathrm{S,g}} + m_{\mathrm{S,r}} + m_{\mathrm{I,r}}$, meaning that the Hilbert space can be divided up into sub-spaces of fixed M'.
The molecular potential energy curves obtained by diagonalizing this matrix are shown in figure 4.12. The potentials that are accessible in the experiment are again shown in green for the mixed family and in red for the triplet family of potentials. For the used magnetic field we are already in the strong B-field regime for the hyperfine structure of the Rydberg state. As such each potential shown in figure 4.9 splits apart into 4 potentials, that are only separated by about 200 kHz depending on the principal quantum number [49, 68, 69]. For the different potentials there are some crossings and some anti-crossings, that are not visible in the figure. To see which states can be excited, the overlap $|\langle\psi_{\mathrm{ex}}|\psi_{\mathrm{eig}}\rangle|^2$ of the calculated eigenstates with the state that is excited by the lasers is again calculated. With the inclusion of the hyperfine interaction of the Rydberg state, there is now a fourth potential energy curve (shown in blue in figure 4.12), which has a non-zero overlap with the state that is excited in the experiment. This will become clear by looking at the excitation scheme used in the experiment, which will be done in the next section.

4.4. Experimental realization and results

With the scheme of the Rydberg excitation as it was shown in figure 3.5 on page 19, the spin of the electron in the Rydberg state will be conserved, with respect to the spin of the electron in the 5S ground state, during the excitation. This leads to a pure triplet scattering interaction of the Rydberg electron with neighbouring ground state atoms, where the valence electron is in the 5S ground state. This pure triplet state does not couple to any other states, as it can be seen in the matrix shown in figure 4.8 where this state corresponds to the first row of the matrix.
In order to observe mixed singlet-triplet Rydberg molecules, it is necessary to change the polarization of the two excitation laser beams, so that the spin of the Rydberg electron is flipped during the excitation. For this the polarization of the 420 nm laser was changed to σ^-, so that the intermediate state is not a stretched state anymore. With this polarization the atoms will be excited to a $m_{\mathrm{F}} = 1$ intermediate state, which consists of states with different values of m_{J}. Using π-polarized 1020 nm light, the excited Rydberg state will then also be a state with $m_{\mathrm{F}} = 1$. This excitation scheme is shown schematically in figure 4.13a. The experiment is conducted in the strong B-field regime for the hyperfine interaction of the Rydberg state, due to the magnetic offset field which is necessary for the magnetic trap in the experiment. This means that the atoms will be excited to a state with $m_{\mathrm{S,r}} = 1/2$ as well as a state with $m_{\mathrm{S,r}} = -1/2$, corresponding to the second highest and the lowest line for large magnetic fields in figure 2.1 on page 8. With this the atoms will end up in a pure triplet state as well as a state with mixed singlet-triplet interaction. The state with pure triplet scattering interaction is the $|m_{\mathrm{I,g}} = 3/2, m_{\mathrm{S,g}} = 1/2, m_{\mathrm{S,r}} = 1/2, m_{\mathrm{I,r}} = 1/2\rangle$-state, for which the molecular potential was already shown in blue in figure 4.12.
Increasing the two-photon detuning of the two excitation laser from the intermediate state

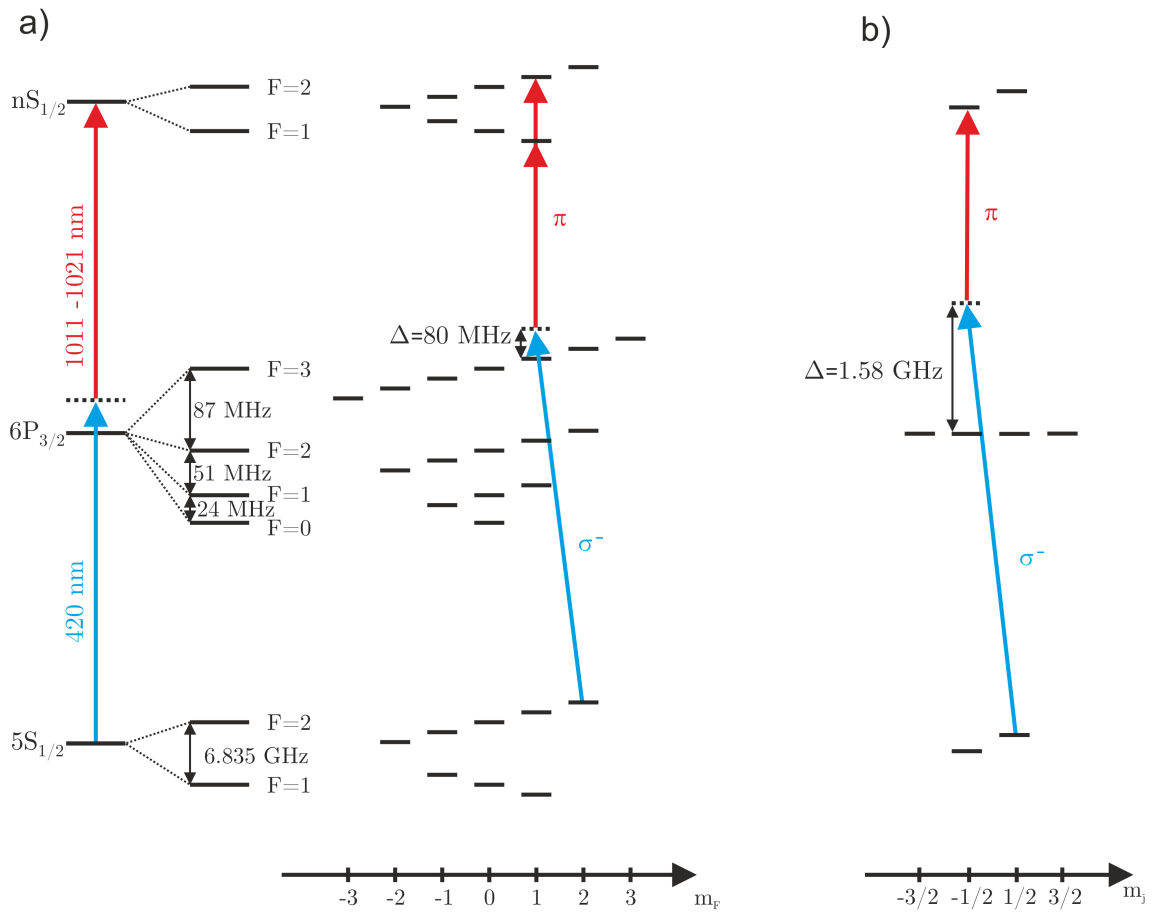

Figure 4.13.: Excitation scheme used for the excitation of the mixed singlet-triplet Rydberg molecules. The atoms are initially prepared in the 5S, $F = 2, m_F = 2$ state and then excited with σ^--polarized 420 nm and π-polarized 1020 nm light to the two $m_F = 1$ sub-states of the nS Rydberg state (a). By increasing the detuning to the intermediate state it is possible to neglect the hyperfine splitting of the $6P_{3/2}$-state, so that the excitation can be looked at in the J-basis. With this the atoms are only excited to the $m_S = -1/2$ Rydberg state (b).

sufficiently, that the hyperfine structure of the $6P_{3/2}$ state can be neglected, it is possible to excite the atoms mainly to the Rydberg state with $m_{S,r} = -1/2$. This is shown schematically in figure 4.13b. In the experiment a two-photon detuning of 1.58 GHz to the intermediate state was used.
With this excitation scheme shown in figure 4.13b, the state of interest for the two-body scattering interaction is then the $|\uparrow_g\downarrow_r\rangle$-state, where the electron of the Rydberg atom has spin down and the electron of the ground state atom spin up. This state is not an eigenstate of the system of two spin 1/2 particles and it can be written as a superposition of the singlet and triplet eigenstates.

$$|\uparrow_g\downarrow_r\rangle = \frac{1}{\sqrt{2}}\left(\underbrace{\frac{1}{\sqrt{2}}\left(|\uparrow_g\downarrow_r\rangle + |\downarrow_g\uparrow_r\rangle\right)}_{\text{triplet state}} + \underbrace{\frac{1}{\sqrt{2}}\left(|\uparrow_g\downarrow_r\rangle - |\downarrow_g\uparrow_r\rangle\right)}_{\text{singlet state}}\right) \tag{4.41}$$

Already by looking at this state, the mixing of singlet and triplet scattering channels can be explained. By including the nuclear spin of both the ground state and the Rydberg state, the resulting excited state is the $|m_{I,g} = 3/2, m_{S,g} = 1/2, m_{S,r} = -1/2, m_{I,r} = 3/2\rangle$ state. The molecular potentials with a non-zero overlap with this state were already shown in different colors in figure 4.12.

4.4.1. Molecular spectroscopy in a thermal cloud

For the measurements of the Rydberg molecules, a spin polarized atomic sample of approximately $3.2 \cdot 10^6$ ^{87}Rb atoms, at a temperature of about 800 nK, in the magnetically trapped 5S, $F = 2, m_F = 2$ state was prepared with the experimental cycle as it was described in chapter 3. With the parameters of the magnetic trap this leads to a peak density of about $5.5 \cdot 10^{13}\,\mathrm{cm}^{-3}$ for the thermal cloud. The atoms are then excited with 20 µs laser pulses via the two-photon excitation shown in figure 4.13b. The excitation pulses are repeated with a repetition rate of 2 kHz. After each excitation pulse the Rydberg atoms are field-ionized within 500 ns and the ions are subsequently detected with a micro-channel plate. In a single atomic cloud, 4000 excitation and ionization pulses are applied. Thereby the frequency of the excitation laser is fixed and only changed from cloud to cloud. The obtained ion signal is then averaged over a number of atomic clouds per frequency, in order to get a better signal-to-noise ratio. Over the course of the 4000 excitation pulses the temperature of the atomic cloud increases up to about 1.8 µK and the atom number decreases to about $2.8 \cdot 10^6$, which leads to a decrease of the peak density to about $1.5 \cdot 10^{13}\,\mathrm{cm}^{-3}$. For the evaluation of the spectra in the thermal cloud, only the first 1000 excitation pulses are used, as the molecular peaks vanish if the density of the cloud decreases too much.
The applied magnetic field is calibrated by the frequency separation of the two atomic transitions to the $m_{S,r} = 1/2$ and $m_{S,r} = -1/2$ Rydberg state. The magnetic field can also be measured by looking at the atom number for different frequencies of the evaporative cooling. Both methods to determine the magnetic field match within a maximal deviation of about 15%.

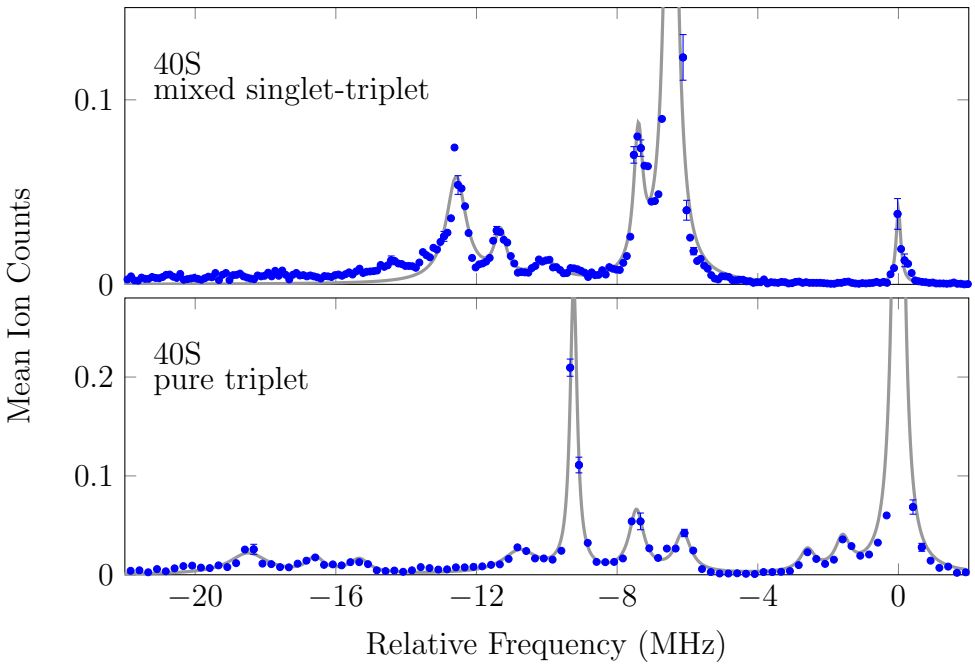

Figure 4.14.: Comparison of a spectrum of the 40S Rydberg state using the normal excitation scheme shown in figure 3.5 and the far detuned excitation scheme shown in figure 4.13b. In the pure triplet spectrum the molecular dimer and trimer lines are visible, as they were already discussed in section 4.2. The mixed singlet-triplet spectrum has a peak of the atomic transition to the $m_{S,r} = -1/2$ Rydberg state at -6.5 MHz and a small leftover peak of the atomic transition to the $m_{S,r} = 1/2$ state at zero. There are two peaks at -7.4 MHz and -12.6 MHz, that correspond to the bound molecular ground state in the mixed singlet-triplet and the triplet potential that are accessible with the mixed excitation scheme (see figure 4.9 or 4.12). Also two peaks corresponding to excited molecular states in the triplet potential are visible in the spectrum. The grey lines are Lorentzian fits plotted for better visibility.

In figure 4.14 the measured spectrum of the 40S Rydberg state is shown for the pure triplet excitation scheme shown in figure 3.5 and for the excitation scheme shown in figure 4.13b, which leads to the spin flip during the excitation. The zero of the frequency axis is the same for both spectra, but it can be seen that for the mixed spectrum the highest peak, which corresponds to the atomic transition, is at -6.5 MHz. This is the expected Zeeman-shift of the atomic transition to the spin down Rydberg state in a magnetic field of 2.35 G. There is also some leftover signal at zero, due to the polarization of the laser beams, which is not perfect in the inhomogeneous magnetic field, and due to the fact that the hyperfine structure of the intermediate state can not be neglected completely. The grey lines are Lorentzian fits to the data, which are plotted for better visibility. In the pure triplet spectrum several molecular states are visible: the ground state of the dimer

at -9.3 MHz, the ground state of the trimer at -18.6 MHz and also several excited states. In the mixed spectrum there are no peaks visible that directly correspond to the peaks in the pure triplet spectrum. In the mixed singlet-triplet spectrum shown in figure 4.14b there are two molecular peaks, which are higher than all the others, that correspond to the molecular ground states bound in the two accessible potentials shown in figure 4.9. The peak corresponding to the molecular ground state in the triplet potential is at -12.6 MHz and the peak corresponding to the ground state in the mixed potential is at -7.4 MHz. For the triplet potential there are also excited molecular states visible at -11.3 MHz and -10.0 MHz. From these binding energies it can already be seen, that the accessible triplet potential is not the same as the pure triplet potential anymore, as the binding energy of the molecular ground state measured to the respective asymptotic atomic transition is clearly smaller than the binding energy of the ground state in the pure triplet potential. This shift of the triplet potential is due to the influence of the magnetic field, which is discussed in appendix A.1.
The measured spectra for various principal quantum numbers in the range of $n = 36 - 45$ are shown in figure 4.15. In this figure the zero of the frequency axis again corresponds to the atomic transition to the spin up nS Rydberg state. The large peak at -6.5 MHz again corresponds to the spin down Rydberg state, which is shifted by the Zeeman effect due to the applied magnetic field of 2.35 G. The outermost peak at the lowest frequency in each spectrum is attributed to the molecular ground state in the accessible triplet potential. The peak at higher frequencies with similar signal strength is attributed to the ground state bound in the mixed singlet-triplet potential. The peaks in between these peaks are attributed to excited states bound in the triplet potential. However, the observed excited states will not be further discussed in the scope of this thesis.
In figure 4.15 also the calculated peak positions, using the pure scattering potentials from a full diagonalization method as well as an effective zero-energy s-wave scattering length approach, are shown. For the effective s-wave scattering length approach, the triplet scattering is extracted from previous measurements of pure triplet Rydberg molecules done in the institute, which include states with the principal quantum number ranging from $n = 34 - 71$ [29, 36]. The zero-energy triplet scattering length is thereby adjusted to these experimental data sets in a least-square fit, leading to a value of $a_{0,\mathrm{T}} = -15.7\, a_0$. With this fixed value there is only one free parameter in an effective scattering length approach that can be adjusted to fit the experimental data shown in figure 4.15: the zero-energy singlet scattering length. The singlet scattering length is therefore fitted to the experimental data in a least-square fit, obtaining a value of $a_{0,\mathrm{S}} = -0.2\, a_0$. The peak position obtained using these effective scattering lengths and the Fermi-pseudopotential are shown as red and green lines in figure 4.15, corresponding to the molecular ground state in the accessible triplet and mixed potential, respectively. To show the sensitivity of this approach on the singlet scattering length the obtained values of the peak position are also shown as dashed lines for a change of $\pm 0.5\, a_0$ in the singlet scattering length. The change in the peak positions for the triplet potential, given by changing the singlet scattering length, is so small, that it is not shown in the figure. It is important to note, however, that a change of the triplet scattering length strongly influences both the triplet and mixed potentials. This simple

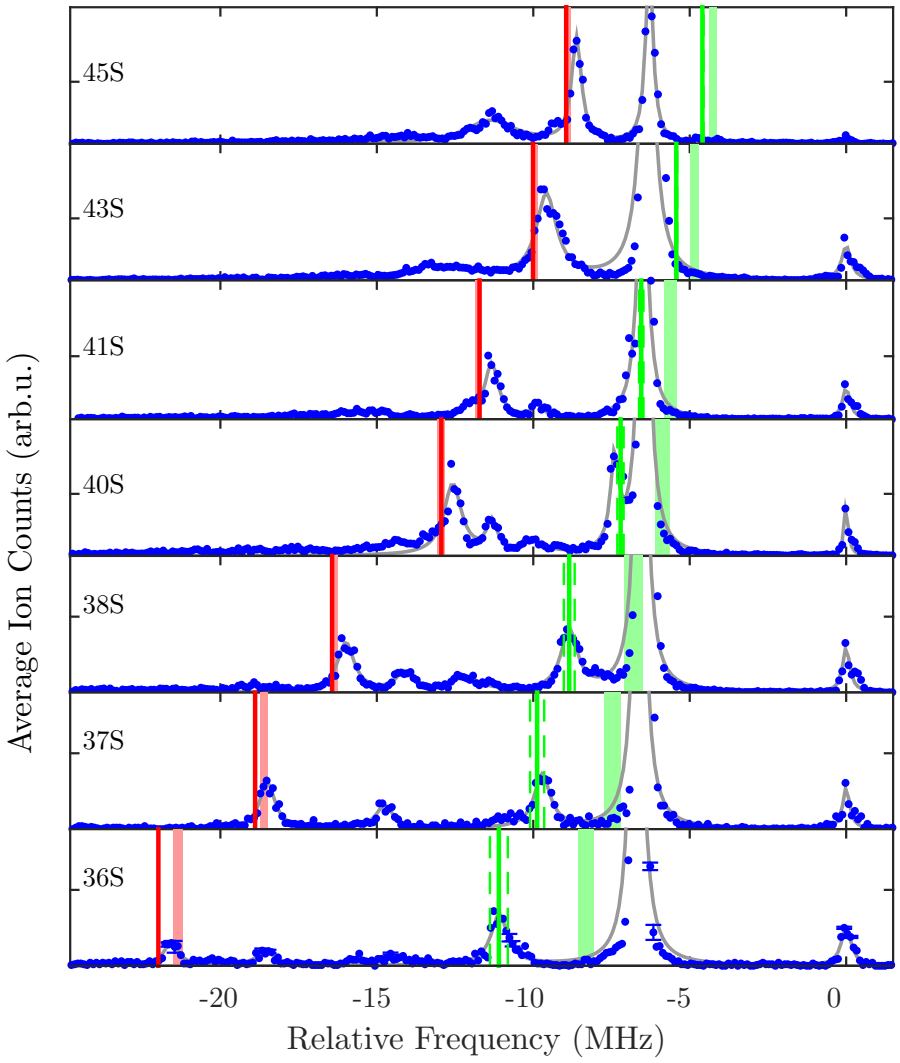

Figure 4.15.: Spectra of Rydberg states for different principal quantum numbers in the range of $n = 36 - 45$. The zero of the frequency axis corresponds to the atomic transition to the spin up nS Rydberg state. The highest peak at -6.5 MHz corresponds to the atomic transition to the spin down Rydberg state in the applied magnetic field of 2.35 G. Red detuned from the atomic transitions several peaks corresponding to bound molecular states are visible. The shaded red and green areas show the calculated binding energies for the triplet (red) and mixed (green) potential shown in figure 4.12, using the full diagonalization method for the calculation of the pure scattering potentials. The shaded region thereby corresponds to the sensitivity of the calculation on the boundary conditions of the potential used to solve the Schrödinger equation. The red and green straight lines correspond to the calculation using an effective zero-energy s-wave scattering length approach. For this we take a fixed value for the triplet scattering length $a_{0,\mathrm{T}} = -15.7\,a_0$, while the singlet scattering length is fitted to the data. The green dashed lines indicate the sensitivity of the peak positions on a change of the obtained singlet scattering length $a_{0,\mathrm{S}} = (-0.2 \pm 0.5)\,a_0$.

perturbative approach allows the prediction of the molecular peaks with a good accuracy and can be used to estimate the peak positions for future experiments.
It could already be seen in figure 4.4 that the p-wave contribution and the energy dependence of the scattering (especially for the singlet scattering) have a strong influence on the shape of the scattering potentials. Because of this the binding energies of the molecules were also calculated for the mixed potentials shown in figure 4.12, in which the pure singlet and triplet scattering potentials obtained from a full diagonalization of the scattering Hamiltonian were used. The energy dependence and the p-wave scattering lead to an outermost lobe of the mixed potential, that is not as deep as it is for s-wave scattering only. As such the outermost lobe becomes comparable with the second last lobe, leading to bound states that are delocalized over multiple potential wells. This effectively lowers the binding energy of these delocalized molecular states. The calculation of the binding energies with this method, however, depends somewhat on the boundary conditions that are used for solving the Schrödinger equation. To reflect this sensitivity in the calculation of the binding energies, a shaded range is shown in figure 4.15 for the calculated peak positions. The calculated peak positions using this method, including the p-wave scattering contribution and the energy dependence of the scattering, deviate at most by 2.5 MHz, which is quite good as there are no free parameters in the calculation. This also shows that the electron-Rubidium scattering phase shifts [22] that are used in the calculations are quite accurate. Nonetheless the deviation that can be seen in between the high resolution data and the calculated peak positions could in the future be used to refine these phase shifts. It is important to note that there are already more recent calculations for the scattering phase shifts [23] which include relativistic effects, that were, however, not available for the calculations done during this thesis. In the future the shown data, together with a better precision of other input parameters, like e.g. the polarizibility of the 5S ground state of Rubidium, can lead to a significant improvement of the calculation of the scattering phase shifts.
What can not be seen in figure 4.15, is that the peak of the atomic transition to the spin down state appears to be asymetrically broadened. Thereby a 'shoulder' is visible for frequencies closer to zero, that is more pronounced for the lower quantum numbers and is not visible anymore for the high quantum numbers that were measured. This can be explained by the inhomogeneous magnetic field caused by the magnetic trap, which means that the polarization of the laser beams is not perfect at every position of the trap. Because of this it is possible to also excite different hyperfine states with a finite probability.
To test this a high resolution measurement was done for the 36S Rydberg state, which is shown in figure 4.16. Here a smaller magnetic field than in the previous measurements of roughly 1.2 G was used, in the hope to see a bigger effect of the hyperfine structure. However, even for the lower magnetic field that was applied, we are still in the strong B-field regime with respect to the hyperfine splitting of the 36S Rydberg state. For the measurement 50 µs excitation pulses were used, in order to use a smaller frequency step size. In figure 4.16 a double structure of the atomic transition peak is clearly visible. Fitting a double Lorentzian function to the data yields a separation of 265 kHz of the two peaks. This separation agrees quite well with the expected splitting of about 220 kHz of

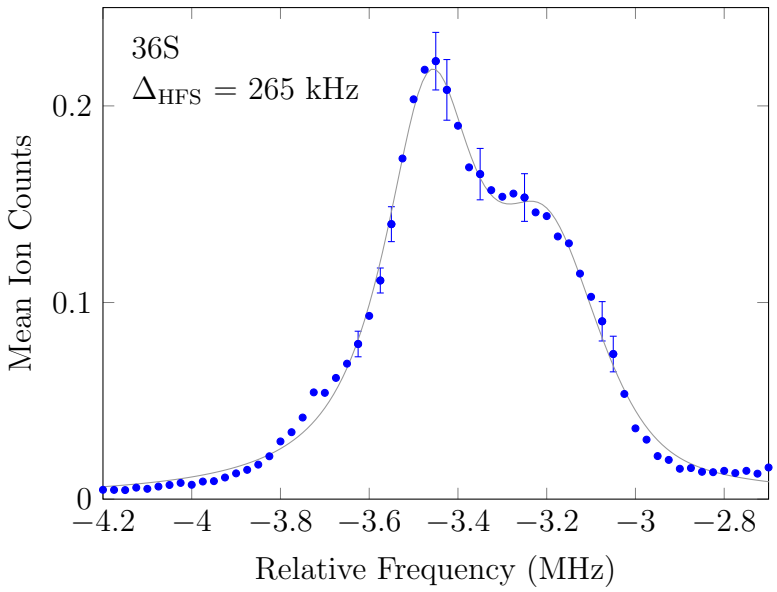

Figure 4.16.: High resolution measurement of the atomic transition to the spin down Rydberg state. It can be seen that the line is broadened asymmetrically, which can be explained by the different hyperfine states that might be excited due to imperfect polarizations of the excitation laser beams. A double Lorentzian fit gives a spectral separation of 265 kHz, which agrees quite well with the expected separation of the different hyperfine levels of the 36S Rydberg state in the strong B-field regime. The grey line is a double-Lorentzian fit plotted for better visibility.

two neighbouring hyperfine levels in the applied magnetic field.

As a next step, the dependency of the observed molecular states on the magnetic field was studied. In the experiment the magnetic field was varied in a small range from about 1.5 G up to 2.5 G by applying an offset field. By applying an offset field in the direction of the Ioffe coil only the trap bottom changes and not the position of the atomic cloud. However, by doing this the number of atoms in the thermal cloud changed, which is most likely due to the RF ramps used for the evaporative cooling. By adjusting these ramps further than just changing the frequency at the end, it should be possible to measure at even higher (and also a bit lower) magnetic offset fields. The measured spectra of the 40S Rydberg state for different amplitudes of the magnetic offset field are shown in figure 4.17. It can be seen that the peak at zero frequency, which corresponds to the transition from the 5S, $F = 2, m_{\mathrm{F}} = 2$ ground state to the spin up Rydberg state, does not move by changing the applied magnetic field. This is because the energy level of the ground state and the Rydberg state are shifted by the same amount due to the Zeeman-effect and as such the relative laser frequency necessary to excite the atoms to the Rydberg state stays the same. For the transition to the spin down Rydberg state, this is not the case and it can be seen in the figure that the highest peak, corresponding to this transition, shifts from

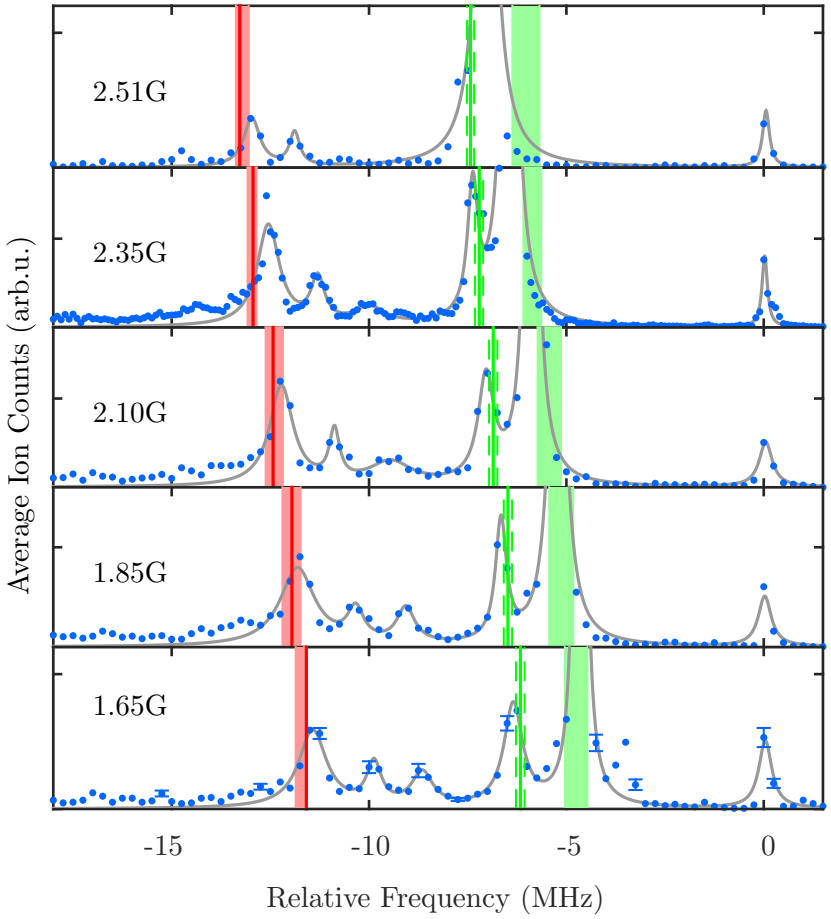

Figure 4.17.: Spectra of the 40S Rydberg state for different amplitudes of the applied magnetic field. The zero of the frequency axis corresponds to the atomic transition to the spin up nS Rydberg state, for which the relative laser frequency remains unchanged as the energy level of the ground and the Rydberg state are shifted by the same amount. The highest peak, which corresponds to the atomic transition to the spin down Rydberg state is shifted due to the Zeeman-effect in the applied magnetic field. For this the peak position changes from about -4.7 MHz to about -7.1 MHz for the measured range of the magnetic field. The peaks corresponding to the bound molecular states are also shifted by the applied magnetic field. The shaded red and green areas show the calculated binding energies for the triplet (red) and mixed (green) potential, using the full diagonalization method for the calculation of the pure scattering potentials. The shaded region thereby again corresponds to the sensitivity of the calculation on the boundary conditions of the potential used to solve the Schrödinger equation. The red and green straight lines correspond to the calculation using an effective scattering approach, with $a_{0,\mathrm{T}} = -15.7\,a_0$ and $a_{0,\mathrm{S}} = (-0.2 \pm 0.5)\,a_0$. The green dashed lines again show the sensitivity of the calculation on a change of the singlet scattering length.

about -4.7 MHz to about -7.1 MHz for the range of applied magnetic fields. It can also be seen that the peaks corresponding to molecular states are also shifted in the magnetic field. Again the calculated peak positions are shown in the spectra as red and green lines for the effective scattering length approach and as shaded red and green areas for the full diagonalization approach.

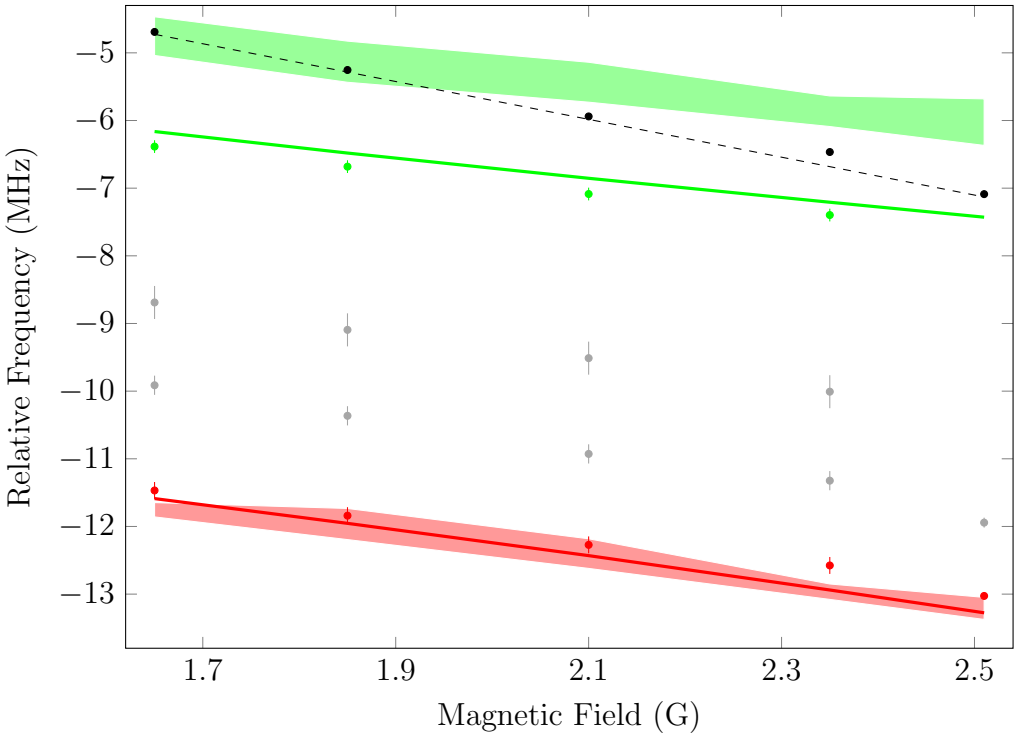

Figure 4.18.: Experimentally observed peak positions of the atomic spin down Rydberg state (black), the triplet molecular ground state (red) and the mixed molecular ground state (green) for the asymptotic 40S Rydberg state versus the amplitude of the applied magnetic field. The straight lines correspond to the calculated peak positions using the effective scattering length approach and the red and green shaded areas correspond to the calculation using the scattering potentials obtained from a full diagonalization method. The black dashed line shows the theoretical Zeeman shift of the atomic spin down Rydberg state, that was used to calibrate the magnetic field. The errorbars shown correspond to the 95% confidence bound of the Lorentzian fits used to obtain the peak positions. The grey dots correspond to the measured peak positions of the excited molecular states in the triplet potential.

It can be seen that the shift of the molecular peaks differs from the shift of the peak corresponding to the atomic transition. This is clearly visible for the mixed molecular state, because the separation to the atomic peak decreases and for the highest magnetic field that was measured the lines are not separated any more. The extracted positions of

	Atomic	Triplet	Mixed
Experiment	1.92 ± 0.28	1.23 ± 0.24	1.04 ± 0.17
Eff. Scattering Length	2	1.40 ± 0.07	1.05 ± 0.05
Full Diagonalization	2	1.27 ± 0.46	1.05 ± 0.27

Table 4.1.: Comparison of the experimentally obtained magnetic moments of the atomic state, the triplet and the mixed molecular states with the theoretically predicted values. The values are obtained from the slope of a linear fit, with the given uncertainties corresponding to the 95% confidence interval of the fit. The magnetic moments are given in units of the Bohr magneton μ_B. The magnetic moments are measured with respect to the transition from the 5S, $F = 2, m_F = 2$ ground state to the spin up Rydberg state, for which the relative laser frequency does not change, but the actual energy levels are shifted by the Zeeman-effect.

the peaks visible in figure 4.17 are shown as a function of the magnetic field amplitude in figure 4.18. In this figure the peak positions (dots) obtained from the shown Lorentzian fits (grey lines in figure 4.17) are shown for the transition to the atomic spin down Rydberg state in black, for the triplet molecular ground state in red and for the mixed molecular ground state in green. The dashed black line corresponds to the theoretical Zeeman-shift of the atomic spin down Rydberg state. The shaded red and green areas are the calculated peak positions using the full diagonalization approach, and the straight red and green lines are the calculated positions using the effective scattering length approach. In the case of the full diagonalizaton method the calculated peak positions differ from the measured positions, which was already seen in the spectra for the different principal quantum numbers.

For the effective scattering length approach the calculated peak positions were already shown in figure 4.11 for a wider range of magnetic field amplitudes. In the measurement the non-linear behaviour that can be seen in figure 4.11 is not observed, because the measured range of the magnetic field was to small. Because of this reason a linear function can be fitted to the data in order to extract the magnetic moments of the different observed states for the small range of measured magnetic fields. The magnetic moments obtained by this method are of course only valid in the small range of the applied magnetic field and are different for another range of magnetic fields. The values of the magnetic moments obtained from the slope of the linear fit are given in table 4.1 in units of the Bohr magneton μ_B. They are thereby measured with respect to the transition from the 5S, $F = 2, m_F = 2$ ground state to the spin up Rydberg state, for which the relative laser frequency does not change with the magnetic field. However the actual atomic energy level of this transition are both shifted by the Zeeman-effect. The obtained values from the experiment and the two theoretical values agree within the given uncertainties, even for the mixed molecules for which the calculation done with the full diagonalization method clearly differs in the peak positions. We find that the shift of the mixed as well as the triplet molecular peaks is

weaker than the Zeeman shift of two isolated atoms. This is due to the mixing of different spin orientations due to all contributions in the Hamiltonian given by equation (4.40). This dependency of the binding energy of the observed mixed singlet-triplet molecules on the magnetic field can in principle be used to engineer the molecular state.

4.4.2. BEC spectroscopy

To further study the effect of the mixed singlet-triplet scattering, a spectrum of the 53S Rydberg state was measured in a BEC. For this reason the frequency of the evaporative cooling was ramped down even further, until the temperature of the atoms is low enough and the density high enough for the phase transition to the condensed phase to happen. With this a spin polarized BEC of roughly $1.5 \cdot 10^6$ ^{87}Rb atoms in the magnetic trapped 5S, $F = 2, m_\mathrm{F} = 2$ ground state with an initial temperature of about $0.65 \cdot T_\mathrm{c}$ was prepared. With the trapping frequencies of the magnetic trap, this leads to a peak density of about $5.5 \cdot 10^{14}\,\mathrm{cm}^{-3}$, which means a mean interparticle separation of about $1200\,a_0$. The prepared BEC is shown schematically in figure 3.6 on page 20. For the evaluation of the BEC spectra only the first 50 excitation pulses are used, as the density of the BEC decreases by about 5% in the course of these 50 excitation pulses. By looking at the other excitation pulses that were measured, the melting of the BEC into a thermal cloud can be studied [5, 6].
A measurement of the 40S Rydberg state, using the excitation scheme which only yields triplet scattering interaction (shown in figure 3.5), was already shown in figure 4.6. For the 53S Rydberg state the pure triplet spectrum is shown in blue in figure 4.19, with the simulated spectrum [4] shown by the dotted blue line. Changing the polarization of the two excitation lasers in order to excite the spin down Rydberg state (excitation scheme shown in figure 4.13b), the observed spectra changes completely as can be seen by the red data points in figure 4.19. It is important to note, that the zero of the frequency axis is the same for both data sets. The atomic transition to the spin down Rydberg state is shifted by the Zeeman-effect due to the applied magnetic field of about 1.65 G and is visible as the beginning of the red spectrum at about -4.5 MHz. The signal at zero is again some leftover signal from the excitation to the spin up Rydberg state. It is clearly visible that the density shift and the broadening of the spectral line is not as pronounced for the mixed singlet-triplet excitation, as it is for the pure triplet scattering.
The molecular potential energy curves for the 53S Rydberg state in the applied external magnetic field are shown in the appendix A.3 in figure A.5. For the 53S Rydberg state the overlap of the molecular potentials with the state that is excited in the experiment is quite different than for the 40S Rydberg state, for which it is shown in figure 4.10. In the applied external field more or less only the triplet potential has a significant overlap, which can be also seen from the magnetic field dependence in figure A.3 in the appendix A.1. Also the depth of the accessible triplet potential is clearly reduced compared to the pure triplet potential. Another important point is that with the decrease of the depth of the potential, also the p-wave scattering contribution is changed compared to the pure triplet potential. It was shown in [4] that the crossing of the potential with the butterfly state

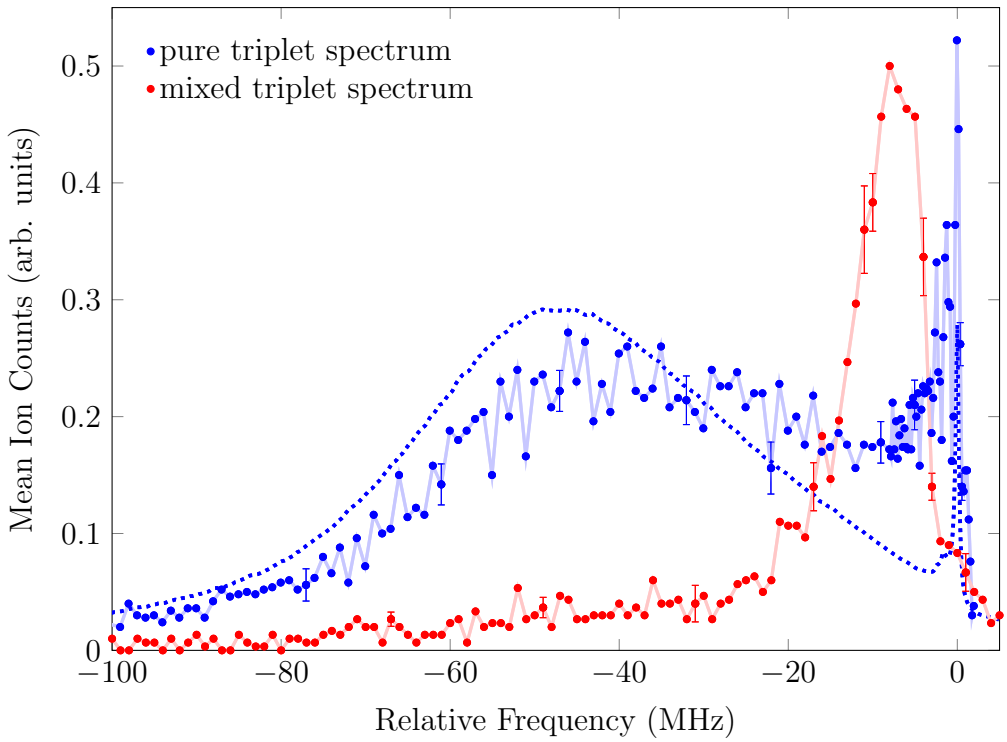

Figure 4.19.: Pure triplet (blue) and mixed singlet-triplet (red) spectrum of the 53S Rydberg state measured in a BEC with a peak density of about $5.5 \cdot 10^{14}\,\mathrm{cm}^{-3}$. The dotted blue line is a simulated spectrum for the case of pure triplet scattering [4]. The atomic transition to the spin up Rydberg state corresponds to the zero of the frequency axis for both spectra. The transition to the spin down Rydberg state is at roughly -4.5 MHz, since it is shifted by the Zeeman-effect in the external magnetic field of about 1.65 G. For some data points the standard error of the mean ion counts is shown exemplary in the spectrum.

(due to the p-wave shape resonance) leads to a broadening of the spectral line. Since the p-wave scattering contribution for the accessible triplet potential is different, this will also influence the broadening of the spectral line.

All in all the measurements shown in this section clearly show the effect of the mixing of singlet and triplet scattering channels on the spectroscopy of Rydberg states. For the spectra in the thermal atomic clouds, distinguishable molecular lines are visible in the spectrum, that can be attributed to bound molecular states in the calculated mixed singlet-triplet potential energy curves that are accessible in the experiment. These molecular states were shown for a range of principal quantum numbers $n = 36 - 45$ and also the dependence of these molecular states on the external magnetic field was shown for a small range magnetic field amplitudes. It could also be shown that the experimental data can be explained quite well by the theoretical model described in section 4.3. By measuring

in a BEC and as such by increasing the density of the atomic cloud, the distinguishable molecular lines disappear into a broad spectral line. For this case the effect of the mixing of singlet and triplet scattering is even more apparent as can be seen in the spectra shown in figure 4.19. The observed mean field shift and the broadening of the spectral line are clearly different for the two different cases.

5. Summary and Outlook

In the course of this thesis Rydberg molecules and in particular Rydberg molecules bound via mixed singlet-triplet scattering, were studied. These mixed singlet-triplet Rydberg molecules were spectroscopically observed in the range of $36-45$ of the principal quantum number n. For the measured Rydberg spectra in a sub-μK thermal cloud, distinguishable molecular lines are visible in the spectrum. These spectral lines can be attributed to bound molecular states in the potential energy curves caused by the Rydberg electron-neutral atom scattering. These potential energy curves were calculated using a simple theoretical model, which only takes the magnetic sub-states of the two atoms in the ground state and the nS-Rydberg state into account. It was shown that by choosing the polarization of the two excitation beams appropriately, it is possible to flip the spin of the Rydberg electron during the excitation, which leads to two accessible potential energy curves in the experiment. For the calculated potential energy curves, the mixing of the singlet and triplet scattering channels can not be neglected, as it was done for all the previous work done with pure triplet scattering, that was discussed in section 4.2.
In zero magnetic field, the obtained potential energy curves can be grouped into two families: pure triplet potentials and mixed singlet-triplet potentials. This results in two potential energy curves: one pure triplet and one mixed singlet-triplet, for both hyperfine states $F = 1,2$ of the 5S ground state. In contrast to previous works studying mixed singlet-triplet Rydberg molecules [2, 3] the applied magnetic field, which is used to trap the atoms in our experiment, further alters the potential energy curves. The applied magnetic field leads to increased mixing and the depths of the different potential energy curves change as a function of the magnetic field amplitude. This leads to a non-trivial dependence of the binding energy of these mixed singlet-triplet molecular states on the magnetic field and the respective magnetic moments also change as a function of the magnetic field. This dependence was studied theoretically for a wide range of magnetic field amplitudes (shown in figure 4.11) and also experimentally observed for a range of 1.65 - 2.51 G in section 4.4.1. In the experimentally observed range it could be seen that the obtained magnetic moments of the molecular states differ significantly from the respective asymptotic atomic energy level. This dependence on the magnetic field can in principle be used to engineer the molecular state, similar to what was already shown for the electric field [36, 37].
By increasing the density of the atomic sample, which is done by condensing the atoms into a BEC, the distinguishable molecular lines in the spectrum disappear into a broad spectral line. The effect of the high density was measured for the 53S Rydberg state for the Rydberg excitation leading to a pure triplet scattering interaction as well as the excitation leading to mixed singlet-triplet scattering and is shown in section 4.4.2. The pure triplet scattering interaction leads to a broad feature in the spectrum with a width of

about 60 MHz, while the excitation leading to mixed singlet-triplet scattering only leads to a feature with roughly 20 MHz width. For the 53S Rydberg state, only the calculated mixed singlet-triplet potential energy curve, belonging to the triplet family, is accessible in the experiment. For this relevant potential energy curve, the depth of the potential is already significantly decreased due to the applied magnetic field, which can explain the decrease of the observed density shift and the broadening of the spectral line.
The measurements presented in this thesis, and the simple theoretical model used to explain these measurements, clearly show the effect of the mixing of singlet and triplet scattering channels in Rb_2 Rydberg molecules. Another important aspect to note is that the shallow bound states in the mixed singlet-triplet potentials are strongly influenced by the p-wave shape resonance of ^{87}Rb. Furthermore, the presented high resolution spectra can in the future serve as a reference for the calculation of the electron-Rubidium scattering phase shifts. Experimental data was not available in this energy regime during the time these calculations [22, 23] were done. With the variety of experimental data as a reference, together with the improvement of the accuracy of the other input parameters, like the polarizibility of the 5S ground state of Rubidium, this could lead to a significant improvement in the calculation of the scattering phase shifts.

Outlook

There are many aspects of Rydberg physics that can be studied in the future using the experimental setup described in this thesis. However, in order to improve the stability of the electric field compensation and the temperature of the coils for the magnetic trap in the experiment, some changes have to be made to the experimental chamber. These changes were described in detail in chapter 3. During this thesis a lot of effort was put into the implementation of the new electric field control chamber and the improvement of the temperature stability of the coils for the QUIC-trap. Unfortunately, this implementation of the improved parts could not be finished during the thesis and is a project for the near future. With the improved experimental setup a lot of new aspects of Rydberg physics, like Rydberg states with an even higher principal quantum number, $n \gtrsim 200$, or circular Rydberg states, can be studied.
The main goal for the future is the in-situ imaging of the imprint of the scattering potential onto the density distribution of the BEC [45, 46], which should occur after some time, because the particles want to the minimize their energy and therefore 'flow' into the potential wells of the scattering potential caused by the Rydberg electron. This increase of particles at the positions of the potential wells of the scattering potential should be visible in the density distribution of the BEC, which can be directly imaged using phase contrast imaging. As the scattering potential is in first order directly proportional to the square of the absolute value of the electron wavefunction of the Rydberg state, this would be a direct observation of the electron orbital of the atomic state. For this 'wavefunction imaging', the setup of an in-situ phase contrast imaging system with a good spatial resolution is necessary. This was already built into the setup and is at the time of writing this thesis being optimized. In order to get the best possible pictures it is necessary to have the

wavefunction as big as the BEC and at the same time still have a deep enough scattering potential. For this a BEC with a smaller radial diameter would be preferable, but up to now the atom number is not stable enough to realize this. The experimental realization of the 'wavefunction imaging' would therefore also greatly profit from the improvements of the experimental chamber.
Another requirement of the imaging of the scattering potential is that the Rydberg atom stays in the target nS- or nD-state for a long enough time, in order for the imprint to become visible in the density distribution. This was also a main point of study during the time of this thesis, which led to the discovery that the Rydberg atom is subject to l-changing collisions on a time scale ranging from about 1 µs up to several tens of µs, depending on the principal quantum number of the Rydberg state and the density of the atomic cloud. The effect of these l-changing collisions can be seen by detecting the Rydberg atoms via state selective field ionization for different waiting times after the excitation. In these measurements it can be observed that the Rydberg state evolves from the original state with a known ionization voltage to a state, for which a higher voltage is necessary to ionize the Rydberg atom. The increase of the ionization voltage corresponds to Rydberg states with a higher angular momentum. It is interesting to note, that the time scale of the l-changing collisions shows some kind of threshold behaviour at around $n = 100$: the state change always happens on a time scale of about 1 µs for $n < 100$, while for principal quantum numbers with $n > 100$, the collision time increases up to several tens of µs. The experimental results of these l-changing collisions will be discussed in detail in future publications [7, 8]. Selected measurements are also shown in appendix A.4.

A. Anhang

A.1. Magnetic Field Dependency of the Mixed Singlet-Triplet Molecular Potentials

The interaction with the magnetic field included in the Hamiltonian as given by equation (4.39) on page 46 leads to further changes in the mixed potentials, as was already discussed in chapter 4.3. The dependency of the obtained potentials on the magnetic field is shown in figure A.1. There the potential strength, which is defined as the depth of the outermost well of the potentials, together with the Zeeman-shift of the asymptotic atomic energy levels is plotted against the amplitude of the magnetic field. Thereby the potentials are calculated by including the pure singlet and triplet potentials obtained from the full diagonalization method into the Hamiltonian and subsequent diagonalization of this Hamiltonian.

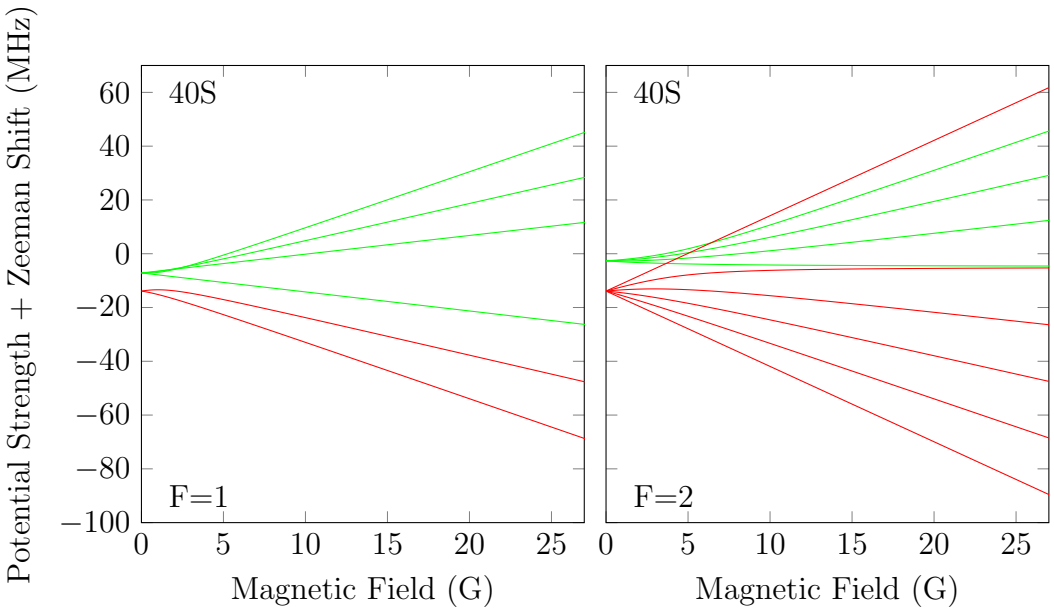

Figure A.1.: Dependence of the potential strength, which is defined as the depth of the outermost well of the potentials, together with the Zeeman-shift of each asymptotic atomic energy level on the amplitude of the external magnetic field. The potentials are grouped into a triplet (red) and a mixed (green) family, according to the situation in zero field. The zero of the vertical axis corresponds to the respective atomic hyperfine state ($F = 1,2$) in zero magnetic field.

For zero magnetic field there are two different values both for $F = 1$ and $F = 2$, corresponding to the triplet and mixed potentials shown in figure 4.7 on page 47. There are some potentials, e.g. the two outermost triplet potentials for $F = 2$, that only show a linear dependency on the magnetic field. As such the magnetic field only appears in the linear Zeeman-shift of the asymptotic atomic energy level and does not change the depth of the potential as it does for the other potentials. For large magnetic fields all the lines shown in figure A.1 show a linear dependency, meaning that there is a transition to a regime where the magnetic field does not influence the depth of the potentials anymore.
Calculating the binding energies of the molecules from the potentials, it is also possible to see this dependency on the magnetic field. This is done in figure A.2 for the binding energies of the triplet and mixed potentials that are accessible in the experiment. These binding energies are calculated from the potentials using the effective s-wave scattering lengths $a_S = -0.2\,a_0$ and $a_T = -15.7\,a_0$ for the principal quantum numbers that were observed in the experiment. In order to compare the different quantum numbers the binding energies of the bound states were normalized to the binding energies of the pure triplet dimer molecules.

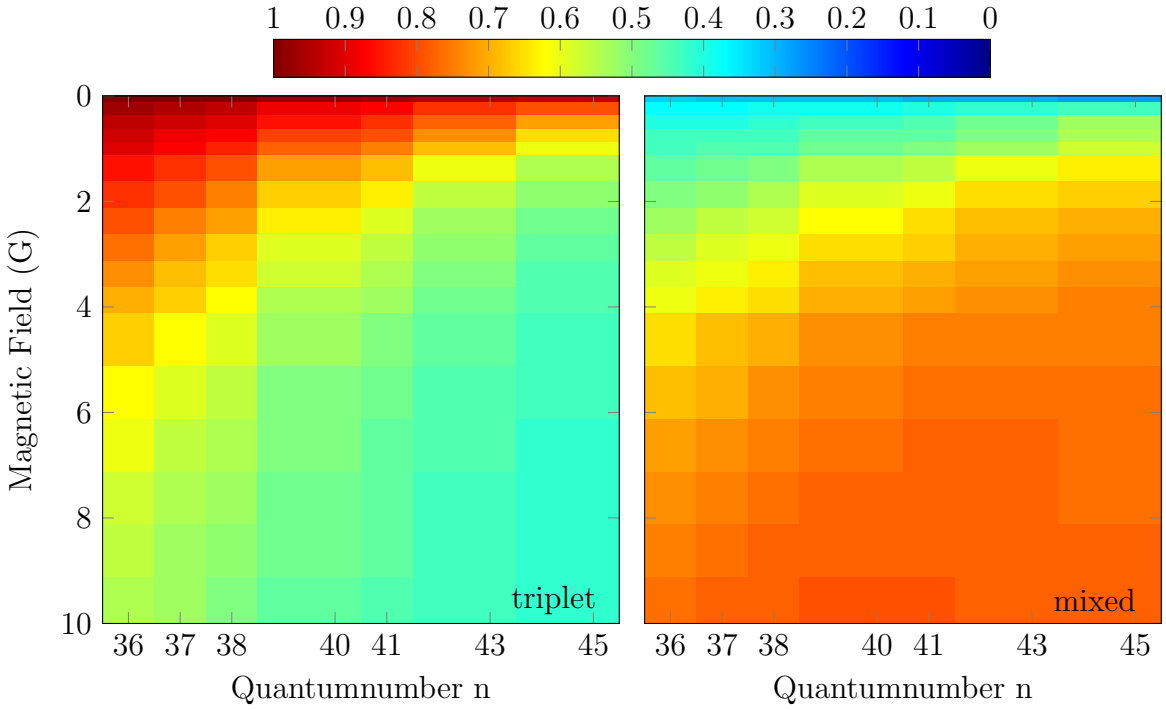

Figure A.2.: Calculated binding energies from the effective s-wave scattering potentials, normalized to the binding energy of the pure triplet dimer molecule, plotted against the prinicipal quantum number n and the amplitude of the magnetic field. The obtained binding energies for the triplet potential are shown on the left side and the binding energies for the mixed molecules on the right.

It can be seen that for zero magnetic field the binding energies of the triplet molecules (left side of figure A.2) match the pure triplet binding energy, while the binding energy for the mixed molecules (left side of figure A.2) is smaller. For higher magnetic fields the binding energy of the triplet molecule decreases, which can be explained by the decrease of the potential depth (compare with figure A.1). At the same time the mixed potential becomes deeper and as such the binding energy increases. This effect saturates after a certain magnetic field, which agrees with what can be observed from figure A.1. There is also a dependency with respect to the principal quantum number visible in the binding energies shown in figure A.2.
Another important quantity that depends on the magnetic field is the overlap of the calculated eigenstates with the atomic state that is excited in the experiment. This dependency is shown in figure A.3 for the range of principal quantum numbers that were studied in the experiment. The shown number for the overlap is the overlap in the middle of the outermost well of the potential (compare with figure 4.10 on page 50).

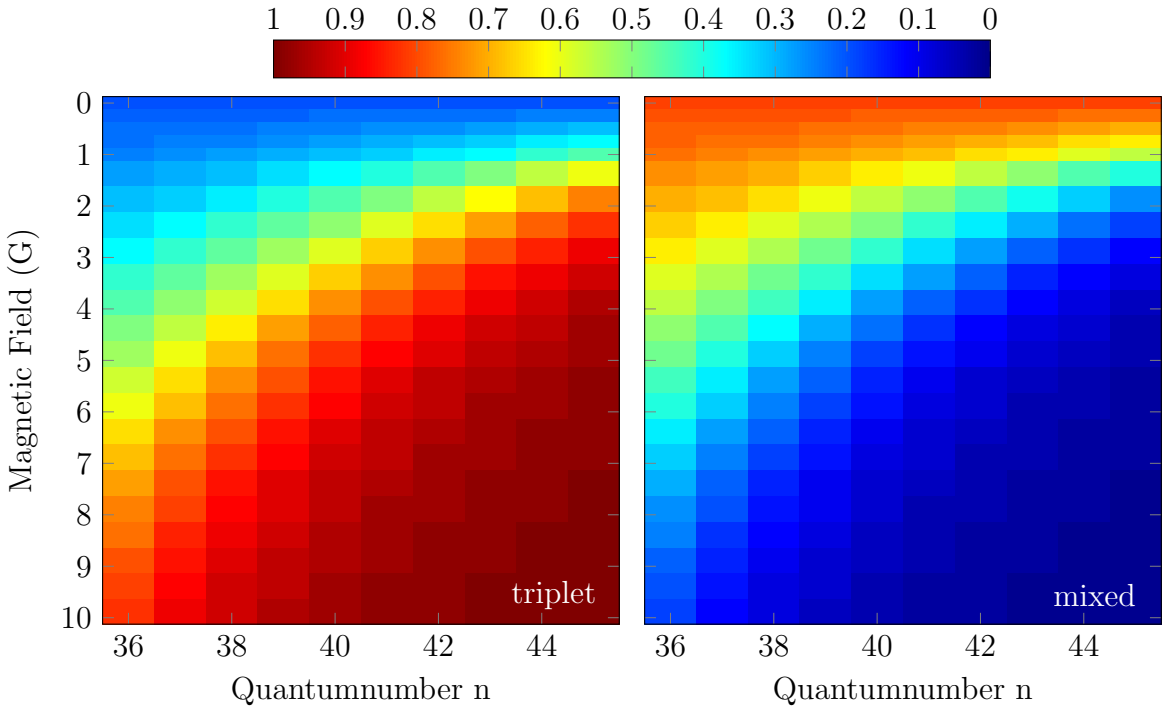

Figure A.3.: Calculated overlap $|\langle\psi_{\text{ex}}|\ \psi_{\text{eig}}\rangle|^2$ of the eigenstates of the Hamiltonian with the experimentally accessible atomic state as a function of the principal quantum number n and the amplitude of the magnetic field. The overlap is thereby obtained as the value in the middle of the outermost well of the molecular potentials.

The overlap to the triplet potential (left side of figure A.3) is relative small for small magnetic fields and then increases until it reaches the maximum value of 1 for high magnetic fields. The overlap for the mixed potential however is strong for small fields and then decreases. This means that for strong magnetic fields only the triplet potential is accessible in the experiment, for which the potential depth at that point is already relative small (compare to figure A.2). Also for the calculated overlap there is a similar dependency on the principal quantum number as was already seen in figure A.2.

A.2. Inverted Excitation Scheme

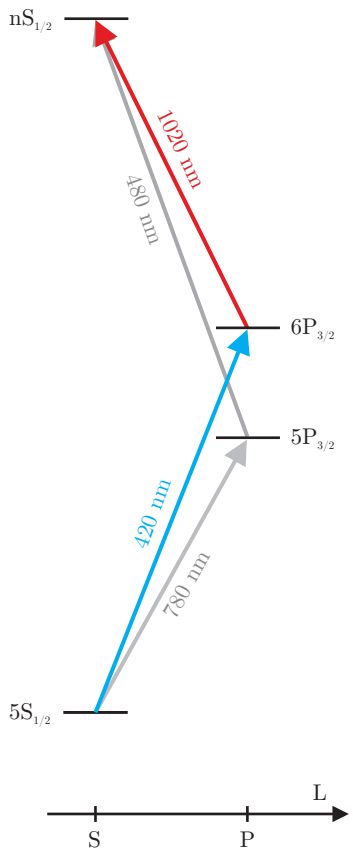

Figure A.4.: Simplified level scheme to the illustrate the two-photon Rydberg excitation for ^{87}Rb. The blue and red arrows indicate the 'inverted scheme' used in the experiment, which uses a 420 nm for the lower transition to the $6P_{3/2}$ state and a 1020 nm laser to the subsequent excitation to the nS Rydberg state. In grey the 'normal excitation scheme' is shown, which uses the $5P_{3/2}$ state as the intermediate state. The wavelengths for the necessary laser are then 780 nm and 480 nm.

A.3. Molecular Potential Energy Curves for the 53S Rydberg State

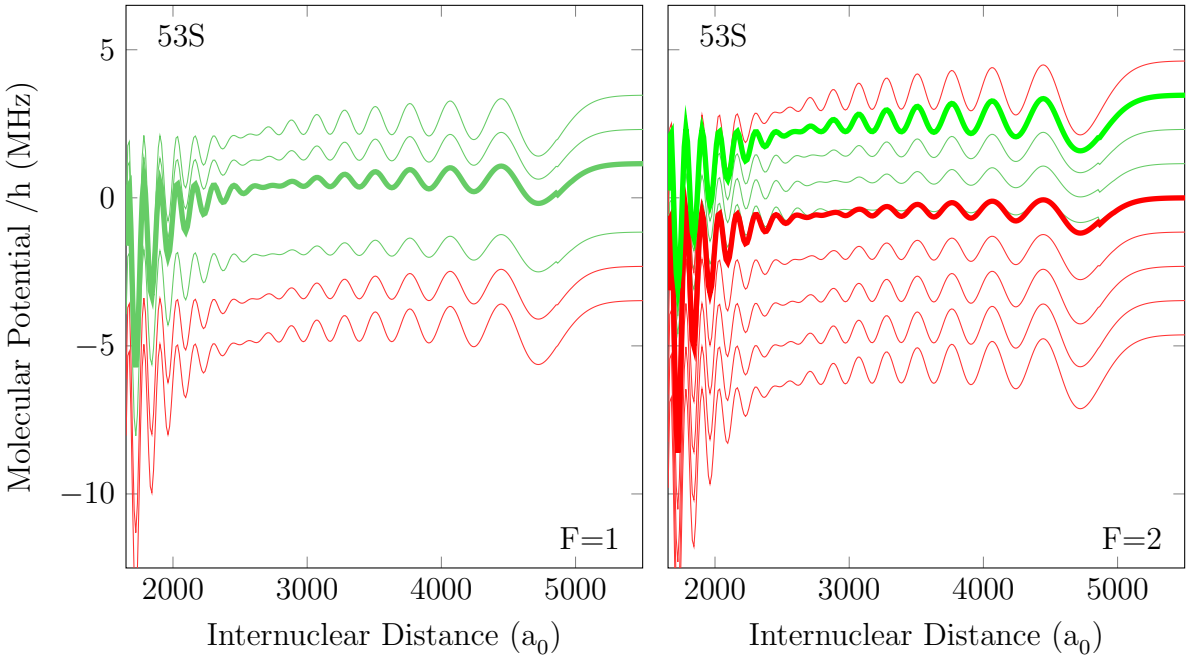

Figure A.5.: Molecular potential energy curves for the interaction of a 5S ground state atom with an atom in the 53S Rydberg state as a function of the internuclear distance R. For the calculation the pure singlet and triplet potentials obtained with the full diagonalization method were used. The inclusion of the hyperfine interaction of the 5S ground state atom and the external magnetic field of B=1.65 G leads to the mixing of singlet and triplet scattering channels. The potentials are grouped into two families, corresponding to the case of zero magnetic field: triplet (red) and mixed (green) potential energy curves. In the experiment only the triplet and mixed molecular potentials of F=2, which are indicated with thick red and green lines, respectively, can be excited. Zero on the vertical axis corresponds to the asymptotes of the respective degenerate hyperfine state (F = 1,2) in zero magnetic field.

A.4. L-Changing Collisions

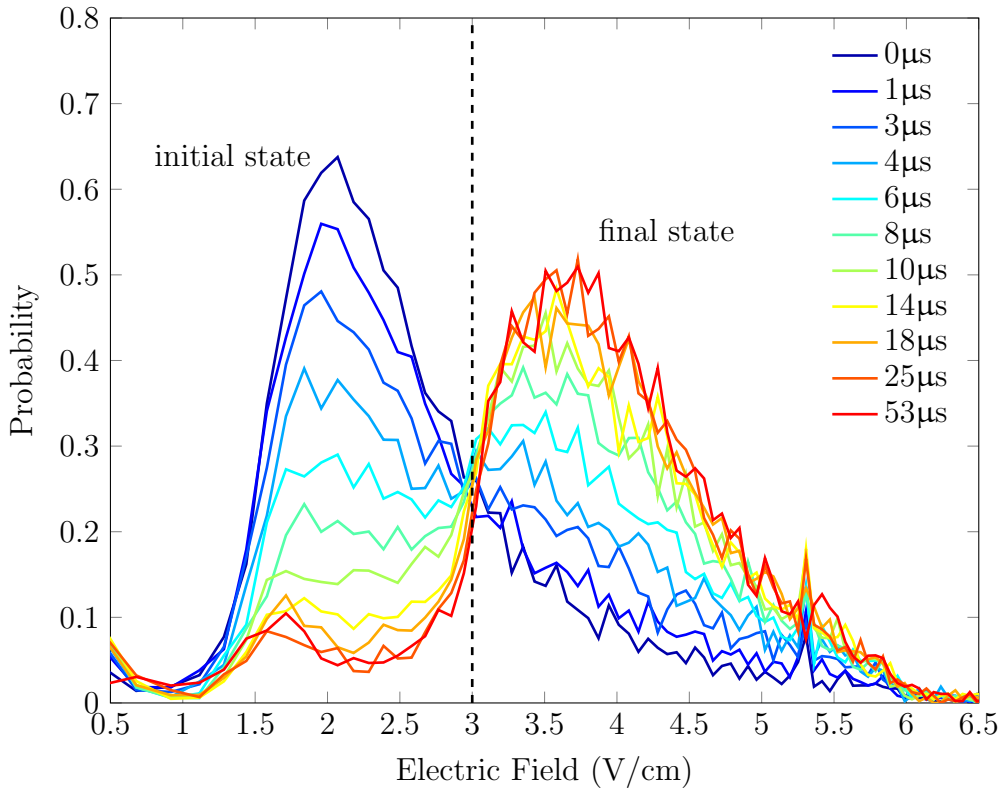

Figure A.6.: State selective field ionization analysis of the detected ions for the 121S state. Thereby the electric field is linearly ramped up within 3 µs after a 500 ns excitation pulse. From the measured arrival time on the ion detector, the necessary electric field for the field ionization can be extracted out of an ion trajectory simulation. The delay time between the excitation and ionization ramp is changed in between 0 µs and 53 µs. For the immediate ionization most of the ions are ionized at around 2 V/cm, corresponding to the initial 121S state. With a delay time between excitation and ionization, it is possible that the Rydberg atom collides with a neighbouring ground state atom. This collision can lead to a change of the angular momentum l and therefore the required ionization field can increase by a factor of $2-4$, corresponding to a high l-state [65]. The dashed black line indicates an ionization field, that can be used in a two-step ionization process to separate the initial and the final state.

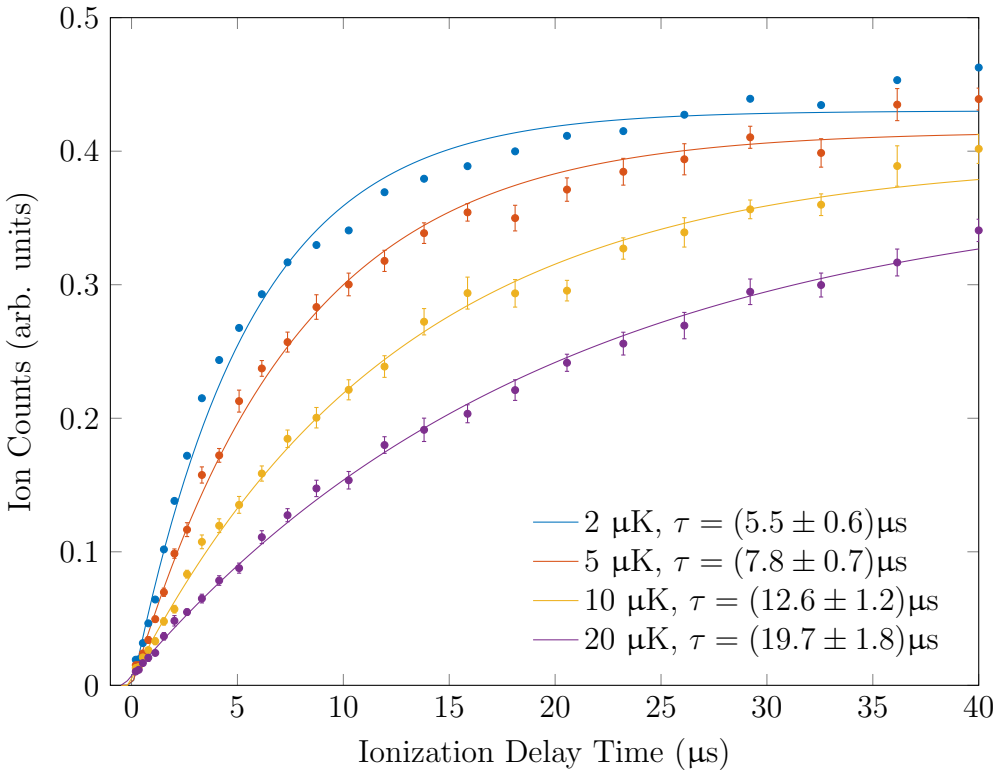

Figure A.7.: Measurement of the l-changing collision time of the 53S state in thermal clouds with a different temperature and atom number. For this measurement a two-step ionization is used, as it is indicated schematically by the dashed black line in figure A.6. The average density in the excitation volume (overlap of the two excitation beams with the atomic cloud) is $2.5 \cdot 10^{13}\,\mathrm{cm}^{-3}$, $9.6 \cdot 10^{12}\,\mathrm{cm}^{-3}$, $4.8 \cdot 10^{12}\,\mathrm{cm}^{-3}$ and $2.4 \cdot 10^{12}\,\mathrm{cm}^{-3}$, respectively for the 2 µK, 5 µK, 10 µK and the 20 µK thermal cloud. The shown ion counts are the detected ions on the MCP for the second ionization step, meaning only Rydberg atoms that underwent a state change. The data points are averaged over 500 excitation pulses in one atomic cloud and over 14 different clouds, with the error bars indicating the deviation from the mean value. The overall ion counts, meaning the sum of both ionization steps, is constant in the range of the errorbars for all ionization delay times. To the data an exponential function of the form $P(t) = 1 - \exp(-t/\tau)$ is fitted in order to extract the collision time τ. The extracted collision times and their respective confidential bound of the fit are given in the legend.

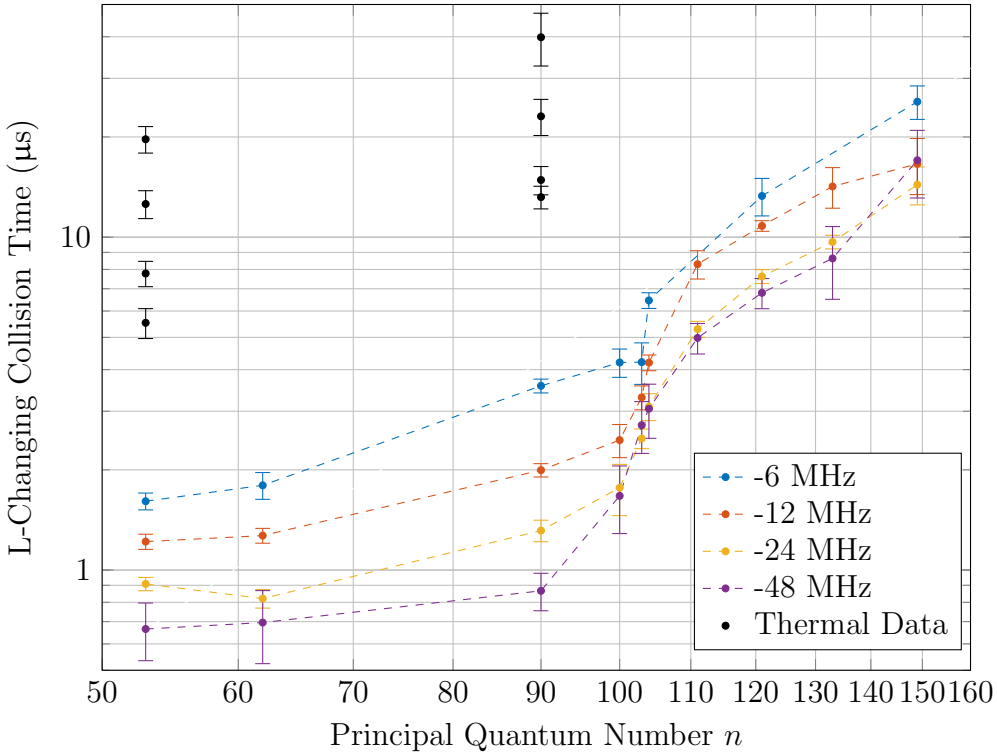

Figure A.8.: Experimentally observed l-changing collision times for different principal quantum numbers n. The different colors correspond to measurements done at a different detuning from the atomic resonance in a BEC, while the black points correspond to measurements done in a thermal cloud with a varying temperature and atom number. The shown collision times were extracted from measurements as exemplary shown in figure A.7, which corresponds to the thermal data points for the 53S state. The thermal data for the 90S state was measured in thermal clouds with similar experimental parameters. The error bars indicate the confidential interval of the fit used to obtain the collision times and also take into account several measurements for each data point. The different detunings in the BEC correspond to different configuration for the distribution of the atoms in the cloud, which corresponds to different density distributions. For the data measured in the thermal cloud the same parameters were used for 53S and 90S as shown in figure A.7, with the densities significantly lower than in the BEC. As expected the collision takes more time for a lower density, which corresponds to a larger internuclear separation. At around $n \approx 100$ a threshold is reached, that leads to significantly longer collision times, independent from the excited density range of the BEC.

Bibliography

[1] F. Böttcher, A. Gaj, K. M. Westphal, M. Schlagmüller, K. S. Kleinbach, R. Löw, T. C. Liebisch, T. Pfau and S. Hofferberth, *Observation of mixing between singlet and triplet scattering channels in Rb_2 Rydberg molecules*, `http://arxiv.org/abs/1510.01097` (2015)

[2] D. A. Anderson, S. A. Miller and G. Raithel, *Angular-momentum couplings in long-range Rb_2 Rydberg molecules*, Physical Review A, Volume 90, Issue 6 (2014)

[3] H. Saßmannshausen, F. Merkt and J. Deiglmayr, *Experimental characterization of singlet scattering channels in long-range Rydberg molecules*, `http://arxiv.org/abs/1412.0846` (2014)

[4] M. Schlagmüller, T. C. Liebisch, H. Nguyen, G. Lochead, F. Engel, F. Böttcher, K. M. Westphal, K. S. Kleinbach, R. Löw, S. Hofferberth, T. Pfau, J. Pérez-Ríos and C. H. Greene, *Probing a scattering resonance in Rydberg molecules with a Bose-Einstein condensate*, `http://arxiv.org/abs/1510.07003` (2015)

[5] H. Nguyen, T. C. Liebisch, M. Schlagmüller, G. Lochead, K. M. Westphal, R. Löw, S. Hofferberth and T. Pfau, *Probing a quantum gas with single Rydberg atoms*, `http://arxiv.org/abs/1506.05302` (2015)

[6] T. C. Liebisch et al. (future work)

[7] M. Schlagmüller et al. (future work)

[8] Michael Schlagmüller, *Static and dynamic interactions of a single Rydberg impurity in Bose-Einstein condensate*, Dissertation, 5. Physikalisches Institut, Universität Stuttgart (future work)

[9] Huan Nguyen, Dissertation, 5. Physikalisches Institut, Universität Stuttgart (future work)

[10] Udo Hermann, *Analysing and improving high resolution Rydberg field ionization statistics*, Masterarbeit, 5. Physikalisches Institut, Universität Stuttgart (2014)

[11] Christoph Tresp, *A Setup for Highly Precise Excitation and Detection of Rydberg Atoms*, Masterarbeit, 5. Physikalisches Institut, Universität Stuttgart (2012)

[12] Thomas Schmid, *High precision excitation, manipulation and detection of Rydberg atoms*, Masterarbeit, 5. Physikalisches Institut, Universität Stuttgart (2014)

[13] Stephan Jennewein, *Building an Apparatus for Cold Rubidium Rydberg Atoms*, Diplomarbeit, 5. Physikalisches Institut, Universität Stuttgart (2012)

[14] Vera Bendkowsky, *Ultralong-range Rydberg molecules: Investigation of a novel binding*, Dissertation, 5. Physikalisches Institut, Universität Stuttgart (2010)

[15] P. G. Burke, *R-Matrix Theory of Atomic Collisions*, Springer Series on Atomic, Optical and Plasma Physics 61 (2011)

[16] T. F. O'Malley, L. Spruch and L. Rosenberg, *Modification of Effective-Range Theory in the Presence of a Long-Range* (r^{-4}) *Potential*, J. Math. Phys. 2, 491 (1961)

[17] E. Amaldi and E. Segrè, *Effect of pressure on high terms of alkaline spectra*, Nature 133, 141 (1934)

[18] E. Fermi, *Sopra lo spostamento per pressione delle righe elevate delle serie spettrali*, Nuovo Cimento 11, 157 (1934)

[19] A. Omont, *On the Theory of Collisions of Atoms in Rydberg States with Neutral Particles*, Le Journal de Physique, 38 (11), pp.1343-1359 (1977)

[20] J. W. S. Rayleigh, *The Theory of Sound*, 1st edn. (Macmillan and Co., London, 1877)

[21] H. Faxén and J. Holtsmark, *Beitrag zur Theorie des Durchganges langsamer Elektronen durch Gase*, Zeits. f. Phys. 45, 307 (1927)

[22] I. I. Fabrikant, *Interaction of Rydberg atoms and thermal electrons with K, Rb and Cs atoms*, J. Phys. B: At. Mol. Phys. 19, 1527 - 1540 (1986)

[23] C. Bahrim, U. Thumm and I. I. Fabrikant, ${}^3S^e$ *and* ${}^1S^e$ *scattering lengths for* e^- *+ Rb, Cs and Fr collisions*, J. Phys. B: At. Mol. Phys. 34, L195 - L201 (2001)

[24] E. Feenberg, *The Scattering of Slow Electrons by Neutral Atoms*, Phys. Rev. 40, 40 (1932)

[25] J. M. Blatt and J. D. Jackson, *On the Interpretation of Neutron-Proton Scattering Data by the Schwinger Variational Method*, Phys. Rev. 76, 18 (1949)

[26] H. A. Bethe, *Theory of the Effective Range in Nuclear Scattering*, Phys. Rev. 76, 38 (1949)

[27] O. Hinckelmann and L. Spruch, *Low-Energy Scattering by Long-Range Potentials*, Phys. Rev. A, Vol.3 No. 2, 642 (1971)

[28] C. H. Greene, A. S. Dickinson and H. R. Sadeghpour, *Creation of Polar and Nonpolar Ultra-Long-Range Rydberg Molecules*, Physical Review Letters Volume 85, Number 12 (2000)

[29] V. Bendkowsky, B. Butscher, J. Nipper, J. P. Shaffer, R. Löw and T. Pfau, *Observation of ultralong-range Rydberg molecules*,Nature 458, 0028 (2009)

[30] V. Bendkowsky, B. Butscher, J. Nipper, J. B. Balewski, J. P. Shaffer, R. Löw, T. Pfau, W. Li, J. Stanojevic, T. Pohl and J. M. Rost, *Rydberg Trimers and Excited Dimers Bound by Internal Quantum Reflection*, Phys. Rev. Lett. 105, 163201 (2010)

[31] B. Butscher, J. Nipper, J. B. Balewski, L. Kukota, V. Bendkowsky, R. Löw and T. Pfau, *Atom-molecule coherence for ultralong range Rydberg dimers*, Nature Physics 6, 970–974 (2010)

[32] B. Butscher, V. Bendkowsky, J. Nipper, J. B. Balewski, L. Kukota, R. Löw, T. Pfau, W. Li, T. Pohl and J. M. Rost, *Lifetimes of ultralong-range Rydberg molecules in vibrational ground and excited states*, J. Phys. B: At. Mol. Opt. Phys. 44, 184004 (2011)

[33] W. Li, T. Pohl, J. M. Rost, Seth T. Rittenhouse, H. R. Saeghpour, J. Nipper, B. Butscher, J. B. Balewski, V. Bendkowsky, R. Löw and T. Pfau, *A Homonuclear Molecule with a Permanent Electric Dipole Moment*, Science 334, 1110 (2011)

[34] A. T. Krupp, A. Gaj, J. B. Balewski, P. Ilzhöfer, S. Hofferberth, R. Löw, T. Pfau, M. Kurz, and P. Schmelcher, *Alignment of D-state Rydberg molecules*, Phys. Rev. Lett. 112, 143008 (2014)

[35] A. Gaj, A. T. Krupp, J. B. Balewski, R. Löw, S. Hofferberth and T. Pfau, *From molecular spectra to a density shift in dense Rydberg gases*, Nature Comm. 5, 4546 (2014)

[36] A. Gaj, A. T. Krupp, P. Ilzhöfer, R. Löw, S. Hofferberth and T. Pfau, *Hybridization of Rydberg electron orbitals by molecule formation*, Phys. Rev. Lett. 115, 023001 (2015)

[37] D. Booth, S. T. Rittenhouse, J. Yang, H. R. Sadeghpour and J. P. Shaffer, *Production of trilobite Rydberg molecule dimers with kilo-Debye permanent electric dipole moments*, Science 348, 99 (2015)

[38] J. Tallant, S. T. Rittenhouse, D. Booth, H. R. Sadeghpour and J. P. Shaffer, *Observation of blueshifted ultralong-range Cs_2 Rydberg molecules*, Phys. Rev. Lett. 109, 173202 (2012)

[39] D. A. Anderson, S. A. Miller, and G. Raithel, *Photoassociation of Long-Range nD Rydberg Molecules*, Phys. Rev. Lett. 112, 163201 (2014)

[40] M. A. Bellos, R. Carollo, J. Banerjee, E. E. Eyler, P. L. Gould, and W. C. Stwalley, *Excitation of weakly bound molecules to trilobitelike Rydberg states*, Phys. Rev. Lett. 111, 053001 (2013)

[41] B. DeSalvo, J. Aman, F. Dunning, T. Killian, H. Sadeghpour, S. Yoshida and J. Burgdörfer, *Ultralong-Range Rydberg Molecules in a Divalent-Atomic System*, `http://arxiv.org/abs/1503.07929` (2015).

[42] C. Fey, M. Kurz, P. Schmelcher, S. T. Rittenhouse and H. R. Sadeghpour, *A comparative analysis of binding in ultralong-range Rydberg molecules*, New J. Phys. 17, 055010 (2015)

[43] T. Manthey, T. Niederprüm, O. Thomas and H. Ott, *Dynamically Probing Ultracold Lattice Gases via Rydberg Molecules*, `http://arxiv.org/abs/1506.05955` (2015)

[44] J. B. Balewski, A. T. Krupp, A. Gaj, D. Peter, H. P. Büchler, R. Löw, S. Hofferberth and T. Pfau, *Coupling a single electron to a Bose-Einstein condensate*, Nature 502, 664-667 (2013)

[45] T. Karpiuk, M. Brewczyk, K. Rzazewski, A. Gaj, J. B. Balewski, A. T. Krupp, M. Schlagmüller, R. Löw, S. Hofferberth and T. Pfau, *Imaging single Rydberg electrons in a Bose-Einstein condensate*, New J. Phys. 17, 053046 (2015)

[46] J. Wang, M. Gacesa and R. Côté, *Rydberg Electrons in a Bose-Einstein Condensate*, Phys. Rev. Lett. 114, 243003 (2015)

[47] Daniel A. Steck, *Rubidium 87 D Line Data*, Version 2.1.4, `http://steck.us/alkalidata`

[48] T. F. Gallagher, *Rydberg Atoms*, p.353, Cambridge University Press (2005)

[49] M. Mack, F. Karlewski, H. Hattermann, S. Höckh, F. Jessen, D. Cano and J. Fortágh, *Measurement of absolute transition frequencies of ^{87}Rb to nS and nD Rydberg states by means of electromagnetically induced transparency*, Physical Review A 83, 052515 (2011)

[50] T. Esslinger, I. Bloch and T. W. Hänsch, *Bose-Einstein condensation in a quadrupole-Ioffe-configuration trap*, Phys. Rev. A 58, R2664(R) (1998)

[51] H. J. Metcalf and P. van der Straten, *Laser Cooling and Trapping*, Springer (1999)

[52] M. R. Andrews, M. O. Mewes, N. J. van Druten, D. S. Durfee, D.M. Kurn and W. Ketterle, *Direct, Nondestructive Observation of a Bose Condensate*, Science Vol.273 No. 5271 pp. 84-87 (1996)

[53] H. Haken and H. C. Wolf, *Molekülphysik und Quantenchemie*, Kapitel 9: Rotationsspektren, p. 159-177, Springer Verlag, 5. Auflage (2006)

[54] P. A. M. Dirac, *The Principles of Quantum Mechanics*, 3rd edition,Clarendon Press, Oxford (1947)

[55] W. Pauli, *Zur Quantenmechanik des magnetischen Elektrons*, Zeitschrift für Physik. 43, 1927, p. 601-623.

[56] W. Nolting, *Grundkurs Theoretische Physik 5/2 Quantenmechanik – Methoden und Anwendungen*, Springer, 6. Auflage (2006)

[57] C. Ramsauer, *Über den Wirkungsquerschnitt der Gasmoleküle gegenüber langsamen Elektronen*, Annalen der Physik 369, 513 (1921)

[58] W. Demtröder, *Laserspektroskopie: Grundlagen und Techniken*, Springer Verlag, 5. Auflage (2007)

[59] J. L. M. Quiroz González and D. Thompsonb, *Getting started with Numerov's method*, Computers in Ohysics, Vol. 11, No. 5 (1997)

[60] J. M. Blatt, *Practical Points Concerning the Solution of the Schrödinger Equation*, Journal of Computational Physics 1, 382-396 (1967)

[61] E. Rutherford, *The Scattering of α and β Particles by Matter and the Structure of the Atom*, Philosophical Magazine, Series 6, Vol. 21, p. 669-688 (1911)

[62] F. Hund, *Deutung der Molekelspektren, I und II*, Zeitschrift für Physik. 40, 742-764 (1927) und 42, 93-120 (1927)

[63] E. Urban, T. A. Johnson, T. Henage, L. Isenhower, D. D. Yavuz, T. G. Walker and M. Saffman, *Observation of Rydberg blockade between two atoms*, Nature Physics 5, 110 - 114 (2009)

[64] F. Carmago, J. D. Whalen, R.Ding, H. R. Sadeghpour, S. Yoshida, J. Burgdörfer, F. B. Dunning and T. C. Killian, *Lifetimes of ultra-long-range strontium Rydberg molecules*, `http://arxiv.org/abs/1511.06793` (2015)

[65] T. F. Gallagher, *Rydberg Atoms*, pp. 83-87, Cambridge University Press (2005)

[66] J. L. Wiza, *Microchannel Plate Detectors*, Nuclear Instruments and Methods, Vol. 162, 1979, pp. 587-601 (1979)

[67] D. C. Anacker and J. L. Erskine, *Analysis of microchannel plate response in relation to pulsed laser time-of-flight photoemission spectroscopy*, Review of Scientific Instruments Vol. 62 No. 5 (1991)

[68] A. Tauschinsky, R. Newell, H. B. van Linden van den Heuvell and R. J. C. Spreeuw, *Measurement of ^{87}Rb Rydberg-state hyperfine splitting in a room-temperature vapor cell*, Phys. Rev. A 87, 042522 (2013)

[69] W. Li, I. Mourachko, M. W. Noel and T. F. Gallagher, *Millimeter-wave spectroscopy of cold Rb Rydberg atoms in a magneto-optical trap: Quantum defects of the ns, np, and nd series*, Phys. Rev. A 67, 052502 (2003)

Danksagung

An dieser Stelle möchte ich einigen Leuten danken, die zum Gelingen dieser Arbeit beigetragen haben. Dies sind im Besonderen:

- **Prof. Dr. Tilman Pfau**, der mir die Möglichkeit gegeben hat meine Bachelor- und Masterarbeit am Institut zu schreiben.
- **Prof. Dr. Peter Michler** in seiner Funktion als Mitberichter dieser Arbeit.
- **Tara Cubel Liebisch**, **Michael Schlagmüller**, **Karl Magnus Westphal**, **Kathrin Kleinbach** und **Felix Engel** für die tolle Atmosphäre bei der Arbeit am Experiment und für die ganzen Sachen die ich während des Jahres von Ihnen lernen konnte.
- **Sebastian Hofferberth** und **Anita Gaj** für die vielen Diskussionen und die ganze Arbeit die zum Verständnis der gemessenen Molekülspektren führte.
- **Udo Hermann** und **Christoph Tresp** die im Rahmen ihrer Masterarbeiten die neue bzw. die aktuelle Version der Experimentbox entworfen haben.
- **Huan Nguyen**, **Thomas Schmid**, **Graham Lochead** und **Stephan Jennewein** die alle ebenfalls ihren Teil beim Aufbau des Experiments beigetragen haben.
- Allen Mitarbeitern vom 5. Physikalischen Institut für die tolle Atmosphäre am Institut.